



universität
wien

MASTERARBEIT / MASTER'S THESIS

Titel der Masterarbeit / Title of the Master's Thesis

„Enabling Technology for High-Frequency Quantum Magnonics“

verfasst von / submitted by

David Schmoll BSc

angestrebter akademischer Grad / in partial fulfilment of the requirements for the degree of

Master of Science (MSc)

Wien, 2022 / Vienna, 2022

Studienkennzahl lt. Studienblatt /
degree programme code as it appears on
the student record sheet:

UA 066 876

Studienrichtung lt. Studienblatt /
degree programme as it appears on
the student record sheet:

Masterstudium Physik

Betreut von / Supervisor:

Univ.-Prof. Dr. habil. Andrii Chumak

Mitbetreut von / Co-Supervisor:

Dr. Sebastian Knauer

Abstract

Spin waves, with their corresponding quasi-particles magnons and the underlying fundamental physics, possess promising technological potential for the transmission, storage and processing of information [1]. Comprehensive technological advancements in the access to millikelvin temperatures, combined with high-frequency microwave technology, allow first steps towards the investigation of individual magnons in the field of quantum magnonics, and enable a path towards their implementation in hybrid quantum systems [2]. Such ultra-low temperatures are required to eliminate thermally excited magnons [3]. Thus, the scientific objective of this thesis was to develop and characterise a measurement platform for the investigation of propagating spin waves with microwave technology at millikelvin temperatures. First, a state-of-the-art Bluefors LD250 cryogen-free dilution refrigerator system, combined with a superconducting vector magnet and a 40 GHz-rated VNA measurement system, was installed and characterised. Further, a multilayer high-frequency PCB was designed with the software package Altium Designer as the connecting interface between the measurement setup and the investigated samples. The high-frequency transmission lines of the PCB were computationally analysed and optimised with the software package COMSOL Multiphysics, allowing microwave propagation up to 40 GHz. After design and analysis, the high-frequency PCB was manufactured and tested. To prove the capabilities of the PCB within the cryogenic setup, propagating spin waves were excited and detected with surface-bonded gold wires in a $5.65\ \mu\text{m}$ thick yttrium iron garnet (YIG) strip on gadolinium gallium garnet (GGG). The functionality of the high-frequency PCB will allow future YIG samples, with e-beam or focused ion beam patterned antenna structures (see [4]), to be directly bonded to the PCB and therefore efficiently feed and detect microwave signals. Finally, YIG samples, grown on GGG, were used to perform propagating spin-wave spectroscopy at millikelvin temperatures, via the excitation and detection of magnetostatic surface spin waves (MSSWs). The cryogenic results are compared to room temperature measurements. These studies represent the first recorded propagating spin waves within the realised dilution refrigerator system. The combination of the built dilution refrigerator, including the superconducting vector magnet together with the calibrated VNA measurement system, and the capabilities of the novel high-frequency PCB, creates a future measurement platform for experiments in the field of quantum magnonics and hybrid opto-magnonic quantum systems.

Kurzfassung

Spinwellen, mit ihren zugehörigen Quasi-Teilchen Magnonen, sowie ihrer zugrunde liegenden fundamentalen Physik, zeigen vielversprechendes Potential zur Informationsübertragung, -speicherung und -verarbeitung [1]. Die fortschreitende technologische Entwicklung im Zugang zum millikelvin Temperaturbereich, verbunden mit Hochfrequenz-Mikrowellentechnologie, erlauben erste Schritte zur Erforschung einzelner Magnonen im Feld der Quanten-Magnonik und deren Implementierung in hybriden Quantensystemen [2]. Solch ultra-tiefe Temperaturen sind entscheidend, um thermisch angeregte Magnonen zu eliminieren [3]. Das Ziel dieser Arbeit ist es, eine Plattform zur Messung von propagierenden Spinwellen bei millikelvin Temperaturen umzusetzen und zu charakterisieren. Zuerst wurde ein "Bluefors LD250 Cryogen-Free Dilution Refrigerator"-System, kombiniert mit einem supraleitendem Vektormagneten und einem bis zu 40 GHz-klassifiziertem VNA-Messsystem, im Labor installiert und charakterisiert. Weiters wurde ein Multilag-Hochfrequenz-PCB, als Nahtstelle zwischen dem Messsystem und der zu untersuchenden Probe, mit dem Softwarepaket "Altium Designer" entworfen. Die Hochfrequenz-Signalleitungen des PCBs wurden mit dem Softwarepaket "COMSOL Multiphysics" computergestützt analysiert und optimiert, um eine Signalübertragung bis zu einer Frequenz von 40 GHz zu ermöglichen. Nach Entwurf und Analyse wurde das Hochfrequenz-PCB industriell gefertigt und im Labor experimentell getestet. Um die Funktionalität des PCBs im kryogenen Messsystem zu prüfen, wurden propagierende Spinwellen mit Hilfe eines Golddrahts in einer $5.65\ \mu\text{m}$ dicken "Yttrium-Eisen-Granat"-Probe angeregt und detektiert. Der Entwurf des Hochfrequenz-PCBs erlaubt zukünftigen YIG-Proben, mit lithographierten Antennenstrukturen (z.B. [4]), direkt zur Probe verbunden zu werden und dadurch effizient Spinwellen anzuregen und zu detektieren. "Yttrium-Eisen-Granat" (YIG) auf einem "Gadolinium-Gallium-Granat"-Substrat (GGG) wurde als Probe zur Untersuchung von propagierenden Spinwellen bei kryogenen Temperaturen verwendet. Dazu werden die Resultate propagierender Spinwellen Spektroskopie, anhand von magnetostatischen Oberflächenwellen diskutiert. Die Ergebnisse der kryogenen Messungen wurden dabei mit bei Raumtemperatur aufgenommenen Daten verglichen. Die durchgeführten Experimente stellen die ersten gemessenen Spinwellen im realisierten kryogenen Setup dar. Die Kombination des "Dilution Refrigerators", einem supraleitenden Vektormagneten und einem kalibrierten VNA Messsystem, zusammen mit den technischen Möglichkeiten des neuen Hochfrequenz-PCBs, formt eine Messplattform für zukünftige Experimente im Feld der Quantenmagnonik und hybrider Quantensysteme.

Contents

Abstract	3
Kurzfassung	6
1. Introduction	11
1.1. Motivation	11
1.2. Introduction to Magnetism	11
1.3. Spin Waves	13
1.4. Quantum Magnonics	16
2. Experimental and Computational Methods	19
2.1. Concept of a Dilution Refrigerator System	19
2.1.1. Introduction to Cryogenics	19
2.1.2. Dilution Refrigerators	20
2.1.3. BF-LD250 Cryogen-Free Dilution Refrigerator System	23
2.2. Concepts of Radio Frequency Technology	28
2.2.1. Radiowaves	28
2.2.2. Transmission Lines and Scattering Parameters	29
2.2.3. High-Frequency PCB	30
2.3. Finite Element Frequency-Domain Simulation	33
3. Experimental Realisation and Characterisation of a Dilution Refrigerator System	35
3.1. Realisation of the Dilution Refrigerator Measurement Setup	35
3.2. Calibration of the Dilution Refrigerator System	37
3.2.1. Cool Down Curve	37
3.2.2. Heat Load Test	38
3.2.3. Reference Measurement of Cable Transmission	40
3.2.4. Cooling Behaviour of the Vector Magnet	42
4. Analysis of a High-Frequency PCB for Quantum Magnonics	45
4.1. Computational Analysis of High-Frequency Transmission Lines	45
4.2. Proof of Concept of the High-Frequency PCB at Millikelvin Temperatures	48
4.3. Prospects of the High-Frequency PCB	49
5. Propagating Spin-Wave Spectroscopy at Millikelvin Temperatures	55
6. Conclusions and Outlook	67
Bibliography	71
A. Appendix	75

List of Tables	83
List of Figures	85

List of Abbreviations

YIG	Yttrium Iron Garnet
GGG	Gadolinium Gallium Garnet
MSSW	Magnetostatic Surface Spin Wave
BVMSW	Backward Volume Magnetostatic Spin Wave
FVMSW	Forward Volume Magnetostatic Spin Wave
PSWS	Propagating Spin-Wave Spectroscopy
FMR	Ferromagnetic Resonance
VNA	Vector Network Analyser
PCB	Printed Circuit Board
RF	Radio Frequency
SNR	Signal to Noise Ratio
GCPW	Grounded Coplanar Waveguide
DR	Dilution Refrigerator
PTC	Pulse Tube Cooler
DU	Dilution Unit
GHS	Gas Handling System
MXC	Mixing Chamber
GGHS	Gas Gap Heat Switch
PCS	Persistent Current Switch

1. Introduction

1.1. Motivation

Felix Bloch theoretically predicted a collective propagating spin precession in the form of waves in magnetic materials at the beginning of the 20th century [5]. These eigenexcitations of the electron spins in magnetically ordered systems can be observed in ferro-, ferri- and antiferromagnets and are referred to as spin waves with their corresponding quasi-particles called magnons. Spin waves have attracted significant interest with respect to their underlying fundamental physics and their technological potential. The field of spin waves in magnetic materials nowadays is called magnonics and investigates the transmission, storage and processing of information with packages of spin waves. Spin waves display a variety of dispersion characteristics, that can be varied, for example by the choice of the magnetic material, the sample geometry, and the orientation and strength of the applied bias magnetic field. The discovery of monocrystalline yttrium iron garnet ($\text{Y}_3\text{Fe}_5\text{O}_{12}$), also called YIG, was of significant importance for the utilisation of magnons as information carriers, due to its low magnetic damping constant and long path lengths in the microwave regime [1, 6]. Owing to the progress in cryogenics and ultra-sensitive microwave technology, first steps towards the investigation of individual magnons are possible and enable access to the new field of quantum magnonics. Single magnons promise a path towards hybrid quantum systems with their potential to coherently combine quantum systems across a wide frequency range like photons [2], phonons [7] or fluxons [8], leading to applications in fields such as quantum simulation, quantum sensing, quantum communication, and quantum computing [2]. The rising interest in quantum magnonics is also established at the University of Vienna, with the Nanomagnetism and Magnonics research group dedicating a new laboratory equipped with a BlueFors LD250 cryogen-free dilution refrigerator system coupled to a superconducting vector magnet to this research direction. The access to the millikelvin temperature regime together with high-frequency microwave technology will allow further research on a single magnon level as inelastic scattering events with thermal magnons can be eliminated [3]. This first section will familiarise the reader with the most basic terms and concepts of the field of magnonics via an introduction to magnetism, spin waves, and the rising interest into single magnons. Comprehensive information to the theoretical background of the fields of magnetism and magnonics can be found in further literature (see [1, 6, 9–16]).

1.2. Introduction to Magnetism

In a simplified view, solid materials can be distinguished into two classes: those that contain atoms or ions with permanent magnetic moments and those that do not. Magnetic properties of materials are discussed with respect to the magnetic susceptibility χ , which is defined as

$$\mathbf{M} = \mathbf{M}_0 + \chi \mathbf{H} \quad \chi = \frac{M}{H}, \quad (1.1)$$

with the magnetisation \mathbf{M} , the saturation magnetisation \mathbf{M}_0 and the applied field \mathbf{H} . Materials without permanent magnetic moments respond to applied magnetic fields with an opposed magnetisation and are called diamagnetic [13]. All materials, irrespective of the net magnetic moment, exhibit this behaviour to a certain degree, but the diamagnetic susceptibility in general is very small and therefore dwarfed by the other contributions to χ . Diamagnetism is dominant in noble gases like He and Ne, in polyatomic gases like N₂ and almost all organic compounds [10]. Paramagnetic materials contain permanent magnetic moments but no spontaneous magnetisation \mathbf{M}_0 , as the moments are randomly oriented in thermal equilibrium without an applied magnetic field. Ferromagnets are materials with permanent spontaneous magnetisation below a critical temperature, the Curie temperature T_C . This phenomenon is based on magnetic domains in ferromagnets, where magnetic moments are aligned within small areas even without an external field and change direction rapidly at boundaries between such domains. The interaction giving rise to this spontaneous magnetic moment is of quantum mechanical origin and called exchange interaction [9]. Without an applied external magnetic field, the domains orient themselves so that they minimise the net magnetic moment of the macroscopic structure. In some materials this orientation of the magnetic domains leads to the line up of adjacent moments along opposite directions. The long range order in this case can be described by two ferromagnetic sublattices. If the net magnetisation of these sublattices is equal, the material is referred to as an antiferromagnet and in the case of unequal net magnetisation as a ferrimagnet. One of the most investigated materials in the field of magnonics is monocrystalline yttrium iron garnet (YIG) and belongs to the class of ferrimagnets with two sublattices. At nonzero temperatures thermal fluctuations disturb spontaneous magnetisation and long range magnetic order, which destroys the magnetic order at high enough temperatures. For ferromagnets and ferrimagnets, this transition temperature is called Curie temperature and Néel temperature for antiferromagnets. When investigating ferromagnetic microstructures, four energy contributions should be taken into account, namely the Zeeman energy E_{Zee} , the dipole-dipole or demagnetisation interaction energy E_{dip} , the exchange energy E_{ex} and the magneto-crystalline anisotropy E_{an} [13]:

$$E = E_{Zee} + E_{dip} + E_{ex} + E_{an}. \quad (1.2)$$

While the Zeeman energy and the dipole-dipole interaction energy can be described by classical magnetostatics, the exchange energy and the magneto-crystalline anisotropy have a quantum mechanical origin. The minimisation of the Zeeman energy contribution aligns magnetic moments parallel to the field lines of an external magnetic field and can be defined as

$$E_{Zee} = -\mu_0 \int_V M_0 \mathbf{m} \cdot \mathbf{H}_{Zee} d\mathbf{x}^3, \quad (1.3)$$

where μ_0 is the vacuum permeability, M_0 is the saturation magnetisation, \mathbf{m} is the atomic magnetic moment and \mathbf{H}_{Zee} is the applied external field. The dipole-dipole interaction energy aims to macroscopically demagnetise states and leads to antiparallel magnetisation configuration,

$$E_{dip} = -\frac{\mu_0}{2} \int_V \mathbf{m} \cdot \mathbf{H}_{dip} d\mathbf{x}^3, \quad (1.4)$$

with the demagnetisation field \mathbf{H}_{dip} . In ferromagnets, spins are subject to the exchange interaction that favours a parallel spin alignment and can be described as

$$E_{ij}^{ex} = -J \mathbf{s}_i \cdot \mathbf{s}_j, \quad (1.5)$$

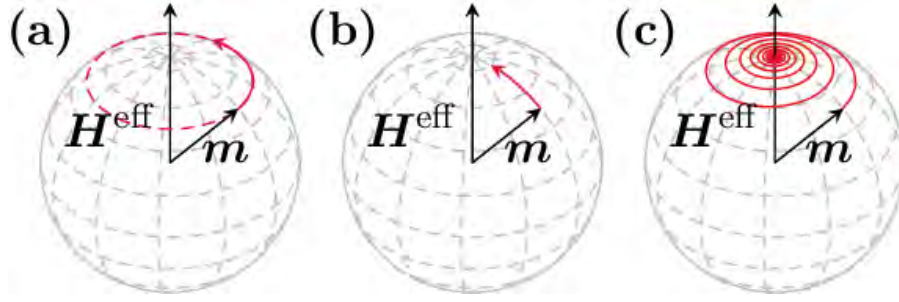


Figure 1.1.: Contributions to the motion of a magnetic moment in an external magnetic field with (a) the precessional motion (b) the dissipative motion and (c) the combined precessional and dissipative motion (taken from [11]).

with the exchange integral J and the spins \mathbf{s} . The magneto-crystalline anisotropy E_{an} aligns magnetic moments along preferable directions in crystalline structures (often referred to as easy axis) [11]. When placed in a static magnetic field under an angle, a magnetic moment starts to precess around the effective field \mathbf{H}_{eff} , which can be described with the Landau-Lifshitz-Gilbert equation (LLG)

$$\frac{d\mathbf{M}}{dt} = -\gamma\mu_0\mathbf{M} \times \mathbf{H}_{\text{eff}} + \frac{\alpha}{M_0}\mathbf{M} \times \frac{d\mathbf{M}}{dt}, \quad (1.6)$$

where γ is the gyromagnetic ratio and α is the Gilbert damping constant. The first term of equation 1.6 describes the precessional motion and the second term the damping part of the movement, which causes the magnetisation to align back to the direction of \mathbf{H}_{eff} , resulting in spiral-like motion (see Fig. 1.1) [17].

1.3. Spin Waves

Spin waves are collective excitations of the electron spin system in magnetic materials and depend on a wide range of parameters, including intrinsic material parameters such as the damping constant α and the sample shape, or external factors like the orientation and magnitude of an applied bias magnetic field. Of all materials, monocrystalline yttrium iron garnet or YIG has the lowest intrinsic spin-wave damping of any known practical experimental material and allows spin-wave propagation to be studied over centimeter distances. As spin waves are commonly studied in thin films or strips, that are in plane magnetised by an external magnetic field, the geometry of the waveguide, together with the saturation magnetisation M_0 and the the applied magnetic field \mathbf{H}_0 , are the key parameters that define the dispersion relation of spin waves [1, 6]. Spin waves can be classified with respect to their dispersion relation, with long range dipole-dipole interaction and short range exchange interactions as the main contributors to the spin-wave energy. These energy contributions lead to three characteristic regimes of spin-wave propagation: dipolar spin waves, dipolar-exchange spin waves and exchange spin waves (see Fig. 1.2). At small wavenumbers ($k < 1 \times 10^{-4} \text{ rad cm}^{-1}$), exchange contributions can be neglected and spin-waves propagate in the dipolar or magnetostatic regime. If the wavenumbers are large ($k > 1 \times 10^5 \text{ rad cm}^{-1}$), exchange contributions dominate the energy associated with the excitation and the corresponding spin waves are called exchange spin waves with $f \propto k^2$. In the intermediate region of dipole-exchange spin waves, the excitation is

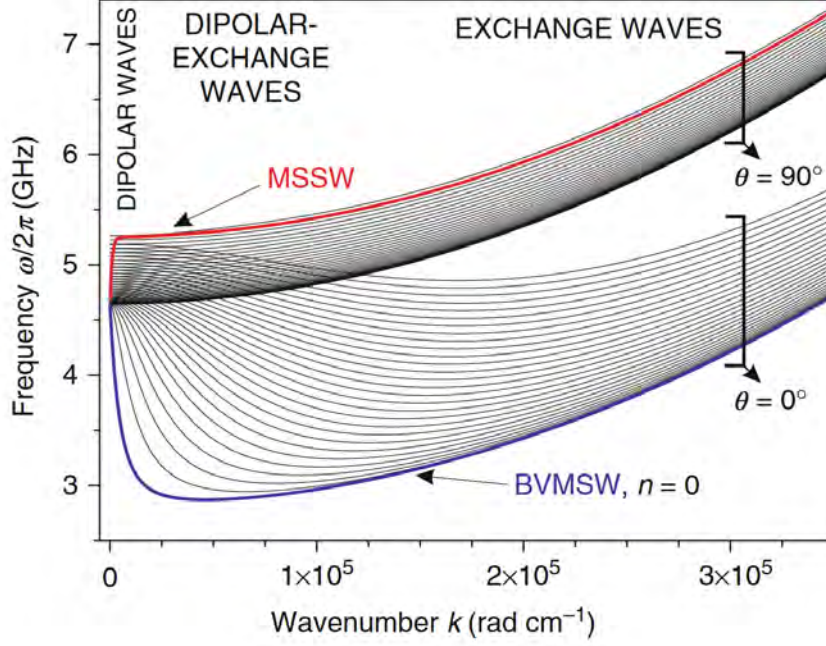


Figure 1.2.: Dispersion curve of a 5 μm thick YIG film at an applied bias magnetic field of 100 mT. Θ is the angle between the wave vector and the magnetisation. The mode number is indicated by n , with the principle mode $n = 0$ of the magnetostatic surface spin wave configuration (MSSW) in red and the backward volume magnetostatic spin wave (BVMSW) in blue (taken from [15]).

associated with both interactions. The spin-wave dispersion in the dipolar regime is strongly influenced by the angle Θ between the propagation direction of the spin wave (given by \mathbf{k}) and the magnetisation. Spin waves that propagate in films magnetised out of plane ($\Theta = 90^\circ$) are called forward volume magnetostatic spin waves (FVMSWs). In the case of in-plane magnetised films, two distinct modes can propagate: magnetostatic surface spin waves (MSSWs) at $\Theta = 90^\circ$, which are also referred to as Damon-Eshbach spin waves, and backward volume magnetostatic spin waves (BVMSWs) at $\Theta = 0^\circ$. The slope of the BVMSW, and therefore the group velocity $v_g = \partial f / \partial k$, is negative (see Fig. 1.2). Due to their dispersion characteristics, BVMSW exhibit counter-propagating group and phase velocities [15]. The dispersion relation of MSSWs and BVMSWs can be analytically calculated with equation 1.7 and 1.8 (see [stancil2009]):

$$f_{\text{MSSW}} = \sqrt{\left(f_{\text{H}} + \frac{f_{\text{M}}}{2}\right)^2 - \left(\frac{f_{\text{M}}}{2}\right)^2 \exp(-2kd_0)}, \quad (1.7)$$

$$f_{\text{BVMSW}} = \sqrt{f_{\text{H}} \left(f_{\text{H}} + f_{\text{M}} \frac{1 - \exp(-kd_0)}{kd_0} \right)}. \quad (1.8)$$

Here, $f_{\text{H}} = \gamma\mu_0 H_0 / 2\pi$ with the external bias field H_0 , $f_{\text{M}} = \gamma\mu_0 M_0 / 2\pi$ with the satur-

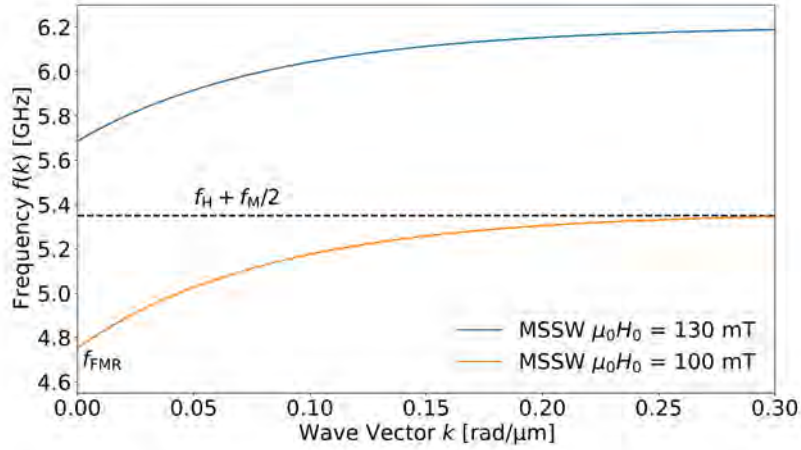


Figure 1.3.: Dispersion curve of a $70 \text{ mm} \times 2 \text{ mm} \times 5.65 \text{ } \mu\text{m}$ YIG film for the MSSW configuration. The dispersion relation was calculated analytically for the lowest order thickness mode with equation 1.7 for external fields $\mu_0 H_0 = 100 \text{ mT}$ (orange) and $\mu_0 H_0 = 130 \text{ mT}$ (blue).

ation magnetisation M_0 , k is the wave vector, and d_0 is the film thickness. A detailed derivation of this formulas can be found in [12]. Fig. 1.3 displays the dispersion relation of a $70 \text{ mm} \times 2 \text{ mm} \times 5.65 \text{ } \mu\text{m}$ YIG film on a $500 \text{ } \mu\text{m}$ thick GGG substrate for the MSSW configuration. The dispersion curve was calculated with equation 1.7 for wave vectors up to $0.8 \text{ rad } \mu\text{m}^{-1}$ and the bias magnetic fields 100 mT and 130 mT . As indicated, the dispersion curve and the spin-wave frequency can be shifted by a change in the external magnetic bias field H_0 . The MSSW frequency in the low wave vector limit is equal to the ferromagnetic resonance (FMR) frequency f_{FMR} and balances at the value $f_{\text{H}} + f_{\text{M}}/2$ for increasing k . The FMR frequency can be analytically calculated as

$$f_{\text{FMR}} = \sqrt{f_{\text{H}}(f_{\text{M}} + f_{\text{H}} + f_{\text{a}})} = \frac{\mu_0 \gamma}{2\pi} \sqrt{H_0(M_0 + H_0 + H_{\text{a}})}, \quad (1.9)$$

with the additional anisotropy field H_{a} (see supplementary [18]). A common way to measure the dispersion curve of spin waves in thin-film samples is space and time resolved Brillouin light scattering (BLS) spectroscopy (e.g. [4, 19]). However, BLS measurements prove to be extremely difficult in a cryogenic environment, due to the limited space in cryostats and the induced heat loads. All-electrical measurements, like propagating spin-wave spectroscopy (PSWS), therefore often are preferable in cryogenic environments [20]. PSWS is a technique that uses a microwave source and detector, typically a vector network analyser (VNA), connected to a pair of microwave antennas that are separated by a gap, to excite and detect propagating spin waves in a thin-film waveguide sample. If the sample is magnetically saturated, the spins are oriented parallel to the applied external magnetic field. A microwave signal that is applied to one of the two antennas, generates an Oersted magnetic field. The components of this Oersted field, which are not oriented parallel along the bias field, exert a torque on the spins, with a precessional amplitude exceeding the thermal contribution (see equation 1.6). Under proper conditions of frequency, magnetisation direction, and bias field amplitude, spins at the antenna

interact with their nearest neighbours and support spin-wave propagation. When the spin wave arrives at the other antenna, it induces an AC-current and therefore can be detected [1, 6]. The main types of antennas used in PSWS measurements are microstrip, u-shaped and coplanar waveguide (CPW) antennas [20]. The antennas can be either placed on a printed circuit board (PCB), or directly patterned on the sample by different lithography techniques (see [4]). If a VNA is used as microwave source and signal detector, the S -parameter spectrum can provide information about the spin-wave mode, its dispersion characteristics, the FMR-frequency of the investigated sample, and the k -vectors that can be excited with the used antennas. Via subtraction of the nonmagnetic background, antenna crosstalk can be filtered out. Typical transmission spectra S_{21} of BVMSWs and MSSWs, recorded during PSWS measurements, can be found in [1, 6].

1.4. Quantum Magnonics

The field of magnonics examines the excitation, propagation, control, and detection of spin waves in magnetic materials. These spin excitations can be modulated either passively by patterning certain structures and adapting magnetic properties, or actively by applying external magnetic fields [16].

Although many aspects of the dynamics of spin waves in that manner can be well described in a quasi-classical model of wave excitations, recent research demands an appeal to their corpuscular character, namely the spin-wave quantum called magnon [15]. The quantum nature of magnons, and the physics of entangled magnonic or hybrid quantum states, establishes as a novel research direction in the field of magnonics. The conversion of coherent signals between different elementary excitations in the microwave frequency range represents a fundamental building block in memory, transport, and sensing applications. A challenge that is faced here, is the connection of different qubit systems to superconducting circuits. With photons having frequencies in the THz-range and typical transition energies of ultra cold atoms below 1 GHz, interfacing with superconducting qubit systems is challenging [21]. Therefore, interest in magnetic materials for quantum devices is motivated by their range of resonance frequencies in the low GHz-region, which is also commonly used in superconducting quantum circuits. Additionally, the frequencies of magnons can be tuned by a bias magnetic field and thus be brought into resonance with other systems. The utilisation of magnons as quantum transducers between different qubit systems therefore could be suggested.

Further, magnons can be coupled to microwave photons via Zeeman splitting and to optical photons via Brillouin light scattering [22]. A microwave cavity hosting a magnetic material, like for example YIG, can be used to increase the coupling strength g_{mw} and push the magnons and the photons into the strong coupling regime, where their modes hybridise, signaled by an avoided crossing at resonance (see [3]). The coupling of magnons to optical photons occurs via Brillouin scattering, where light is scattered by the absorption or creation of a magnon. Compared to microwave photons, where experiments are able to reach the strong coupling regime, the coupling of optical photons to magnons is still in the weak coupling regime, as the coupling strength is smaller than the typical decay rates [21]. The strong coupling of magnons and microwave cavities was already utilised together with superconducting qubits in the detection of single magnons for uniform precessions in a YIG sphere, as reported in [2]. The path to operations with single propagating magnons, however, still requires further research. The excitation of single magnons is believed to be impossible without the use of cryogenic

techniques, due to the high density of thermally excited magnons at room temperature. Therefore, research focuses on the realisation of efficient single magnon sources and detectors, able to be operated at millikelvin temperatures. Up to now, superconducting systems, based on nonlinear Josephson circuits, seem to be the most promising solutions [21].

The main goal of this master thesis is the realisation and characterisation of a propagating spin-wave spectroscopy measurement setup, able to operate at base temperatures below 100 mK. Therefore, a Bluefors LD250 cryogen-free dilution refrigerator system was combined with a vector magnet and an Anritsu VectorStar VNA measurement system, rated for signals up to 40 GHz. Together with specially designed high-frequency PCBs, this laboratory setup will allow the excitation and detection of spin waves at cryogenic temperatures in various different samples, creating a measurement platform for future experiments in the field of quantum magnonics. To achieve this goal, the thesis is organised in the following structure:

- **Chapter 2** starts with the discussion of cryogenics and the Bluefors LD250 cryogen-free dilution refrigerator system. Afterwards, we will continue with an introduction to the basic concepts of radio frequency technology and transmission lines, that are crucial to the design of high-frequency circuits and the recording of transmission spectra. The chapter will be concluded by the discussion of a designed high-frequency PCB, able to host different samples in PSWS experiments, and the concept of finite element frequency-domain studies, that were used to analyse parts of the PCB.
- **Chapter 3** comments on the installation and calibration of the dilution refrigerator system. The experimental setup, containing the dilution refrigerator, a superconducting vector magnet, and a VNA measurement system, was characterised by the analysis of the temperature curve during the cool down, the transmission losses in the internal transmission lines of the cryostat, and the temperature changes during the operation of the superconducting vector magnet.
- **Chapter 4** covers the computational analysis of the high-frequency transmission lines of the designed PCB and an experimental proof of the PCBs functionalities. Further, prospects of the high-frequency PCB are discussed, including the fabrication of coplanar waveguide samples for more detailed future experimental analysis of the PCB.
- **Chapter 5** is discussing first PSWS measurements at millikelvin temperatures for MSSWs. The results are compared to studies performed in an electromagnet-based room temperature setup and analysed with respect to their dispersion curves.
- **Chapter 6** concludes the characterisation of the introduced cryogenic PSWS setup and the first recorded results. Additionally, the chapter contains an outlook to possible improvements of the dilution refrigerator system and future experiments, containing magnons and their implementation to hybrid quantum systems.

2. Experimental and Computational Methods

In this chapter, fundamental experimental and computational techniques are presented. We begin with the concept of a dilution refrigerator (DR) by a general introduction to cryogenics, and the theoretical background of a DR, followed by a detailed discussion of the Bluefors cryogen-free dilution refrigerator system. Afterwards, a basic introduction to radiowaves, transmission lines, and scattering parameters prepares the reader for the discussion of the design of a high-frequency PCB. The principle structure and the idea behind the design of the PCB is discussed. The chapter is concluded with an overview to finite element frequency-domain simulation.

2.1. Concept of a Dilution Refrigerator System

2.1.1. Introduction to Cryogenics

Cryogenics can be defined as the science and technology of temperatures below 120 K [23]. The limit temperature of 120 K includes the normal boiling points of the main atmospheric gases (see table 2.1) and also includes methane as an important constituent of natural gas, which represents one of the main industrial applications of cryogenics together with the liquefaction and separation of gases [24]. Generalised, cryogenics can also be defined as the branch of physics which deals with the production of very low temperatures and their effect on matter [25].

Cryogenic technology finds widespread applications in industrial purification and liquefaction of gases such as helium and nitrogen, the production of inert gases, aerospace industry, sensor technology, medical applications, and refrigeration purposes [27]. The latter generally makes use of cryogenic fluids like helium and nitrogen. Due to the boiling point of 4.2 K (see table 2.1), He is the only atmospheric gas that is liquid at very low temperatures and is therefore widely used, whereas N often finds applications because of its wide availability and

Element	Normal Boiling Point [K]	Critical Temperature [K]
Methane	116.6	190.6
Oxygen	90.2	154.6
Argon	87.3	150.7
Nitrogen	77.3	126.2
Neon	27.1	44.4
Hydrogen	20.4	32.9
Helium	4.2	5.2

Table 2.1.: Characteristic temperatures of cryogenic fluids and the main atmospheric gases at 1013.25 mbar (taken from [26]).

relative low costs [24]. Cryogenic technology also is utilised in scientific experiments to achieve and maintain cryogenic temperatures. Complex refrigeration systems are used in the fields of superconductivity, quantum sensing, and quantum information [28, 29] to prepare well defined environments at temperatures below 120 K. All these applications exploit the thermodynamic properties of cryogenic fluids, to achieve cryogenic temperatures [30].

2.1.2. Dilution Refrigerators

The theoretical principle of a DR was first proposed in the early 1950s by Heinz London and experimentally realized at Leiden University in 1964. A year later, in 1965, the first dilution refrigerator using a $^3\text{He}/^4\text{He}$ -mixture was built at the university of Manchester. In 1966 the first commercial DR was developed together with Heinz London in Oxford, which achieved a base temperature of 200 mK. This opened the door to cooling beyond the known liquid helium temperatures. Today, base temperatures below 10 mK can be achieved with commercially available DR systems [31]. It is possible to achieve temperatures below 10 mK without any moving mechanics at the low temperature stages. A DR utilises a mixture of the two helium isotopes, ^3He and ^4He , to obtain cooling. To run the dilution refrigerator's cooling cycle, a starting temperature of liquid helium needs to be obtained with another cooling system first [32], which in the early days was achieved by a liquid bath of He and nowadays is realised with a pulse tube cooler (PTC). As such systems do not require liquid He, they are often referred to as dry or cryogen-free dilution refrigerators [31].

Pulse Tube Coolers

PTCs use oscillatory compression and expansion of a gas within a closed volume to remove heat and therefore achieve cooling. The advantage to other cryocoolers, for example Stirling machines, is that no mechanical displacers or motorised valves are needed for the operation of a PTC, which significantly reduces vibrations at the cold end of the PTC. Fig. 2.1 depicts a schematic diagram of a conventional PTC design with a compressor, a rotary valve, the regenerator, the pulse tube, a buffer, and three heat exchangers as the main components. The compressor, together with the rotary valve, is able to create an alternating pressure level at the connection to the regenerator. The regenerator is filled with a porous material that normally contains stacked layers or spherical particles with a sufficiently high heat capacity and low thermal conductivity, which receives heat during the compression phase and delivers it back when the gas is expanding. The pulse tube is a hollow tube, normally made of stainless steel with a uniform temperature gradient between its warm and cold end, that rejects heat to flow back to the cold end together with the buffer [33]. The operation of the PTC relies on an oscillatory high pressure signal from the compressor, that densifies the gas (in most cases helium) at the hot end of the pulse tube, which leads to an increase in temperature at the hot end heat exchanger (HHX). The after cooler (AC), which is the heat exchanger at the warm end of the regenerator, pre-cools the incoming gas of the compressor and reduces the temperature at the HHX in the pulse tube, causing the regenerator to supply low temperature gas more efficiently. Once the rotary valve connects the low pressure line to the regenerator, the compressed gas will expand again, which leads to a temperature decrease at the cold end heat exchanger (CHX). The gas flow passing through the regenerator will take up the stored heat and flow back to the compressor, where it is cooled again. At this point the cycle can start again [33].

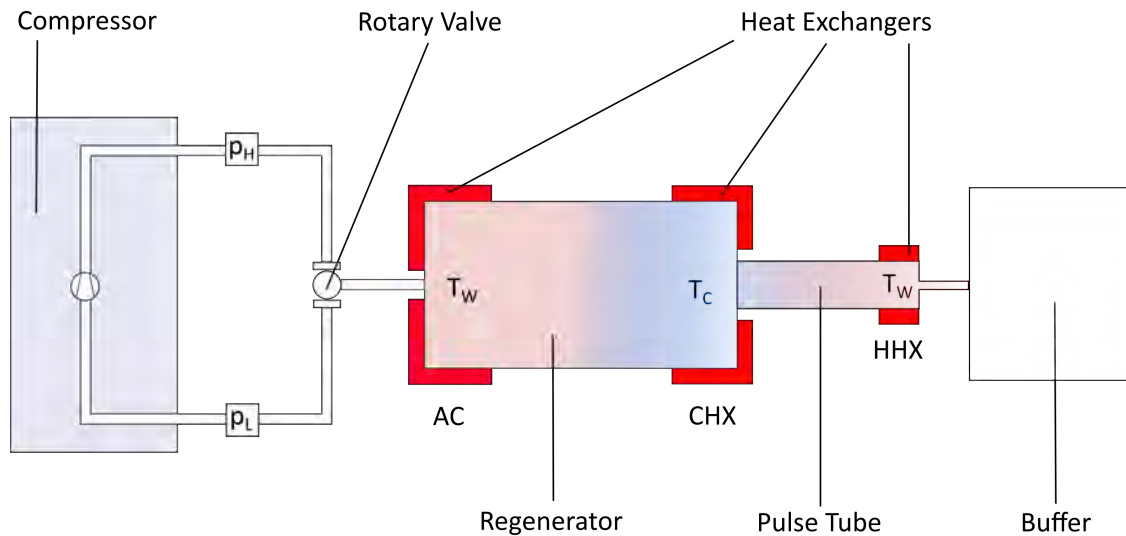


Figure 2.1.: Schematic diagram of a Pulse Tube Cooler with the heat exchangers indicated as After Cooler (AC), Cold End Heat Exchanger (CHX) and Hot End Heat Exchanger (HHX). Further explanation can be found in the text (following [33]).

Dilution Unit

The dilution unit (DU) uses the intrinsic properties of a $^3\text{He}/^4\text{He}$ -mixture to achieve cooling. Pure ^4He undergoes a phase transition to a superfluid at 2.17 K, as it obeys Bose-Einstein statistics with a nuclear spin of 0. ^3He on the other hand, obeys Fermi statistics with a nuclear spin of 1/2. As indicated in the phase diagram of the $^3\text{He}/^4\text{He}$ -mixture (see Fig. 2.2), this leads to a phase transition between a normal fluid and a superfluid (λ -line). As the Pauli exclusion principle prevents ^3He from undergoing a phase transition until very low temperatures, at which spins pair up and ^3He also obeys Bose-Einstein statistics, the λ -line shifts to lower temperatures for higher concentrations x of ^3He in the mixture [31]. At temperatures below 0.8 K, the $^3\text{He}/^4\text{He}$ -mixture separates into two phases, a ^3He -rich phase (concentrated phase) and a ^4He -rich phase (dilute phase) [32].

Approaching 0 K temperature, the concentrated phase becomes pure ^3He , while the dilute phase still contains 6.4% of ^3He . This finite solubility is the result of a stronger bonding force of the ^3He -isotope in ^4He . Due to the stronger bonding, ^3He atoms prefer to stay in ^4He until a concentration of 6.4%, as the chemical potential at this point equals that of ^3He in pure ^4He . If therefore ^3He atoms are removed from the diluted phase, atoms from the concentrated phase will occupy the vacant energy states. As displayed in Fig. A.1 (see appendix), the enthalpy of ^3He is higher in ^4He than in pure ^3He , as ^3He behaves like a Fermi gas in ^4He . Because of the enthalpy change, the crossing of the phase boundary costs energy and can be used for cooling [31]. Fig. 2.3 depicts the main parts of a DU, with the so called condensing line, the mixing chamber, the still pumping line, and the distiller ("still"). As ^4He has a higher atomic mass than ^3He (see [34] p.734), the dilution phase collects in the mixing chamber. In the condensing line the pre-cooled condensed phase is forced to pass a flow impedance, which, together with several heat exchangers, leads to condensation of the gas above the mixing chamber. Through the still pumping line, the mixing chamber is connected to the still,

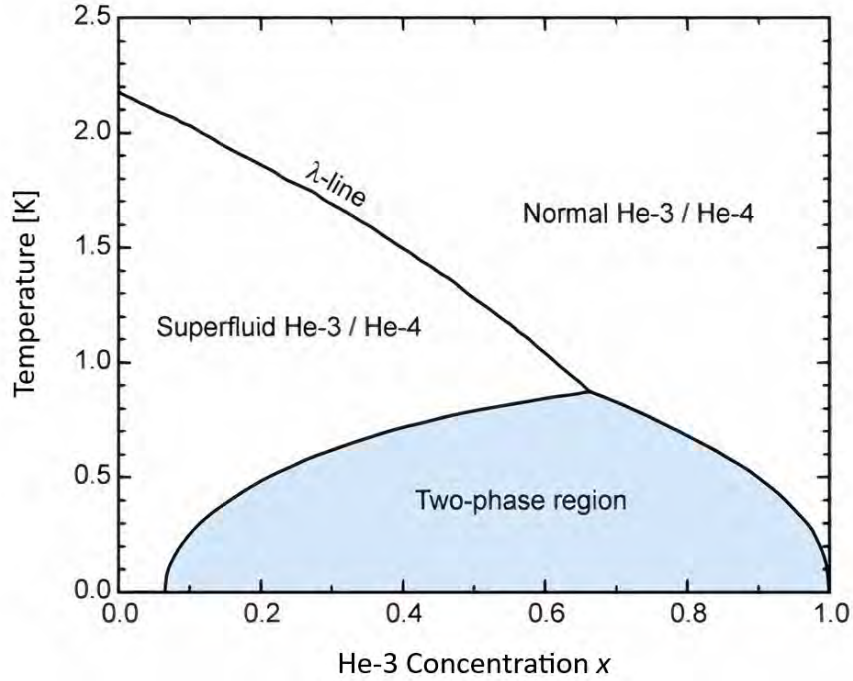


Figure 2.2.: Phase diagram of ^3He in ^4He for different concentrations x . Along the λ -line the $^3\text{He}/^4\text{He}$ -mixture transitions from a normal fluid to a superfluid. Below 0.8 K, the mixture separates into a ^3He -rich concentrated phase and a ^4He -rich dilution phase (taken from [32]).

where ^3He is distilled from the dilution phase, as ^3He has a higher vapour pressure at near 0 K temperatures than ^4He (see Fig. A.2 in the appendix). The distiller is connected to a heater, as the temperature and therefore the vapour pressure otherwise would decrease too fast to provide sufficient circulation. If, on the other hand, the still temperature is too high, the difference in vapour pressure between ^3He and ^4He gets too small and the efficiency of the dilution process will be reduced. These two mechanisms result in an optimal still temperature of 0.7 K to 0.8 K. As ^3He is distilled from the dilution phase, the ^3He concentration decreases, which ultimately leads to an osmotic pressure gradient between the mixing chamber and the distiller. Therefore, ^3He is pulled from the mixing chamber to the still and ^3He atoms from the condensed phase will cross the phase boundary to fill the energetically favourable vacancies. Due to the enthalpy difference, this boundary crossing consumes energy, and thus heat is taken from the surrounding area, resulting in cooling of the mixing chamber. The associated cooling power is determined by the enthalpy difference ΔH and the ^3He flow rate $n_{\text{H}3}$ [31].

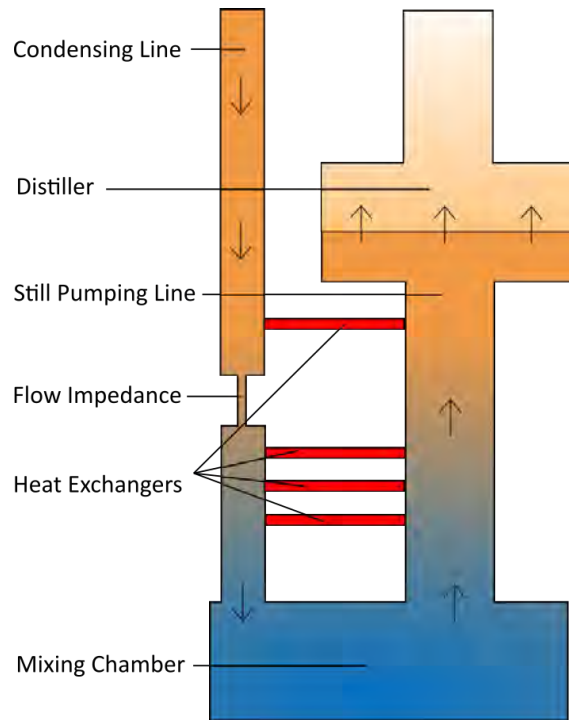


Figure 2.3.: Schematic of the main components of a dilution unit. The condensed phase is indicated in orange, the dilution phase is indicated in blue and the flow direction is depicted with black arrows. Further explanation can be found in the text (following [32]).

2.1.3. BF-LD250 Cryogen-Free Dilution Refrigerator System

This section will focus on the technical realisation and specifications of the examined DR, namely the Bluefors LD250 cryogen-free dilution refrigerator system. The basic components of the DR can be summarised as the gas handling system (GHS), the control unit, and the cryostat itself. Additionally, the examined system is equipped with a superconducting vector magnet [32].

Gas Handling System

The GHS contains all pumps, pumping lines, and valves that are necessary to operate the system. The GHS is divided into two main circuits that can be interconnected at certain valves: the main circulation circuit and the service manifold. A detailed flow diagram is depicted in Fig. 2.4. The main circulation circuit is actuated by an Edwards nXDS15i scroll pump (scroll 1 in Fig. 2.4) and a Pfeiffer HiPace 400 turbo pump (turbo 1 in Fig. 2.4), while the service manifold is operated by an Agilent SH-110 scroll pump (scroll 2 in Fig. 2.4) with an additional Agilent V301 turbo pump (turbo 2 in Fig. 2.4). The pumps in the service manifold are mainly used for pressure regulation and vacuum pumping. Therefore, the GHS also contains a Vent port and an AUX port, which are connected to atmospheric pressure conditions. A TEST port allows the connection to a leak detector. The pumps of the circulation cycle are needed to start, maintain, and end the dilution cycle [32].

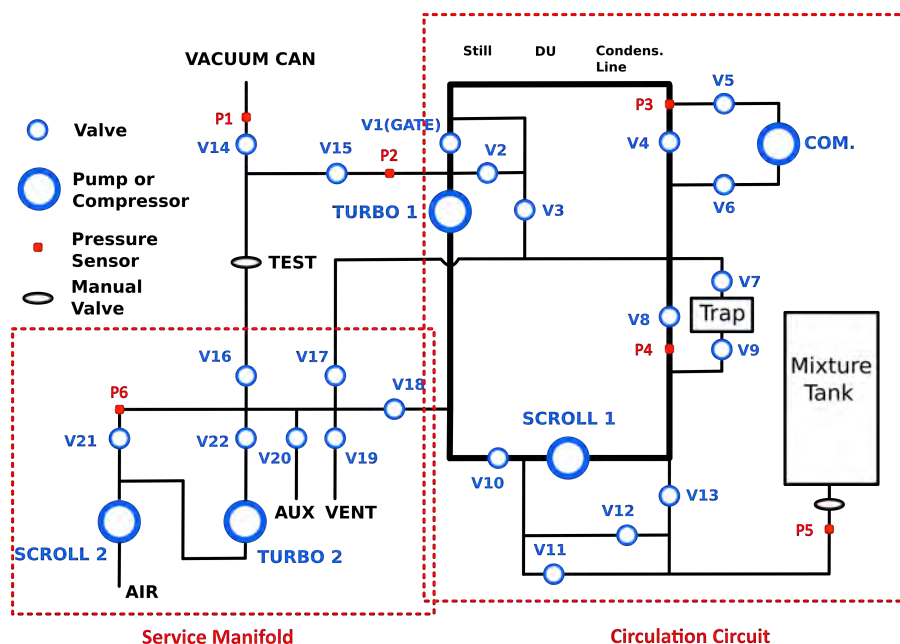


Figure 2.4.: Flow diagram of the gas handling system containing the main valves (labeled from V2 to V22), pumps, and pressure sensors (labeled from P1 to P6) in the layout of the main board on the control unit. The service manifold and the circulation circuit are indicated with red boxes (following [32]).

Control Unit

The control unit allows the user to operate the DR manually by switching the main valves, pumps, and compressors over a central relay board. Each control channel of the relay board can be switched either by the buttons directly on the control unit or by a computer via a USB connection. The system is delivered with a Lab-View software interface, which enables the user to load and run control scripts to automate steps in the operation of the DR. The control unit is also equipped with a 6-channel pressure control unit for the readout of pressure gauges at the GHS and displays the values directly and in the software [32].

Cryostat

The cryostat is situated inside of a vacuum can and connected to the GHS by the still pumping line, the ^3He -return line, that leads to the mixture tank, and the pumping line of the vacuum can. All these lines are electrically isolated from the GHS. The cryostat itself is connected to a separate ground. As depicted in Fig. 2.5, the inner layout of the cryostat can be sectioned into four different thermal stages, namely the 50 K-flange on top, followed by the quasi 4 K-flange, the still-flange, and the mixing chamber-flange (MXC) on bottom. The temperatures at each stage, the magnet, and the probe (not indicated in Fig. 2.5) are recorded via a resistance thermometer. The magnet is thermally coupled to the 4 K-flange and the probe stage is thermally connected to the MXC-flange, to cool down the inserted sample. The whole inner layout of the cryostat is situated in one common vacuum space and surrounded by a radiation shield assembly to isolate it from its surroundings. The 50 K-flange and the 4 K-flange are connected and thermally coupled to the warm and cold end of the PTC with flexible copper

braids to damp vibration. The heat exchanger at the 50 K-flange acts as a cold trap, which freezes contamination in the circulating helium gas and collects it in a separated trap that is cooled by liquid nitrogen. The 4 K-flange is thermally coupled to the cold end of the PTC and the condensing line of the dilution unit [32].

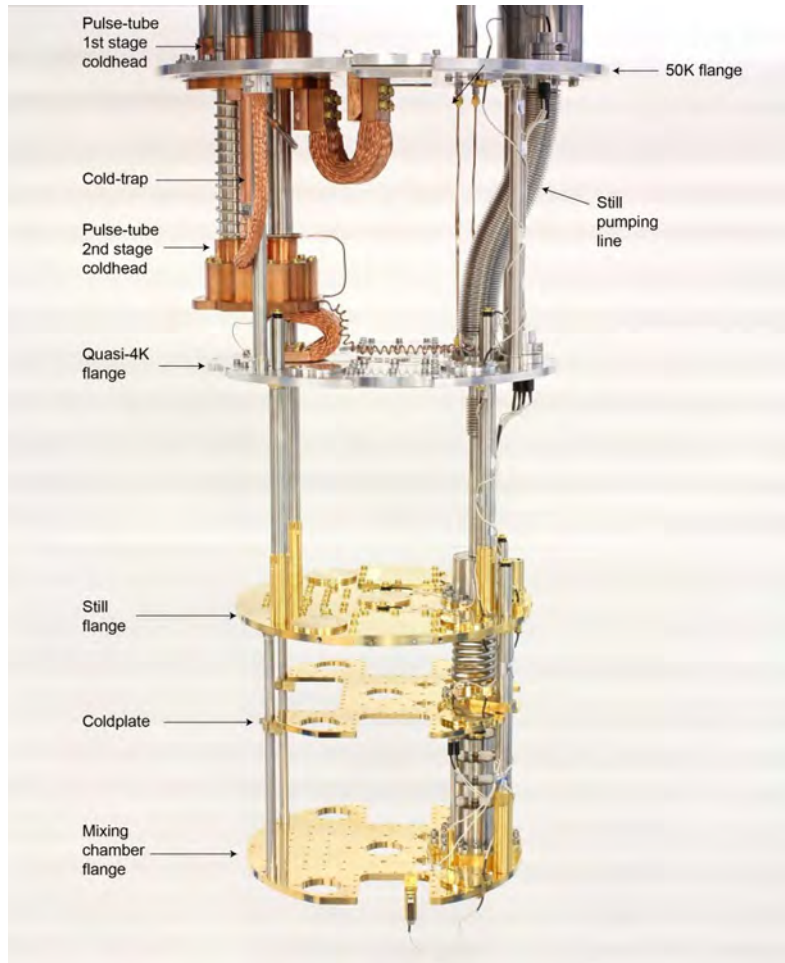


Figure 2.5.: Inner Layout of the cryostat with the 50 K-flange, the 4 K-flange, the still-flange, and the MXC-flange as the different thermal stages. The pulse tube cooler can be found on the top left and the dilution unit is located on the bottom right (taken from [32]).

Gas-gap heat switches (GGHS) are installed between the 4 K-flange, the still-flange, and the MXC-flange. As the whole system is placed inside of only one vacuum can, the heat switches are needed to thermally separate the flanges after starting the dilution cycle. After the initial pre-cooling of the system with the PTC, the heat switches break the thermal contact between the different stages to enable the operation of the DU. The GGHS consist of two copper heat exchangers at its ends that are separated by a stainless steel tube with very poor thermal conductivity. To conduct heat between the two heat exchangers, the tubes are filled with helium gas. The GGHS can be turned on, if they are filled with helium and can thermally connect the different stages. To turn the heat switches off, He is pumped with an active carbon

pump through outlets in the heat exchangers and absorbed by the active carbon. Therefore, the active carbon has to be cooled to temperatures below 10 K beforehand. The heat switches can be turned back on by small heaters that warm up the carbon, which releases the helium gas. After the pulse tube cooling pre-cooling, the dilution cycle can be started. A compressor raises the pressure of the mixture to 2 bar, before it is inserted into the condensing line. The heat exchangers at the top of the condensing line and the Joule-Thomson effect at the flow impedance lead to the condensation of the mixture due to cooling. The condensed mixture then fills the mixing chamber and parts of the distiller, with the dilution phase collected at the bottom of the MXC. The pumping of the still line now starts the dilution cycle and the pumped ^3He is returned to the condensing line [32]. The sample itself can be mounted on sample holder rods at the top of the sample insert, which are equipped with a thermometer and a heater.

Bottom-Loading Sample Exchange System

The sample exchange is based on a fully automatic load-lock system, that inserts the probes from the bottom of the cryostat. The system consists of its own control unit, a lift mechanism and a sample insert. Via the gate valve and its own pump valve, the sample exchange system can be separated from the main vacuum space in the vacuum can. The sample insert is thermally connected to the MXC-flange, the still flange, the magnet, and the 50 K-flange over several contact rings as indicated in Fig. 2.6.

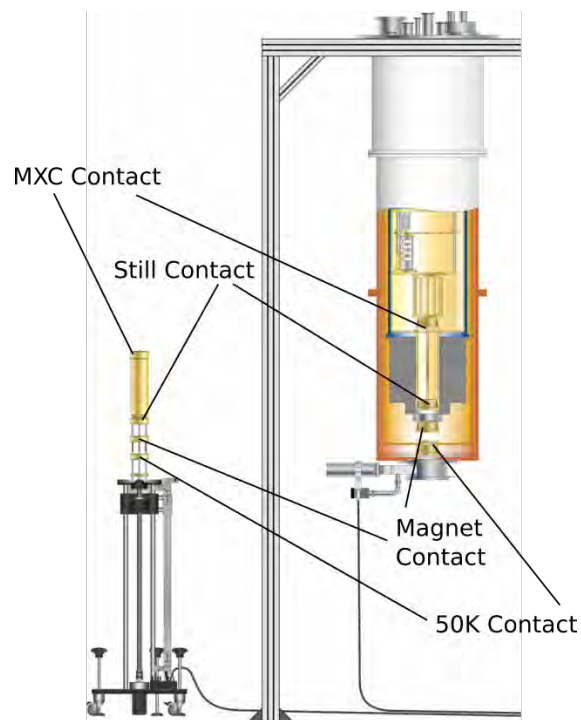


Figure 2.6.: Layout of the bottom-loading sample exchange system on the left and the cryostat on the right. The sample insert is thermally connected to the different stages in the cryostat via contact rings (taken from [35]).

The top of the sample insert hosts eight coaxial SMP ports and two Micro D-Connectors, which enable the user to apply signals to the sample [35]. Three different types of transmission lines are used to host the signal from the top plate of the cryostat to the coaxial ports at the sample insert:

- SN086: 0.86 mm SCuNi – CuNi semi-rigid coaxial line (at ports 1-4 from room temperature to the sample holder)
- SN219: 2.19 mm SCuNi – CuNi semi-rigid coaxial line (at ports 5-8 from room temperature to the 4 K-flange)
- NT086: 0.86 mm NbTi superconducting coaxial line (at ports 5-8 from the 4 K-flange to the sample holder)

To filter out noise and minimise heat dissipation in the cryostat, the 50 K-flange, the 4 K-flange, the still flange, the cold plate, and the MXC-flange are equipped with different attenuator configurations.

Multiple Axes Vector Magnet

The installed dilution refrigerator system is equipped with a superconducting vector magnet, which allows the user to apply magnetic fields at the inserted sample. The examined DR comes with a cryogen-free multiple axes vector magnet manufactured by the company AMI, which consists of three independently controlled coil sets. A solenoid coil for the principle field axis in z -direction can create magnetic fields with a magnitude of 9 T and two sets of split-coils for the x - and y -direction can create fields up to 1 T. The different coils can be operated separately or together, permitting magnetic fields of 1 T in all directions [36]. Generally speaking, a superconducting magnet utilises the absence of electrical resistivity for certain materials (in this case Niobium-tin, Nb_3Sn) below their critical temperatures to create electromagnetic fields with much larger currents than conventional electromagnets. As a constant flow of electrical current from an external power source to the superconducting coils would constantly dissipate heat, most superconducting magnets can be operated in persistent mode. This concept enables such a magnet to maintain a constant operational field even after the power source is turned off and is achieved with a heater-activated persistent-current switch (PCS). Fig. 2.7 displays a simplified circuit diagram of a persistent mode superconducting magnet. The total circuit resistance is represented by r and the magnet is indicated with the inductance of the coil L . The PCS shunts the magnet terminals (black dashed line), which ideally have to be superconducting, as the joint resistance at the terminals otherwise adds to r . The two diodes shunt the PCS to protect it in the event of a magnet quench. If a current is sent through the PCS heater, the PCS becomes resistive with a non-zero resistivity R_{pc} . The magnet can be energised via the current leads and an external power supply. Once the operating current for the desired magnetic field strength is obtained, the heater can be turned off and the PCS becomes superconducting. At this point, the circuit becomes fully superconducting (with very small internal losses) and the magnet is completely isolated from the current leads, which enables the magnet to maintain the magnetic field without an external power supply, due to the almost lossless current in the circuit [37].

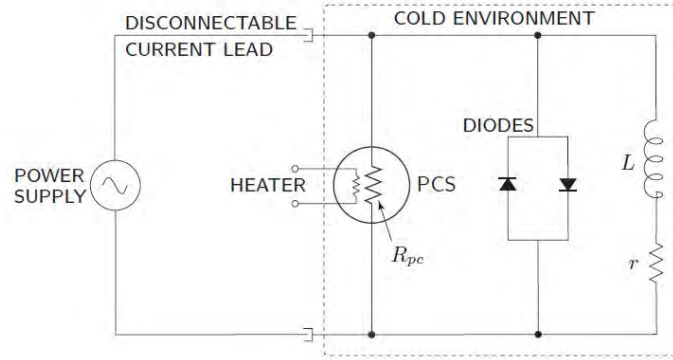


Figure 2.7.: Simplified circuit diagram of a persistent mode superconducting magnet. The magnet is represented by the inductance of the coil L , while r represents the whole circuit resistance and the resistance R_{pc} indicates the PCS. The elements enclosed inside of the dashed lines can be considered to be in the cold environment (taken from [37]).

2.2. Concepts of Radio Frequency Technology

2.2.1. Radiowaves

Radio frequency (RF) technology utilises electromagnetic wave phenomena in the frequency spectrum of 3 Hz to 300 GHz and has significantly shaped our modern society [38]. Maxwell's theory of electromagnetism and electromagnetic waves built the foundation and basis of the understanding and description of radio waves and light. The propagation of electromagnetic waves as electric and magnetic fields dependent on time and space is indicated in Maxwell's equations and the corresponding energy transfer can be described with the concept of the Poynting vector $\mathbf{S} = \mathbf{E} \times \mathbf{H}$ [39]. If an electric field changes rapidly from one static configuration to another, for example in an alternating current (AC), energy will be released by the system in the form of electromagnetic wave pulses. By modulating an AC-signal in a way, that a series of suitably spaced pulses is released, information can be carried by an electromagnetic wave [38]. In RF technology, antennas are used to transmit signals by applying modulated AC-signals and to receive radio wave signals, by detecting changes due to resonances in the local electric fields. Therefore, detection systems can be tuned to receive signals that occupy a range of frequencies (baseband), which enables many communication systems to coexist without interfering with each other. However, the receiving antenna also detects noise signals from its environment, which limits the amount of amplification at the receiving end. A good indicator for the quality of a radio wave signal is the signal to noise ratio or SNR, which is defined as the ratio between the received signal and the noise power. The noise power is strongly dependent on the range of frequencies the receiver should detect (bandwidth). As a consequence the SNR can be increased by a small bandwidth and by the filtering of unwanted signals [39]. RF technology also finds application in the study of magnetic materials by the means of FMR and PSWS spectroscopy, with the excitation and detection of resonant spin-wave modes [40].

2.2.2. Transmission Lines and Scattering Parameters

Radio waves that are propagating in free space will experience a significant reduction in amplitude after they are emitted from the source, which leads to unwanted signal loss. If the signal only needs to reach one receiver, it is desirable to transmit all the energy to this antenna. Structures that allow efficient signal transmission over long distances are referred to as transmission lines [38]. One of the most frequently used transmission line structures, the coplanar wave guide (CPW), consists of a thin metallic strip and two adjacent and parallel ground electrodes, deposited on the surface of a slice of dielectric material [41]. Additionally to the parallel ground strips, a third ground can be added on the bottom of the dielectric substrate. This configuration is referred to as grounded coplanar wave guide (GCPW). The electric field components in the GCPW are concentrated in the gaps between the signal strip and the ground layers, while the magnetic field lines revolve around the signal track [42]. A cross section of a GCPW structure together with the magnetic (blue) and electric (red) field lines is displayed in Fig. 2.8.

For transverse electromagnetic (TEM) wave propagation, transmission lines often are schematically represented by a two-wire line, as they consist at least out of two conductors (one signal and one ground line). For infinitesimal small lengths, the transmission line can be modelled as a lumped element circuit, where voltage and current do not vary significantly over the physical dimensions of the elements. Such a two-wire lumped element circuit with series resistance R , inductance L , shunt conductance G , and capacitance C for the two conductors, is sketched in Fig. 2.9 [43].

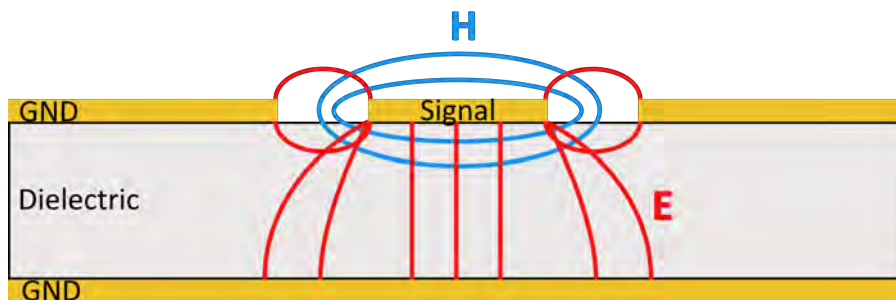


Figure 2.8.: Schematic diagram of the magnetic (blue) and electric (red) field components in a grounded coplanar wave guide configuration. The waveguide consists of a dielectric substrate between a bottom ground layer and a signal track on top, which is situated between two ground tracks. The majority of the electric and magnetic field lines are confined between the signal track and the ground layers.

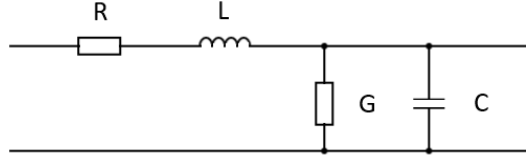


Figure 2.9.: Schematic circuit diagram of a lumped element two-wire line with series resistance R , inductance L , shunt conductance G , and capacitance C .

In the lumped circuit approximation, the characteristic impedance Z_0 of the transmission line is generally defined as the ratio between the voltage V_0 and the current I_0 amplitude. Together with the angular frequency ω along the line, the characteristic impedance can be expressed as [43]

$$Z_0 = \frac{V_0}{I_0} = \sqrt{\frac{R + i\omega L}{G + i\omega C}}. \quad (2.1)$$

Analytical methods, as discussed in [43] and online calculation tools like [44], can be used to calculate the characteristic impedance for different geometric structures. The characteristic impedance is of great importance at structural transitions, as differences in Z_0 for different sections of a transmission line lead to internal reflections and therefore transmission losses. A useful tool in the description of reflection and transmission in a N -port network is the scattering matrix, which relates the voltage amplitudes incident on the ports V_n^+ to those reflected from the ports V_n^- . In a two port network, S_{11} represents the reflected signal measured at port 1 when an incident voltage signal is applied at port 1 (vice versa for S_{22}). S_{21} represents the signal measured at port 2 when an incident voltage signal is applied at port 1 (vice versa for S_{12}). The scattering parameters can be directly measured with a vector network analyser [43].

$$\begin{pmatrix} V_1^+ \\ V_2^+ \end{pmatrix} = \begin{pmatrix} S_{11} & S_{12} \\ S_{21} & S_{22} \end{pmatrix} \begin{pmatrix} V_1^- \\ V_2^- \end{pmatrix} \quad (2.2)$$

2.2.3. High-Frequency PCB

A multilayer high-frequency PCB, with the possibility to host samples in a cryogenic environment and connectors for the application of DC and high-frequency signals up to 40 GHz, was designed within the framework of this thesis. The PCB will be part of a measurement platform for future experiments in the field of quantum magnonics. Printed Circuit Boards or PCBs are the basic building blocks of any practical electronic system, as they interconnect all the components in a circuit design [45]. During measurements in the dilution refrigerator, such a PCB will be the interface that connects the investigated sample to the transmission lines of the cryostat and the VNA. Different connectors on the PCB allow to apply and detect signals in a wide frequency range, for which the PCB contains multiple layers with different electrical potentials.

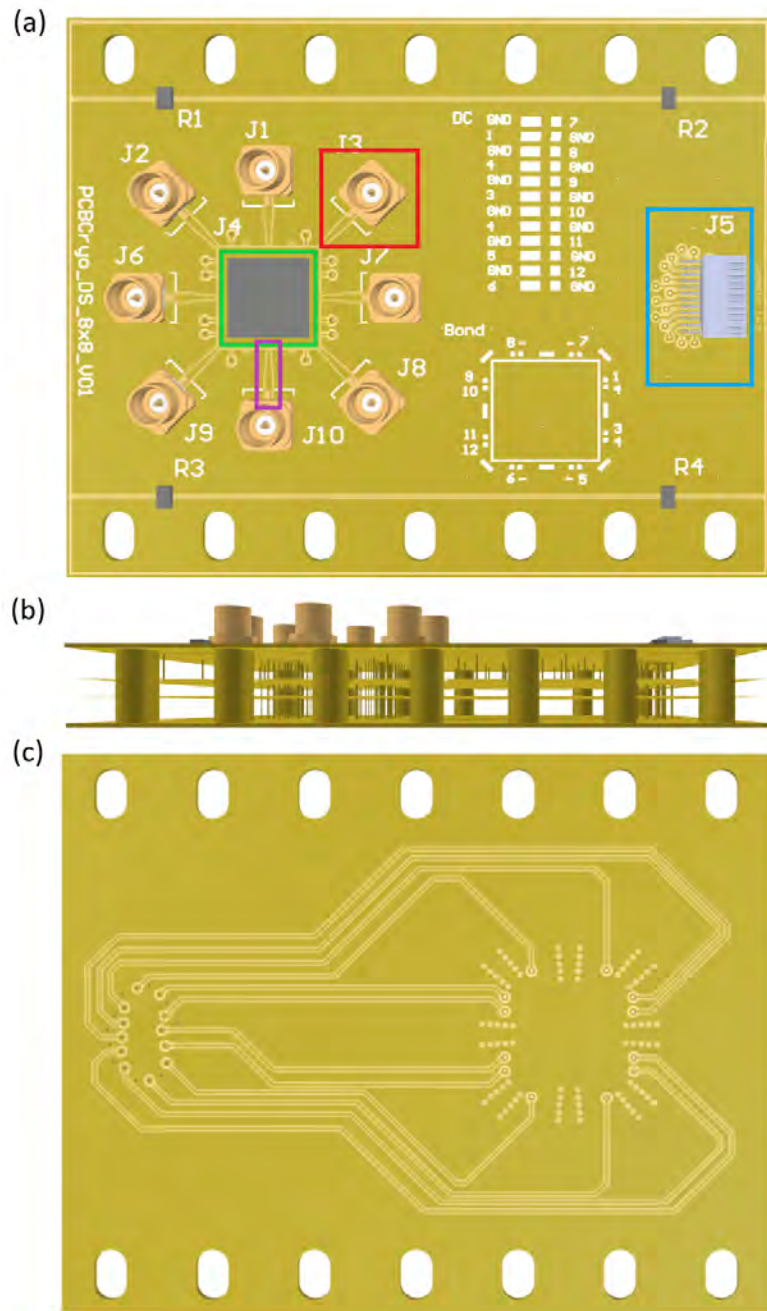


Figure 2.10.: Final PCB design, exported from the software package Altium Designer. (a) Top layer, containing a 24-pin DC connector (blue), eight SMP connectors (red), a cavity cut out for the placement of the sample (green), and a GCPW for the transmission of high-frequency signals (purple). The connectors and the cables are labeled from $J1$ to $J10$ and a sketch of the pin arrangement at the DC connector and the cavity cutout is imprinted to the top layer. Additionally, four resistors labeled from $R1$ to $R4$ can be placed on the top layer, to electrically connect the top and bottom layer. (b) Expanded side view of the layer configuration. (c) Bottom layer with the tracks that transmit the signal from the DC connector to the cavity cutout.

The PCB was designed with the software package Altium Designer version 22.0.2 and later manufactured by the Vienna based company PIU-Printex GmbH. The final PCB design is depicted in Fig. 2.10. The high-frequency PCB is structured in four conducting copper layers which are separated by different insulating laminates. The top and the bottom layer are containing the signal tracks from the different connectors to the sample, while the middle layers provide a reference ground for the outer layers. The ground and the signal layers are $35\ \mu\text{m}$ thick and separated by the dielectric laminate Rogers3003 with a dielectric constant $\epsilon_r = 3$ and a thickness of $254\ \mu\text{m}$, while the two ground layers are separated by the $127\ \mu\text{m}$ thick dielectric laminate FR-4, with a dielectric constant $\epsilon_r = 4.8$. The PCB can be mounted and thermally coupled at the rods of the DRs sample holder via slotted vias. As these vias electrically connect the bottom and the top layer, four resistors can be added as indicated in Fig. 2.10, to short the top and bottom layer. The three main components of the PCB are the 24-pin non-magnetic DC connector (blue), the non-magnetic SMP connectors (red), the cavity cut out (green), and the high-frequency GCPW transmission line that connects the SMP connectors with the PCBs bonding pads.

The DC signal is routed from the pins to the bottom layer with vias, further directed to the cavity cut out with grounded coplanar wave guide transmission lines, and again connected to the PCBs bonding pads by vias. The SMP connectors are coupled to a $4\ \text{mm}$ long grounded coplanar waveguide, that transmits the signal from the SMP connector to a bonding pad. The GCPW allows a signal transmission from the $0.4\ \text{mm}$ wide pin of the SMP connectors to the bonding pads and was computationally analysed with the software package COMSOL Multiphysics to ensure low signal losses. The sample itself can be glued inside of the cavity cutout and connected to the bonding pads with a wire bonder. In future experiments, antenna structures will be patterned directly on the sample (see [4]). As the further design of these antennas still needs to be investigated, the PCBs where designed with two different high-frequency transmission lines. One version of the PCB contains a $50\ \Omega$ -matched GCPW and the other version provides the possibility to bond to high impedance antennas with a $50\ \Omega$ to $100\ \Omega$ tapered GCPW. The cavity cut out is needed to align the surface of the investigated samples as close to the PCBs top layer, and therefore the magnetic field center inside of the DR, as possible. The manufactured PCB is depicted in Fig. 2.11.

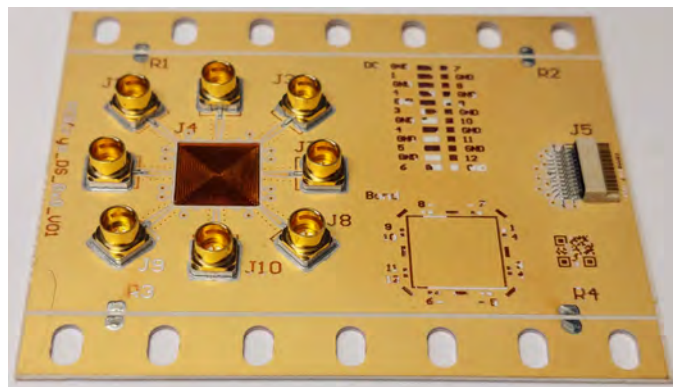


Figure 2.11.: High-frequency PCB following the design of Fig. 2.10 and fabricated by the company PIU-Printex GmbH. The PCB contains a cavity cutout, eight SMP connectors, and a 24-pin DC connector.

Wire Bonding

The high-frequency PCB was designed in a way, that all signal tracks that route either a DC or a high-frequency signal from the connector to the cavity cut out, end with a 100 μm bonding pad. These pads can be connected to an antenna pattern on the analysed sample with a thin metallic wire by a wire bonder. Multiple different bonding techniques are used in the field of microelectronics, but one of the most standard techniques is called ultrasonic bonding. Ultrasonic bonding is normally performed at room temperature (if heating is involved it is often referred to as thermo-sonic bonding) and uses aluminium or gold wires to interconnect the bonding pads. The weld at the bonding pad is formed by applying ultrasonic energy via a resonator in combination with the application of a clamping force. The majority of wire bonding is done with round wires. However, in the microwave regime, ribbon wires prove to be more suitable due to lower losses. Compared to round wires, ribbon wires have a lower impedance at high frequencies, which results in lower skin effect losses [46]. A second advantage of ribbon bonds in the GHz-regime is the smaller crosstalk. Crosstalk is the term for signals that are induced in an antenna by neighbouring signal transmitters, which may can be neglected at low-frequency ranges but can lead to problems when working with high frequencies [47].

2.3. Finite Element Frequency-Domain Simulation

The design of high-frequency transmission lines requires simulations to optimise the geometry and the used materials for the best possible signal transmission. The numerical simulations in this thesis were obtained with the software package COMSOL Multiphysics and the built-in RF-module. In general, two main approaches are used in COMSOL Multiphysics to simulate variations in time of physical quantities: the explicit time-domain study and the implicit time-domain study. In the RF-module, explicit time-domain studies are available over the Electromagnetic Waves Transient interface, which calculates the changes in the solution of the used equation-set for each time step. As this approach causes great computational costs for small time steps, the implicit time-domain study, namely the Electromagnetic Waves Frequency-Domain interface, often is more sufficient and therefore also is used in this thesis. The latter approach can be used if variations in time occur as sinusoidal signals and the problem proves to be time harmonic. Thus, a stationary problem with complex-valued solutions can be formulated, where the amplitude and the phase of the field are included in the complex values and the frequency is specified as a scalar model input. Typical frequency-domain simulations contain propagating wave problems, for example in waveguides and antennas. The Electromagnetic Waves Frequency-Domain interface solves Faradays law and Maxwell-Amperes law, combined in equation 2.3 for small mesh elements (finite elements), under the consideration of the chosen boundary conditions [48]:

$$\nabla \times \mu_r^{-1}(\nabla \times \mathbf{E}) - k_0^2 \left(\epsilon_r - \frac{j\sigma}{\omega\epsilon_0} \right) \mathbf{E} = 0. \quad (2.3)$$

Here, μ_r represents the relative permeability and ϵ_r the relative permittivity of the propagation medium. \mathbf{E} is the electric field, k_0 is the wave vector, j is the current density, σ is the electric conductivity of the propagation medium, and ω is the angular frequency. The excitation (and detection) of an electromagnetic wave can be simulated by the lumped port boundary condition, which can be described as a voltage source between two electrodes. A lumped

port has to be applied between two metallic surfaces and should only confine a distance much smaller than the wavelength [48]. The lumped port calculates the impedance and the S -parameters as defined in Sec.[2.2] and therefore is a useful tool in the analysis of signal transmissions.

3. Experimental Realisation and Characterisation of a Dilution Refrigerator System

This chapter discusses the experimental realisation of a dilution refrigerator system combined with a 40 GHz-rated VNA system in a cryogenic PSWS measurement setup. Further, the DR is characterised with regard to its cool down behaviour, different applied heat loads at the sample, the losses of the internal transmission lines, and the temperature change during the operation of the magnet.

3.1. Realisation of the Dilution Refrigerator Measurement Setup

The installation of a Bluefors LD250 cryogen-free dilution refrigerator system and its implementation in a functioning measurement setup was within the framework of this thesis. Fig. 3.1 (a) shows a photo of the measurement setup that was developed within my master thesis. An Anritsu VectorStar VNA system with KBL-2M-LOW+ high-frequency cables (green box) allows the monitoring and application of microwave signals up to 40 GHz in a power range of -30 dBm to 20 dBm. The VNA itself is connected to the internal transmission lines of the DR by KBL-2M-LOW+ high-frequency cables, which are rated for signals up to 40 GHz. The high-frequency cables are connected to an adapter plate with 2.92 mm-2.92 mm connectors and afterwards routed and attached to the top plate of the DR (purple box). The intermediate adapter plate simplifies the switching between different ports, as they now do not have to be changed on the top plate of the DR. At the top plate, the signal enters the vacuum can of the DR (yellow box) and is transmitted to the sample holder. The SMP ports of the sample holder can be connected to a PCB via copper cables. The PCB itself can be mounted on rods at the sample holder (see Fig. 3.1 (e)) and is inserted into the DR with the help of the bottom loading system (red box). The external magnetic field is created in the coils of the superconducting magnet, which are located around the sample holder inside of the vacuum can (see Fig 3.1 (b)). The magnet is operated with an external power supply (blue box). This laboratory setup allows to characterise the DR, test the high-frequency PCB and permits first spin-wave excitations in the millikelvin temperature regime. Fig. 3.1 (b) depicts the experimental setup for the experiments performed within this thesis. The VNA system is indicated on top of the adapter plate, with the cables and transmission lines (blue) connecting it to the sample holder inside of the cryostat. Fig. 3.1 (c)-(e) show the shorted sample insert for the determination of the losses in the internal transmission lines (c), the mounted samples for the proof of principle of the high-frequency PCB (d), and a microantenna-PCB with a $70\text{ mm} \times 2\text{ mm} \times 5.65\text{ }\mu\text{m}$ YIG strip on a $500\text{ }\mu\text{m}$ thick GGG substrate for the millikelvin PSWS measurements (e).

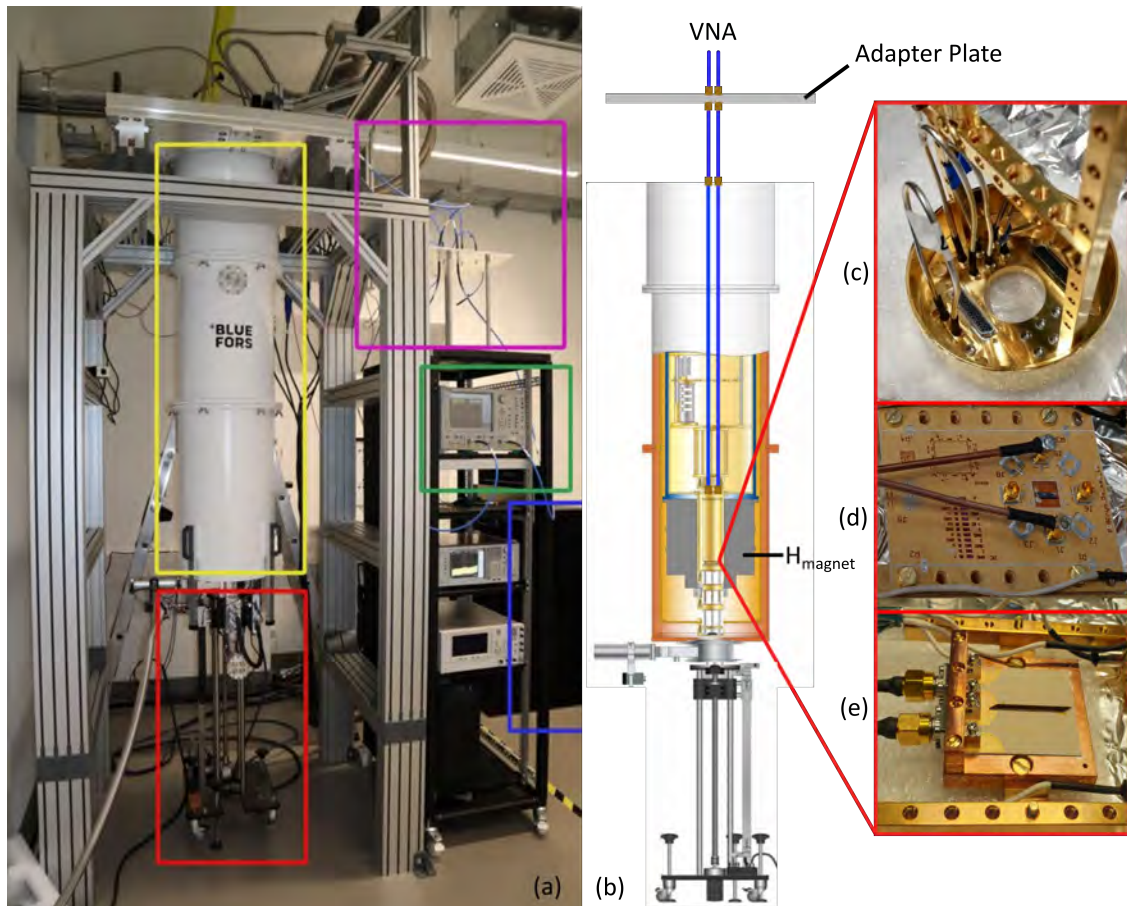


Figure 3.1.: (a) Laboratory setup with the cryostat (yellow box), the bottom loading system (red box), the power supply of the superconducting magnet (blue box), the VNA system (green box), and the KBL-2M-LOW+ high-frequency cable connection with an adapter plate (purple box). (b) Schematic of the setup for the experiments performed in this thesis, including the VNA on the top, the vacuum can of the dilution refrigerator (following [35]), the high-frequency cables and transmission lines of the cryostat (simplified with two blue lines), and the sample loader. (c) Patch cables that short the ports at the sample holder for the determination of the signal losses in the transmission lines of the cryostat. (d) Proof of principle of the high-frequency PCB with a YIG strip on GGG. (e) Millikelvin PSWS measurement with a microantenna-PCB and a YIG strip on GGG.

To determine the losses in the internal transmission lines of the cryostat, the different ports at the sample holder were directly interconnected with patch cables (see Fig. 3.1 (c)). The recorded data were corrected by subtraction of the transmission losses of the KBL-2M-LOW+ cables and the used patch cables.

The proof of principle of the high-frequency PCB was performed with a $70 \text{ mm} \times 2 \text{ mm} \times 5.65 \mu\text{m}$ YIG strip on a $500 \mu\text{m}$ thick GGG substrate. The YIG film is placed perpendicular to the SMP connectors of the PCB, which are connected to the transmission lines of the cryostat via copper cables (see Fig. 3.1 (d)). The signal of the SMP connector is routed to the sample

by a gold wire, which represents an antenna that can excite a spin wave. The spin wave that is detected with the VNA system, proves that a signal is transmitted through the high-frequency transmission lines and connectors of the manufactured PCB. Propagating spin-wave spectroscopy in the MSSW configuration was performed in a $70\text{ mm} \times 2\text{ mm} \times 5.65\text{ }\mu\text{m}$ YIG strip on a $500\text{ }\mu\text{m}$ thick GGG substrate at millikelvin base temperatures. The spin waves were excited by microstrip antennas on a microantenna-PCB. The PCB, together with the sample, was mounted on an oxygen-free copper holder, which can be thermally coupled to the sample rods of the DRs sample holder. Copper cables allow to connect the sample holder and the PCB (see Fig. 3.1 (e)). The YIG strip was placed on top of the microstrip antennas and glued to the microantenna-PCB with GE-varnish.

3.2. Calibration of the Dilution Refrigerator System

3.2.1. Cool Down Curve

To ensure ideal operation of the installed Bluefors LD250 cryogen-free dilution refrigerator system, the cool down curves of the 50 K-shield, 4 K-shield, the superconducting magnet, the still-flange, and the mixing chamber were recorded from room temperature to a steady base temperature. The temperature laps was recorded by the resistance temperature detectors (RTDs), placed at the introduced thermal stages (see Fig. 3.2). This temperature curve can be compared to reference data, which are provided by the manufacturer Bluefors (see [32]). After the vacuum can was pumped to a pressure level of 6.5×10^{-3} mbar, the pulse tube cooling was started to activate the first cool down cycle. The 50 K-shield stabilises at a temperature of 45 mK, the 4 K-shield at 3.8 K, the magnet at 6.4 K, and the still-flange at 5.6 K after 50 h of pulse tube operation. Due to the high thermal mass, the magnet temperature decreases slower than the other thermal stages.

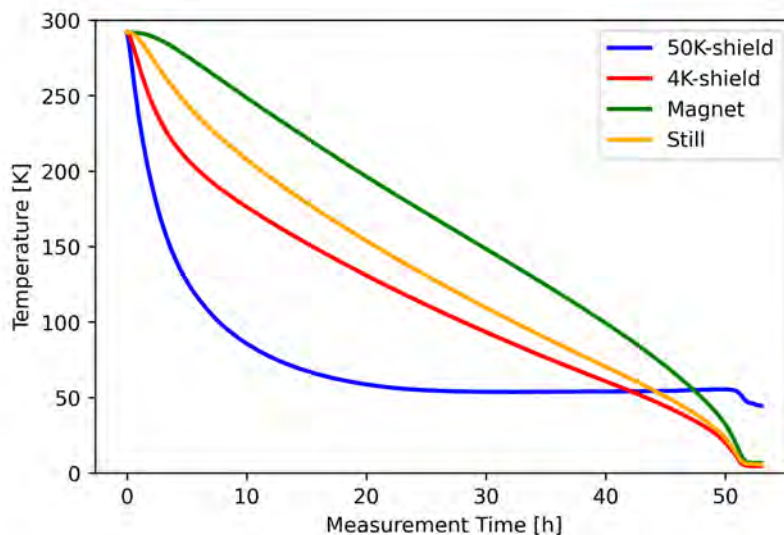


Figure 3.2.: Cool down curve measured at the 50 K-shield (blue), the 4 K-shield (red), the magnet (green), and the still-flange (orange) during the PTC operation.

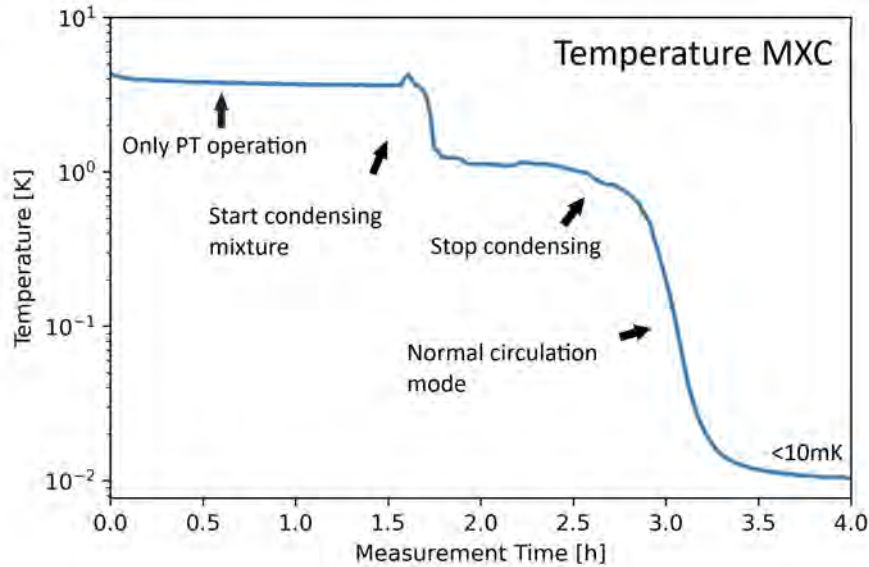


Figure 3.3.: Recorded cool down curve of the mixing chamber during the operation of the Dilution Unit. After a constant temperature plateau during the pulse tube cooling, the temperature decreases with the condensing of the mixture. When the condensing is stopped, the temperature stabilises and drops again once the normal circulation mode is started, until a final base temperature below 10 mK is obtained.

Once the temperature during the first cooling cycle reaches a plateau, the operation of the DU can be initiated, to start cooling down to millikelvin base temperatures (see sec.[2.1]). Fig. 3.3 displays the temperature laps of the mixing chamber during the operation of the dilution unit. Once the dilution cycle is started, the temperature starts to decrease abruptly during the condensing of the mixture and stabilises at 1 K, until the condensing is stopped. During the normal circulation mode, the temperature decreases further until a final base temperature below 10 mK is obtained.

3.2.2. Heat Load Test

The Bluefors LD-Series cryogen-free dilution refrigerator system enables the user to control and change the temperature at certain stages, namely the distiller, the mixing chamber, and the probe. The heaters are controlled by the applied current or input power and can increase the base temperature at the dedicated stages via Joule heating. Typical input powers of the still heater are in the mW-range, to reach the desired temperature regime of 0.7 K-0.8 K (see [31]) for the optimal cooling power and circulation. The probe heater is operated in the μ W-range. Generally, the still heater is on during circulation, to ensure optimal operation of the DU. In the case of the examined DR, the optimal input power at the still heater was found to be 9 mW. The heater at the sample is only operated if temperatures above the base temperature are required. However, it proves to be very useful to perform a heat load test, to characterise the behaviour of the heater and provide an estimate of the current that needs to be applied to reach specific temperatures. As shown in equation 3.1 and 3.2 (principle

thermodynamics and Joules law), the temperature difference should be linearly dependent on the current that is applied at the heater. The temperature T proves to be a function of the current I , the voltage U , the time span Δt for which the current is applied, and the heat capacity C . In the case of the DR the temperature will stabilise at a certain level, as the cooling and the heating reach an equilibrium at the base temperature:

$$\Delta Q = C \cdot \Delta T \quad \Delta Q = U \cdot I \cdot \Delta t, \quad (3.1)$$

$$\Delta T = \frac{U \cdot \Delta t}{C} \cdot I. \quad (3.2)$$

Fig. 3.4 depicts the temperature curve of the examined dilution refrigerator during the application of different heat loads at the probe heater, indicated by the heater currents. The temperature of the probe and the mixing chamber was recorded for different applied current values up to 3.54 mA. The measurement data accord with the expected linear behaviour of equation 3.2. The used temperature sensors are characterised with an uncertainty of ± 4 mK for temperatures up to 50 mK and ± 16 mK for temperatures up to 1.5 K. The probe heater is able to increase the temperature of the corresponding thermal stages to steady temperature levels, with the experimentally determined correlation

$$T_p = (218.217 \cdot I + 15.106) \text{mK} \quad T_{\text{MXC}} = (57.567 \cdot I + 1.287) \text{mK} \quad (3.3)$$

between the temperature rise ΔT and the applied current I . It should be mentioned, that the linear fit does deviate from the measured temperatures at small currents between $0 \mu\text{A}$ and $25 \mu\text{A}$, with a difference of 4.15 mK for T_p and 7.73 mK for T_{MXC} at zero current.

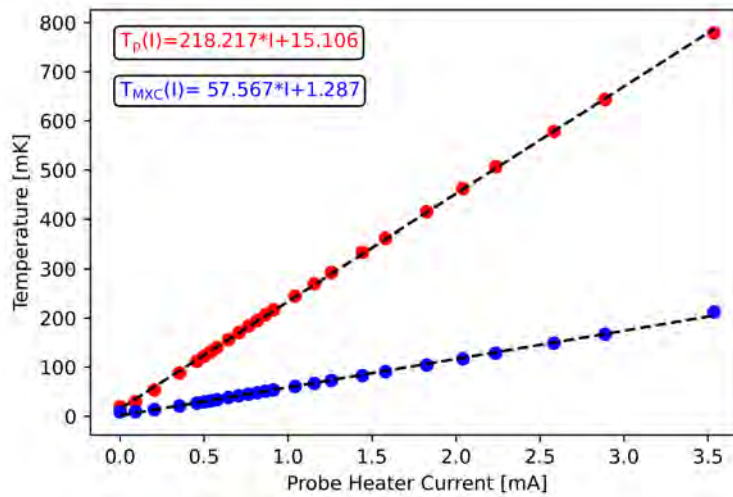


Figure 3.4.: Measurement of the temperature increase at the probe (red) and the mixing chamber (blue) for different power inputs at the probe heater. The temperature proves to be a linear function of the applied current at the heater. The used temperature sensors are characterised with an uncertainty of ± 4 mK for temperatures up to 50 mK and ± 16 mK for temperatures up to 1.5 K.

3.2.3. Reference Measurement of Cable Transmission

For future measurements and the ones presented in this thesis, it is required to characterise the signal losses in the transmission lines of the DR between the top plate and the coaxial SMP ports at the sample insert (see Fig. 3.1 (b)). These reference measurements allow to estimate the signal losses that can be traced back to the experimental setup. Additional losses that arise from external cables can be subtracted from the signal with the calibration function of the VNA system itself. The different port configurations for the transmission measurement and the corresponding attenuation losses are summarised in table 3.1. The cryostat is equipped with four regular conducting lines (ports 1 to 4) and four superconducting lines (ports 5 to 8), which can transmit signals from an external source to the sample holder. The transmission of port 3 and 4 was not determined, as the SNR does not allow to detect signals in the used power range, due to the high attenuation losses of 92 dB.

To obtain the DRs transmission line losses, the KBL-2M-LOW+ cables need to be included in the calibration of the VNA and the signal loss of the patch cables need to be subtracted from the data. Therefore, the S_{12} parameters of the patch cables were determined separately with the VNA system. Fig. 3.5 displays the recorded S_{12} spectra of the internal cryostat transmission lines between room temperature and millikelvin base temperatures for frequencies up to 40 GHz. As proof of principle, the signal transmission was recorded for the input powers -10 dBm and 0 dBm.

We observe that the transmission decreases with increasing frequencies at both input power levels, with a rising noise level at frequencies above 10 GHz and a smaller SNR for lower input powers. The regular conducting lines at port 1 and 2 show higher losses than the superconducting lines below the critical temperature of the superconductors. If the 30 dB losses related to the attenuators are taken into account, the regular conducting lines have losses below 1 dB at a frequency of 1 GHz, but show a continuously lower transmission for rising frequencies, with losses of 40 dB at a frequency of 40 GHz. For the superconducting lines the losses indeed increase with frequency, but the overall losses are smaller compared to the normal conducting lines, as expected. Port 5 and 6 show a signal loss of 11 dB and port 7 and 8 display 27 dB losses at frequencies near 40 GHz. Therefore, the superconducting transmission lines behave consistent, if the attenuator losses of table 3.1 are taken into account. Both superconducting lines show no dependence on the signal power in this frequency spectrum and reveal no differences at the measured temperatures of 4 K and 18 mK.

Ports	Type	Attenuator losses [dB]
1 & 2	regular	15 each
5 & 6	superconducting	0
7 & 8	superconducting	7 each

Table 3.1.: Summary of the port configurations during the transmission reference measurement and the signal losses introduced by the integrated attenuators.

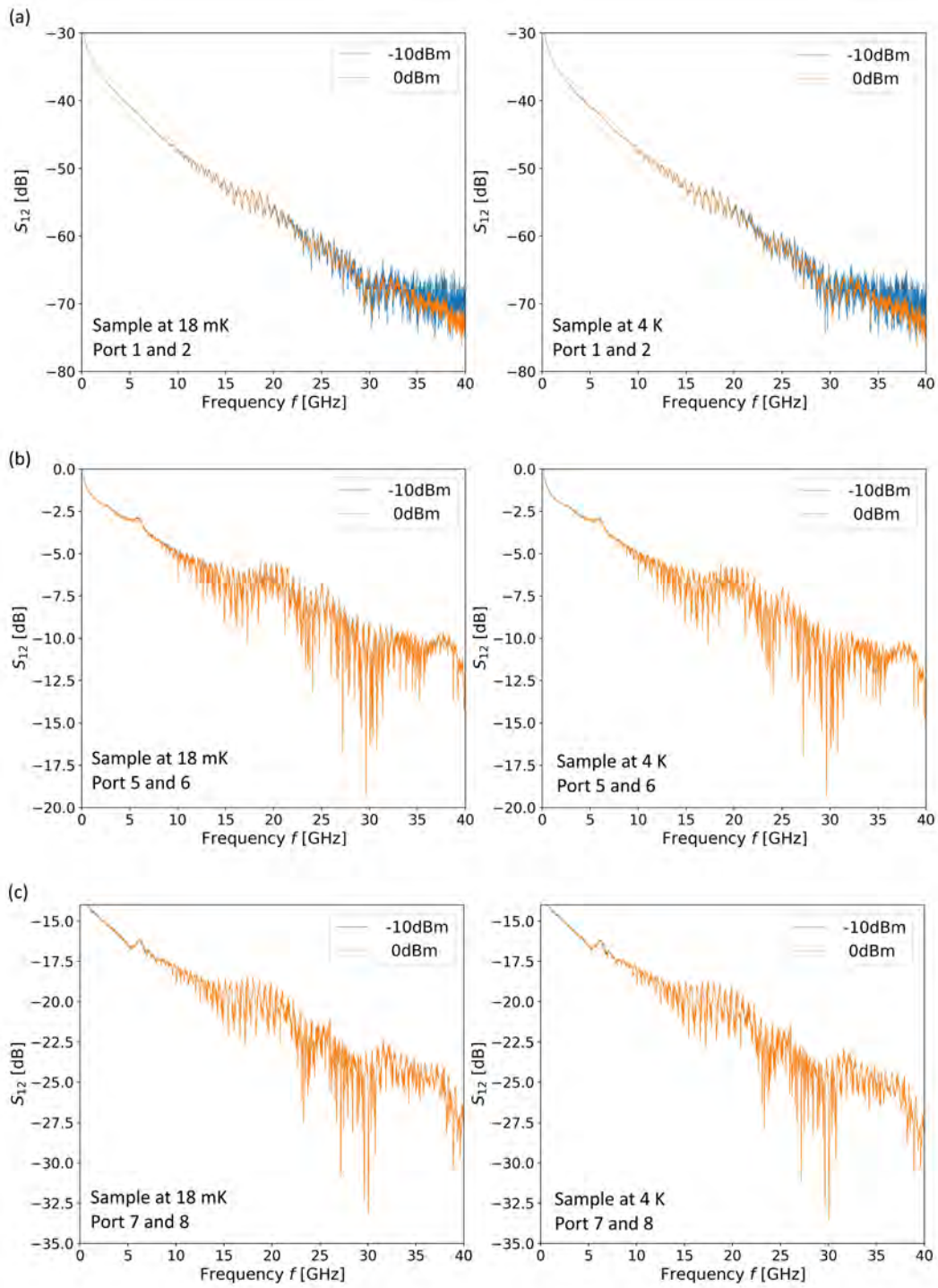


Figure 3.5.: S_{12} -parameters for (a) port 1 and 2 (regular conducting), (b) port 5 and 6 (superconducting) and (c) port 7 and 8 (superconducting). The S -parameters were recorded at temperatures of 18 mK and 4 K for the input powers -10 dBm and 0 dBm. The attenuation losses of 30 dB for ports 1 and 2 and 11 dB for port 7 and 8 need to be considered in the recorded transmission losses.

3.2.4. Cooling Behaviour of the Vector Magnet

To test the performance of the magnet and prepare a reference for future measurements, the temperature curve of the 4K-flange was recorded for different field magnitudes and field directions. The temperature of the 4K-shield was chosen as reference, as it is thermally coupled to the magnet and responds faster to temperature changes, because of the lack of thermal mass. Fig. 3.6 shows the temperature evolution during the magnet operation. During the operation of the magnet coils in z -direction with a field magnitude of 9 T, a steep temperature rise of 1 K can be observed. This increase in temperature is caused by the magnet ramping to the field of 9 T. The ramp-rate to reach the field was 0.1 T/min. After the desired field magnitude is obtained, the temperature decreases but stabilises again, as the applied current from the power supply is steady at this point. Once the temperature has stabilised, the heater of the PCS is turned off, which leads to a rapid temperature decrease. It is followed by another temperature decrease, once the magnet is in persistent mode. Afterwards, the temperature stabilises again, as no additional current is applied to the magnet coils (see Sec.[2.1]). To ramp the magnet to zero magnetic field, the persistent switch needs to be turned on again and therefore current is applied to the heater, which leads to a temperature increase. Once the persistent switch is turned back on, the magnet exits the persistent mode and can start to ramp down. The ramping leads to a temperature increase and is followed by a steep temperature decrease. The temperature stabilises again and decreases to the pre-operation level, once the persistent switch is turned off.

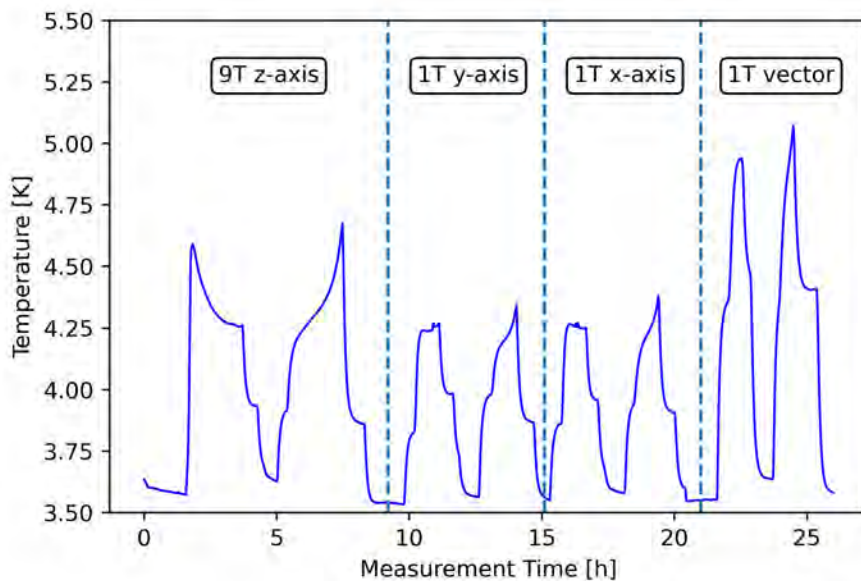


Figure 3.6.: Measurement of the temperature at the 4K-stage during the operation of the magnet in the z -, y -, x - and combined vector-mode. Further explanation can be found in text.

	z	y	x	xyz
Target Field [T]	9	1	1	1
Ramp Rate [T/min]	0.1	0.025	0.025	0.025

Table 3.2.: Parameters for the performance test of the superconducting vector magnet. Further information is provided in the text.

An analogue procedure was performed for the y - and the x -coil operation, with a ramp rate of 0.025 T/min up to a field magnitude of 1 T. In the vector configuration, the operation cycle was performed with a ramp rate of 0.025 T/min to an individual field of 0.577 T in the x -, y - and z -coils, resulting in a magnetic field with directions in x , y and z and a resulting field magnitude of 1 T. The ramp rates and the target field for the different configurations of the magnet are summarised in table 3.2.

4. Analysis of a High-Frequency PCB for Quantum Magnonics

Within this thesis, a multilayer high-frequency PCB was designed as part of a measurement platform for future experiments in the field of quantum magnonics, with the ability to host various samples and bond to transmission lines with signals in the DC and high-frequency spectrum. Important transmission lines of the PCB were computationally analysed with finite element frequency domain studies. Further, an experimental proof of concept of the high-frequency PCB is presented and prospects of the PCB are discussed.

4.1. Computational Analysis of High-Frequency Transmission Lines

The designed high-frequency PCB is equipped with multiple connectors and different transmission lines, that route the applied signals to the bonding pads (see Fig. 2.10). Most of the transmission lines are hosting DC signals on the bottom layer of the PCB and are designed as short and direct as possible, to minimise losses (see [49]). The transmission lines that route the high-frequency signals from the SMP connectors to the bonding pads, represent more complex structures and have therefore been computationally analysed with the COMSOL Multiphysics software package (see Fig. 4.2).

The high-frequency PCB was designed in two versions for the first manufacturing run: one with a straight GCPW and one with a tapered GCPW from the SMP connectors to the bonding pads. The GCPW should be impedance matched with the SMP connectors characteristic impedance of $50\ \Omega$ at the soldered pin, to avoid signal reflections. Therefore, the straight GCPW was designed for a characteristic impedance of $50\ \Omega$, while the tapered GCPW matches the $50\ \Omega$ at the SMP connector, but exhibits a higher impedance of $100\ \Omega$ at the end of the taper. Both versions of the PCB allow to bond to antennas that are patterned into investigated samples. As the best antenna design for future PSWS measurements still needs to be investigated, the higher impedance of the tapered version provides more flexibility, due to the possibility to work with high impedance antennas. The dimensions of the GCPW were determined with respect to the desired characteristic impedance values, the pin size of the SMP connector and the material parameters of the used dielectric laminate. The pin of the SMP connector is $0.4\ \text{mm}$ wide and needs to be soldered on the top layer of the PCB. Therefore, the signal track of the GCPW at this end has to be at least $0.6\ \text{mm}$ wide, to provide enough space for soldering. Rogers3003, with a relative permittivity $\epsilon_r = 3$, was chosen as the dielectric laminate for the high-frequency PCB, due to its isotropic coefficient of thermal expansion and the small thermal coefficient of ϵ_r (see [50]). For the high-frequency signals up to $40\ \text{GHz}$, which will be transmitted through the GCPW, fencing vias need to be implemented along the transmission line, to break possible higher order modes in the ground strips [51]. A sketch of the GCPW geometry for both versions is depicted in Fig. 4.1.

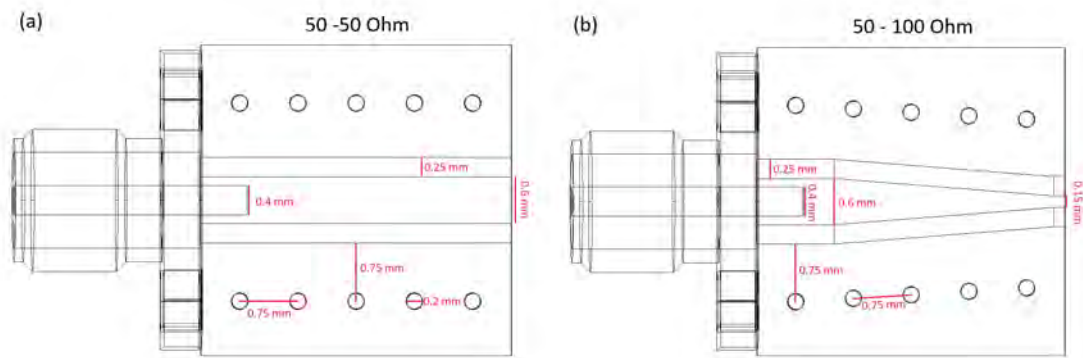


Figure 4.1.: Geometry and dimensions of the GCPW that transmits high-frequency signals from the SMP connector to the bonding pad. (a) Straight GCPW with a characteristic impedance of $50\ \Omega$. (b) Tapered GCPW with an impedance of $50\ \Omega$ at the pin of the SMP connector and an impedance of $100\ \Omega$ at the bonding pad.

The excitation and propagation of an electromagnetic signal in the GCPW was simulated with a 3D model in the RF module of COMSOL Multiphysics. The model consists of a 4×4 mm block with a thickness of $254\ \mu\text{m}$ and the material parameters of the laminate Rogers3003 (see Fig. 4.2). This block corresponds to the dimensions and intrinsic parameters of the real transmission line on the PCB. The signal track, the ground strips and the bottom side of the block were assigned with the perfect electrical conductor (PEC) boundary condition, to represent the metallic top and ground layers of the PCB. The SMP connector was added to the model with an in-built SMP geometry of COMSOL and the respective dimensions and material parameters of the real connector. The lumped port boundary condition was used to excite an electromagnetic wave at the pin of the SMP connector and to detect the signal at the bonding pad. A coaxial lumped port boundary condition was used at the SMP connector and a rectangular lumped port boundary condition in an air bridge configuration (see [52]) was applied at the bonding pad. The shielding vias were assigned with the PEC boundary condition to connect the ground strips and the bottom ground layer. The vias are situated in a distance of $0.75\ \text{mm}$ to the signal track and between the vias. The spacing was varied over several simulation runs and chosen in the configuration with the smallest transmission losses. The whole geometry is surrounded by an air volume that was assigned the scattering boundary condition, to minimise back reflection. The 3D model was meshed with the physics controlled mesh option of COMSOL. A finite element frequency-domain study for the frequency range of $1\ \text{GHz}$ to $40\ \text{GHz}$ was performed with a frequency step of $1\ \text{GHz}$, to calculate the electric field norm.

Fig. 4.2 (a) and (b) depict the electric field magnitude and the field components, indicated by red arrows, for the straight and tapered version of the GCPW. The electric field lines in a GCPW configuration should follow the distribution of Fig. 2.8, which is acknowledged by the results of Fig 4.2. A frequency of $40\ \text{GHz}$ corresponds to a wavelength of $7.5\ \text{mm}$ and therefore

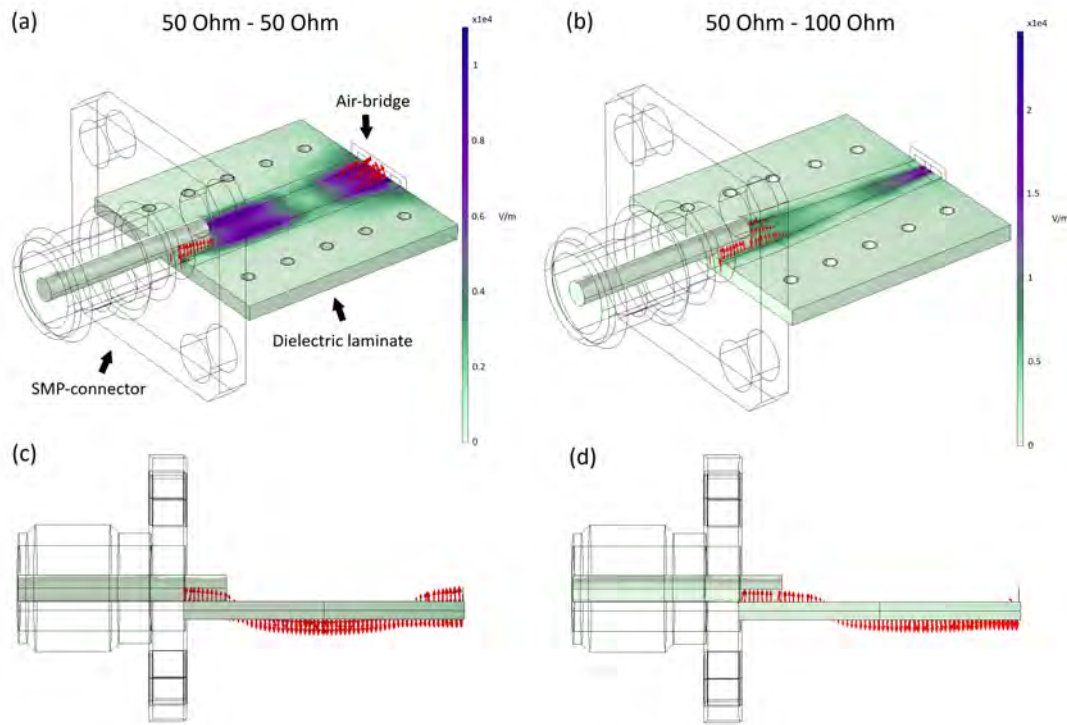


Figure 4.2.: Norm of the electric field components, indicated by the colour legend, and the electric field components illustrated by red arrows. (a) and (c) Simulation results for the $50\ \Omega$ -matched version of the high-frequency transmission lines. The shown electric field was calculated for an excitation signal with a frequency of 40 GHz. (b) and (d) Simulation results for the $100\ \Omega$ high impedance version of the high-frequency transmission lines.

approximately half a wavelength fits into the 4×4 mm block that represents the GCPW. Thus, one amplitude of the sinusoidal signal can be suited in the waveguide (see Fig. 4.2 (c) and (d)). Fig. 4.2 (a) and (b) demonstrate that the signal is confined in the center track of the GCPW in both versions. The electromagnetic wave travels from the pin of the SMP connector directly to the bonding pad. The frequency-domain study also calculated the S -parameters for the chosen input frequencies, with the S_{21} - and the S_{11} -parameters displayed in Fig. 4.3 (a) for the straight version of the GCPW and in Fig. 4.3 (b) for the tapered version of the GCPW. Considering the broad frequency range, the signal transmission losses are steady at -1 dB, with a decrease of the transmission for frequencies above 30 GHz at both designs of the GCPW. The S_{11} -parameters of Fig. 4.3 constantly increase with frequency, indicating an impedance mismatch at high frequencies. The reflection spectrum of Fig. 4.3 (b) depicts a minimum at 31 GHz, indicating a standing wave formation within the waveguide structure [53]. After the minimum, the reflection curve increases again. The GCPW will be bonded to an antenna and the reflection spectrum therefore can change like it is the case in long transmission lines [54]. Nevertheless, the transmission spectra prove to be constant over the simulated frequency range, with small losses above 30 GHz, and therefore justify the modelled GCPW.

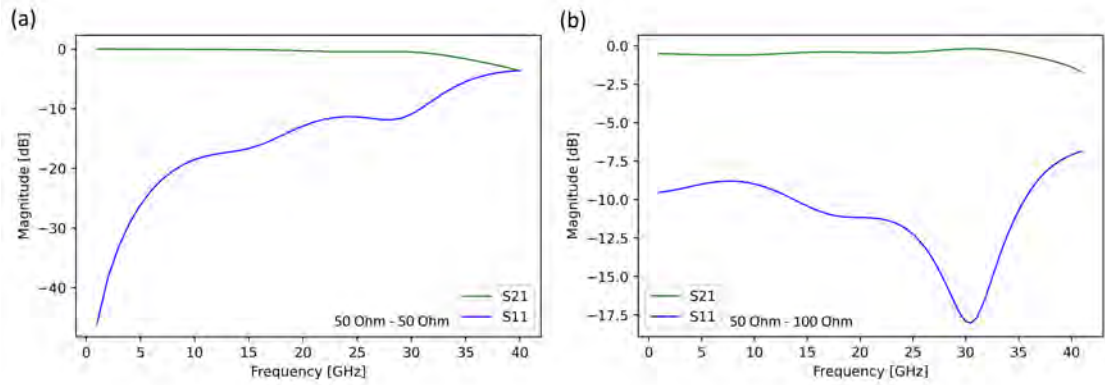


Figure 4.3.: Simulated S -parameters for (a) the $50\ \Omega$ - $50\ \Omega$ straight version of the GCPW and (b) the $50\ \Omega$ - $100\ \Omega$ tapered version of the GCPW. The green line represents the S_{21} -parameters and therefore the signal transmission. The blue line depicts the reflection spectrum with the S_{11} parameter. The S -parameters were obtained in a finite element frequency-domain study with a stepsize of 1 GHz and are displayed continuously for a better illustration of the transmission and reflection spectra.

4.2. Proof of Concept of the High-Frequency PCB at Millikelvin Temperatures

After the computational analysis of the high-frequency transmission lines, the technical functionality of the manufactured high-frequency PCB was experimentally tested. Therefore, a spin wave was excited and detected in a 2 mm wide and $5.65\ \mu\text{m}$ thick YIG strip on a $500\ \mu\text{m}$ thick GGG substrate, which was glued in the cavity cutout of the PCB with GE-varnish and silver paint. Two gold wire wedge bonds are used as antennas, that host the high-frequency signal from the PCB and excite or detect spin waves in the sample (see Sec.[1.2]). This experiment is a non perfect PSWS measurement, due to the inefficient antennas, but enables to proof the working principle of the high-frequency PCB. A simplified schematic of the experiment together with the high-frequency PCB, mounted on the sample rods of the dilution refrigerator, is depicted in Fig. 4.4 (a). For this experiment, a 40 GHz-rated Anritsu VectorStar VNA system was connected to the dilution refrigerator over ports 5 and 6 and two KBL-2M-LOW+ high-frequency cables. The transmission lines of the DR were connected to the high-frequency PCB via the sample holder and two copper cables (see Fig. 4.4 (a)). The spin wave was excited with an input power of $-5\ \text{dBm}$ at the VNA and the S -parameters were recorded over 200 loops per point. The measurement was performed in the MSSW configuration with external bias fields of 150 mT, 160 mT, and 175 mT at a temperature of 105 mK. Similar to the results of chapter [5] the results were corrected to the non-magnetic background and smoothed with the *scikit - rf* package included in python (see [55]).

Fig. 4.4 (b) proofs the excitation and detection of a propagating surface spin wave as a prominent peak in the S_{12} spectrum (see Sec.[1.2]). The dispersion curve can be shifted to higher spin-wave frequencies, if the applied magnetic field is increased and therefore allows to distinguish the peaks in the S_{12} spectrum from other features. The detected spin waves represent a proof of the functionality of the manufactured high-frequency PCB and validate

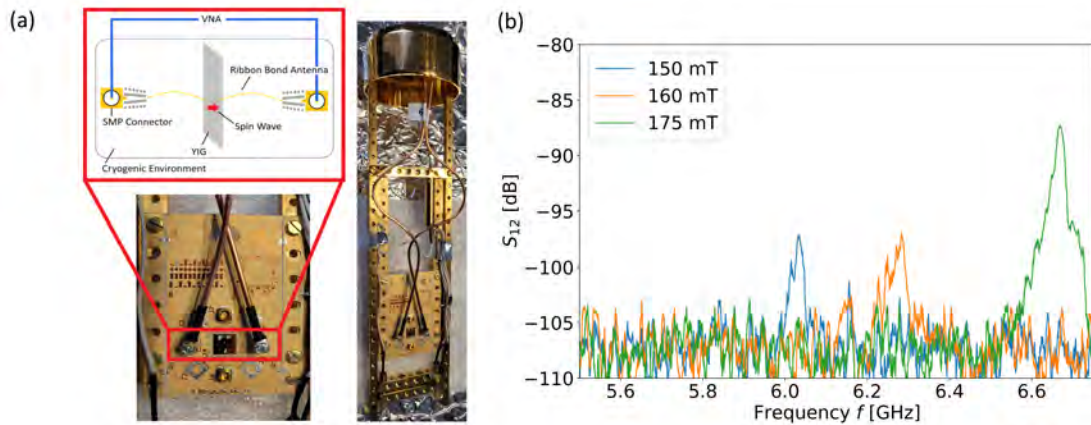


Figure 4.4.: (a) Simplified schematic for the experimental proof of principle of the designed high-frequency PCB. A signal with an input power of -5 dBm at the VNA excites a spin wave (indicated by red arrow) at a bonded gold wire antenna. The spin wave is detected by a second antenna at the opposing edge of the sample. The components placed in the grey box are situated inside of the dilution refrigerator. The high-frequency PCB is mounted on the sample rods of the dilution refrigerator and connected to the transmission lines with copper cables. (b) Recorded S -parameters of the excited spin waves in a 2 mm wide and 5.65 μm thick YIG strip on a 500 μm thick GGG substrate with the designed high-frequency PCB at a temperature of 105 mK. MSSW were recorded at magnetic bias fields of 150 mT, 160 mT, and 175 mT.

the results of the computational analysis.

4.3. Prospects of the High-Frequency PCB

With the design, the computational analysis, and the experimental proof of concept, a major part of this thesis was dedicated to the development of a high-frequency PCB which allows propagating spin-wave spectroscopy in a broad microwave frequency spectrum from a few MHz up to 40 GHz. Additionally, DC signals can be applied to samples on the PCB, which opens the way for the modification of the dispersion curve of spin waves by a local change of the magnetic field (see Sec.[1.3]). Further experiments in the Nanomagnetism and Magnonics research group will be performed to utilise the local tuning of the magnetic field in the development of magnon phase shifters, delay lines, and attenuators.

The current PCB design takes into account, that antenna structures will be directly patterned on future samples by electron-beam lithography. To this point, it is still unclear if antennas with high impedance will allow more efficient spin-wave excitation or if a $50\ \Omega$ -matched circuit will prove to be more sufficient. Therefore, this question leaves room for further research in the design of high-frequency antennas and their application in PSWS measurements. To guarantee flexibility for future experiments, I designed a $50\ \Omega$ impedance matched version and a $100\ \Omega$ high impedance version with respect to the high-frequency transmission lines of the

PCB, as presented in the preceding sections. The $50\ \Omega$ -version is still in the manufacturing process and should arrive in the near future, while the $100\ \Omega$ -version was already fabricated. The non-optimal ribbon bond antennas allowed to proof the functionality of the PCB, but do not allow further experimental characterisation of the transmission losses. For this purpose, coplanar waveguide samples were fabricated in the clean room facilities of the Central European Institute for Technology (CEITEC), located in the city of Brno in the Czech Republic. These samples will allow to determine signal losses, that arise within the transmission lines and connectors of the designed PCB. Also, the fabrication of the CPW samples lead to valuable information for the nanofabrication of future antenna structures.

The CPW samples consist of a signal track and two ground lines of $10\ \text{nm}$ thick titanium and $60\ \text{nm}$ thick gold, deposited on a $6\times 6\ \text{mm}$ rectangular silicon wafer. Different samples were fabricated for the $50\ \Omega$ -matched version and the $100\ \Omega$ high impedance version of the PCB. To estimate the impedance and transmission losses of the fabricated CPW's, the sample patterns were computationally analysed with a finite element frequency-domain study in the COMSOL Multiphysics software package. Before the simulation, the optimal dimensions of the track width and the spacing to the ground lines were determined with an analytical online calculator tool (see [44]). These calculations considered the given thickness and relative permittivity ϵ_r of the used Si-wafer. As the sample structure is restricted by a reasonable patterning time of the e-beam lithography and the intrinsic material parameters of Si, it was not feasible to fabricate samples with higher impedance values than $Z_0 = 82\ \Omega$. This impedance mismatch between the sample and the bonding pad of the $100\ \Omega$ GCPW of the high-frequency PCB needs to be considered in future experiments.

A 3D model was generated and studied in the RF-module of COMSOL Multiphysics, to simulate the excitation and propagation of an electromagnetic signal in the designed CPW samples. The model consists of a $6\times 6\ \text{mm}$ substrate block, with the assigned material parameters of pure Si from the COMSOL material library (relative permittivity $\epsilon_r = 11.7$). On top of the substrate block, a 2D version of the analytically estimated CPW dimensions was imprinted with a work plane. The whole structure is covered by a sphere that represents the surrounding air volume. This sphere is assigned the scattering boundary condition, to suppress back reflection. The track and the two ground lines on top of the Si-block have been assigned the perfect electrical conductor (PEC) boundary condition, that prevents the electric field components normal to this plane to penetrate into the structure. Therefore, a two dimensional structure is sufficient to represent the Ti/Au-layer of the track and ground lines. The Lumped Port boundary condition was used to excite an electromagnetic signal at one end of the CPW and detect it at the other end of the structure. The multi-element-uniform type lumped port was used at two rectangular elements between the ground line and the track in each case. The

Parameters	$50\ \Omega$	$100\ \Omega$
Track Width [mm]	0.15	0.1
Metal Spacing [mm]	0.1	0.7
Trace Length [mm]	5	5
Characteristic Impedance [Ω]	50.51	81.77

Table 4.1.: Pre-calculated dimensions and impedance values of the fabricated samples. The data were estimated with an analytical online calculator tool (see [44]).

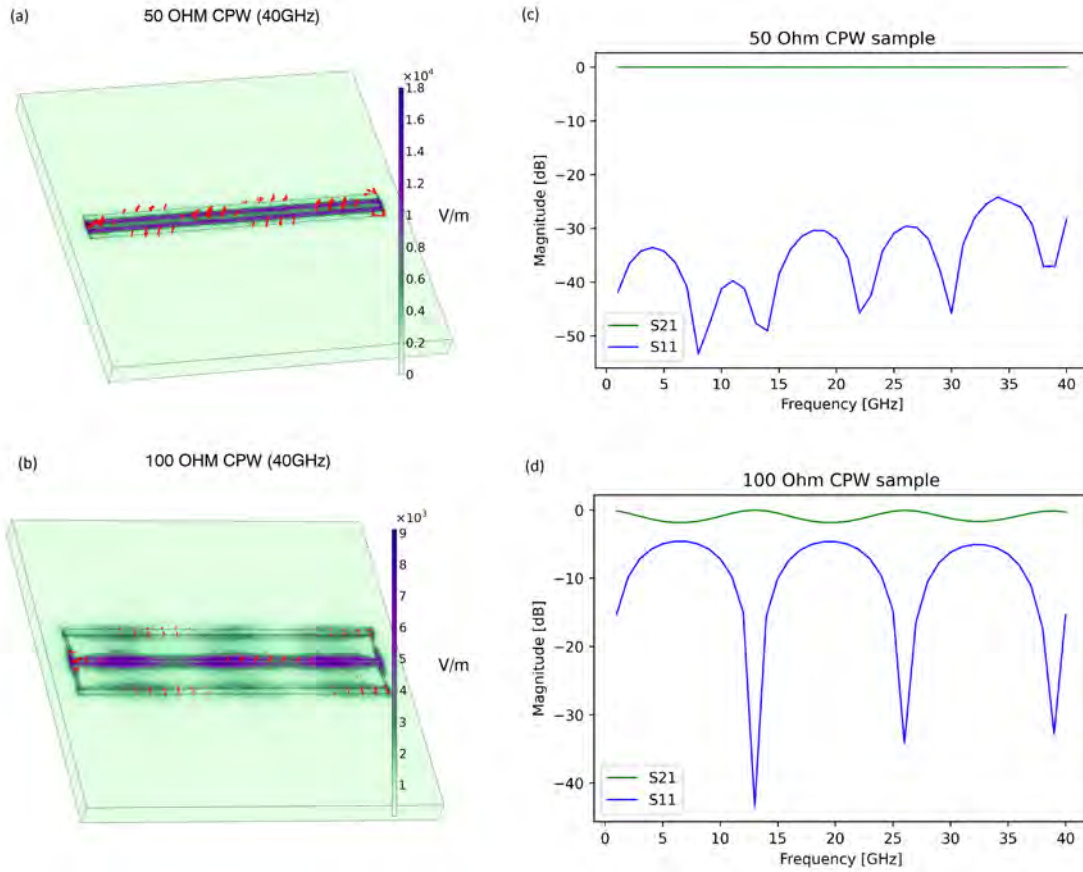


Figure 4.5.: (a)-(b) Norm of the electric field components indicated by the colour legend and electric field components indicated by red arrows for a $50\ \Omega$ and a $100\ \Omega$ Ti/Au-CPW on a Si-substrate. The electric field was calculated for a frequency of 40 GHz. (c)-(d) Simulated S -parameters of the fabricated CPW samples for a frequency spectrum of 1 GHz to 40 GHz with a step-size of 1 GHz.

whole structure was meshed with the physics controlled mesh option of COMSOL. By performing a frequency-domain study in the range of 1 GHz to 40 GHz, the electric field norm and the electric field components for the excited CPW samples were calculated. The results are depicted in figure 4.5 (a) and (b) for a frequency of 40 GHz. The model yields to the expected electric field distribution of a coplanar waveguide (see Sec.[2.2]), with the main signal propagating at the edges of the center track and the field lines pointing from the center track to the ground tracks, with periodically changing direction [56]. The signal is confined at the center track of the CPW and travels from the excited lumped port to the detecting lumped port at the other end of the sample. Figure 4.5 (c) and (d) depict the simulated transmission (green) and reflection (blue) spectra of the CPW samples. The calculated S_{21} -parameters prove to be reasonable low over the whole frequency spectrum for both samples, but alternate periodically in the $100\ \Omega$ sample. The alternation in the transmission signal arises from the pronounced resonances that are visible in the S_{11} parameters.

After the CPW samples were computationally analysed, I fabricated them with e-beam

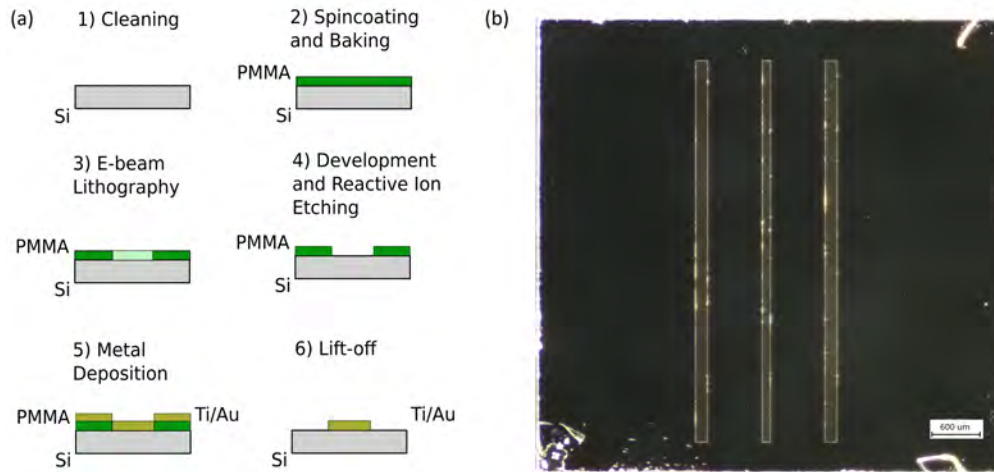


Figure 4.6.: (a) Different steps in the fabrication of the CPW samples, with the silicon substrate indicated in grey, the resist in green and the deposited metal layers indicated in gold. After cleaning, the Si-substrate is coated with Polymethylmethacrylat (PMMA) and heated on a hot plate. The structure then is patterned into the resist with e-beam lithography and developed with Methylisobutylketon (MIBK). The surface can be cleaned with reactive ion etching. Afterwards, titanium and gold is evaporated onto the pattern with thin film metal deposition. After the lift-off, the structure is transferred to the substrate. (b) High impedance- $100\ \Omega$ coplanar waveguide sample, fabricated in the clean room facilities at CEITEC.

lithography and thin film metal deposition in a clean room environment. Figure 4.6 (a) summarises the performed fabrication steps. Most nanofabrication techniques are planar processes starting with a substrate (usually a wafer or a chip) that acts as the backing of the fabricated sample. A Si-chip was used as the substrate for the CPW samples. To clean the Si-wafers, they were placed in a beaker with acetone and afterwards isopryl alcohol (IPA) in an ultrasonic bath for five minutes. After cleaning, the substrate is coated with a layer of resist, usually a thin layer of a chemically sensitive polymer. Here, the substrate was covered with Polymethylmethacrylat (PMMA) by spincoating for 60 s with 3000 rounds per minute. The Si-wafers then were baked at $180\ ^\circ\text{C}$ for 180 s on a covered hot plate. The desired structure is patterned into the resist by a lithographic technique and developed afterwards with a suitable chemical [57]. The patterning can either be achieved by scanning a focused beam from point to point with respect to a pre-designed pattern, or by exposure through a mask. Conventional lithographic exposures affect the chemical structure of the resist by changing its solubility and the response of the resist can either be positive or negative, depending if the exposed or unexposed areas will be removed after the development [58]. For this thesis, e-beam lithography was used to trace the CPW pattern into PMMA. As the resolution is limited by scattering processes of the beam electrons with the resist layer, the ultimate resolution of e-beam lithography is typically in the range of a few nanometers, depending on the energy of the electrons and the intrinsic properties of the used resist [57]. The pattern structure is usually created with a commercial software (here RAITH150) that is compatible with an e-beam writer. The e-beam, normally created by a Schottky emitter, is then scanned over the resist while being focused by electric or magnetic lenses and turned

on and off during the scan. The biggest limitation of e-beam lithography is its slow speed, which arises from the sequential writing process and the writing current, as high currents degrade the resolution [58]. Here, the e-beam lithography was performed with a MIRA3 XMU scanning electron microscope from the company TESCON. The structure was patterned into the resist with a writing field of $500\ \mu\text{m}$. The used beam parameters together with a dosage of $300\ \mu\text{C cm}^{-2}$ resulted in a lithography time of approximately 20 min per sample. After the lithography, the samples were put into the solvent Methylisobutylketon (MIBK) for 40 s to develop the patterned resist. After the development, the samples were cleaned with IPA. To remove remaining contaminations, the wafers were exposed to an O_2 -plasma beam for 5 s in a reactive ion etching system. After the lithography, the patterned structure needs to be transferred from the resist to the substrate, which can be achieved by numerous pattern transfer techniques [58]. Here, the structure of the CPW samples was transferred to the substrate by the deposition of a 10 nm thick film of Ti and a 60 nm thick film of Au. During the deposition, the sample was spinning with 10 rounds per minute, and a deposition rate of $1\ \text{\AA min}^{-1}$ for titanium and $2\ \text{\AA min}^{-1}$ for gold. For the lift-off, the samples were left in acetone for two hours and cleaned with IPA afterwards. Figure 4.6 (b) depicts the $100\ \Omega$ -version of the CPW sample, recorded with an optical microscope.

5. Propagating Spin-Wave Spectroscopy at Millikelvin Temperatures

In this chapter, we discuss the results of PSWS measurements at millikelvin temperatures. The experiments were performed with the installed dilution refrigerator system, its superconducting vector magnet, and a calibrated VNA measurement system. I was able to excite and detect MSSW in a YIG strip on a GGG substrate and compared the cryogenic results to room temperature studies, obtained in a standard electromagnet-based setup (see [1, 20]).

The PSWS measurements were all performed in a monocrystalline $70\text{ mm} \times 2\text{ mm} \times 5.65\text{ }\mu\text{m}$ YIG strip on a $500\text{ }\mu\text{m}$ thick GGG substrate, with a 30° edge-cut to avoid spin-wave reflection. The sample was glued onto a microantenna-PCB with GE-varnish and placed on top of two microstrip antennas, which allow to excite and detect spin waves in the sample (see Sec.[1.3]). The $50\text{ }\mu\text{m}$ wide antennas are separated by a 8 mm wide gap and can be connected to an Anritsu VectorStar VNA via two 2.92 mm -connectors and the dedicated KBL-2M-LOW+ (cryogenic measurement) or CBL-2M-SMSM+ (room temperature measurement) high-frequency cables. The used microantenna-PCB, with the YIG on GGG strip and an oxygen-free copper sample holder, is displayed in Fig. 5.1 (a). The Oersted field created by the microstrip antennas is strongest at the antennas termination, which is why the antenna is grounded shortly after the sample. Close to the 2.92 mm -connectors, the microstrip antennas characteristic impedance is matched with the standard value of $50\text{ }\Omega$. Fig. 5.1 (b) depicts the microantenna-PCB and the sample holder in an electromagnet-based room temperature PSWS measurement setup. The room temperature setup comprises a bipolar H-framed GMW electromagnet (150 mm pole separation, 70 A -coils, 85 V power supply), two 20 GHz -rated CBL-2M-SMSM+ cables, and a 20 GHz -rated Anritsu VectorStar VNA system. Fig. 5.1 (c) shows the YIG on GGG strip, together with the microantenna-PCB and the sample holder, mounted on the sample rods of the dilution refrigerators bottom loading system. The microstrip antennas are connected to ports 1 and 2 of the cryostat via two bent copper cables. The top plate of the cryostat was connected to a 40 GHz -rated Anritsu VectorStar VNA system with KBL-2M-LOW+ high-frequency cables (see Sec.[3.1]). If a VNA is used as microwave source and signal detector, spin waves that propagate in the gap between the input and detecting antenna, are visible as peaks in the recorded transmission spectra S_{12} and S_{21} . Here, the recorded transmission spectra of the VNA are analysed to verify first spin-wave propagation in the installed dilution refrigerator setup. The results are compared to the room temperature PSWS studies with the same YIG on GGG strip and microantenna-PCB. Fig. 5.2 displays the uncorrected S_{12} transmission spectra of recorded MSSWs at (a) room temperature and at (b) 45 mK , for a bias magnetic field of 200 mT . The peak in the S_{12} spectrum of Fig. 5.2 (b) represents the first recorded propagating spin wave in the installed dilution refrigerator system.

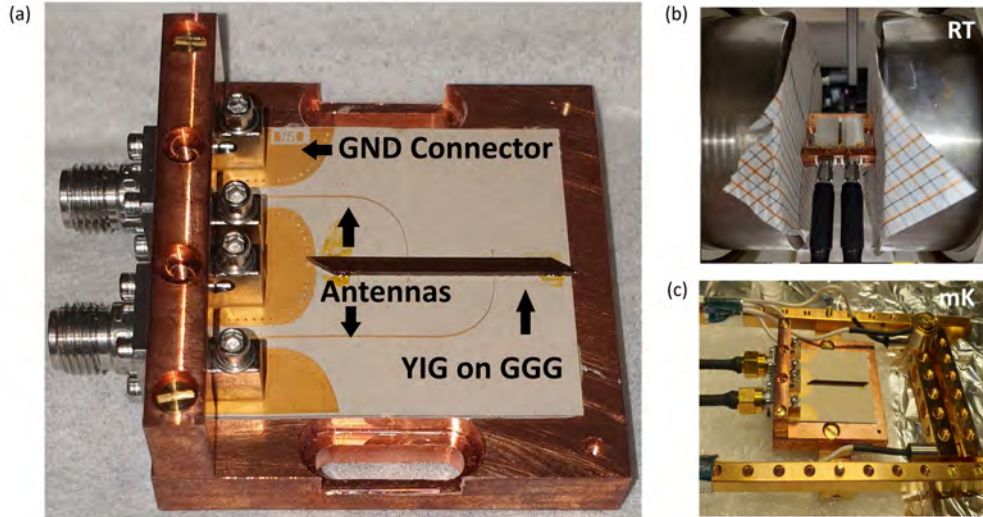


Figure 5.1.: (a) The microantenna-PCB, connected to two 2.92 mm-connectors on an oxygen-free copper holder. A $70\text{ mm} \times 2\text{ mm} \times 5.65\text{ }\mu\text{m}$ YIG strip on a $500\text{ }\mu\text{m}$ thick GGG substrate is placed on top of two microstrip antennas, which can excite and detect spin waves. (b) Photo of the used microantenna-PCB with the sample and the oxygen-free copper holder, placed in an electromagnet-based PSWS measurement setup in the MSSW configuration and (c) mounted to the sample rods of the dilution refrigerators bottom loading system.

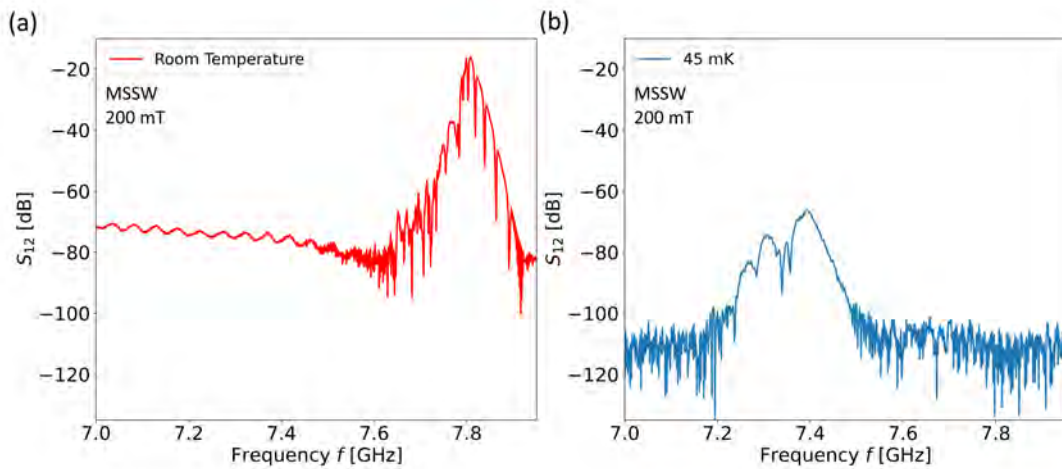


Figure 5.2.: Uncorrected S_{12} transmission spectra of (a) a room temperature and (b) a cryogenic PSWS measurement in the MSSW configuration. Both spectra were obtained for an applied bias field of 200 mT. The data were recorded for an input power of -15 dBm at room temperature and 0 dBm at the cryogenic measurements, with a base temperature of 45 mK.

The uncorrected S_{12} -parameters were averaged over 100 loops and obtained for an input power of -15 dBm at room temperature and 0 dBm at 45 mK. The different input powers were chosen because of the placed attenuators in the cryostats transmission lines. The attenuators indeed filter the input signal of the VNA, as is visible in the smooth signal level and peak of Fig. 5.2 (b), but they also increase the transmission signal losses. As the cryogenic PSWS measurements were performed at ports 1 and 2 of the dilution refrigerator, the attenuation losses (see table 3.1) lead to a decrease of the applied 0 dBm input power at the VNA to an effective input power of -15 dBm at the input antenna.

To allow a direct comparison of the transmission spectra, obtained in the room temperature and millikelvin PSWS measurements, the additional losses in the dilution refrigerators transmission lines (see Fig. 3.5 (a)) need to be considered. Due to the difference in the chosen number of points at the VNA for the two measurements, the losses of the cryostats transmission lines can't be directly subtracted from the S_{12} spectra displayed in Fig. 5.2 (b). Instead, the transmission line losses in the frequency range of 4 GHz to 11.6 GHz (expected spin-wave frequency range, see Fig. A.3 to A.8) were calculated with a linear fit, as displayed in Fig. 5.3. The calculated transmission losses allowed the correction of the cryogenic S_{12} and S_{21} spectra and enabled the comparison of the recorded data to the room temperature PSWS measurements. Fig. 5.4 displays the room temperature S_{12} spectra (a) and the millikelvin results (b), corrected with respect to the dilution refrigerators transmission losses.

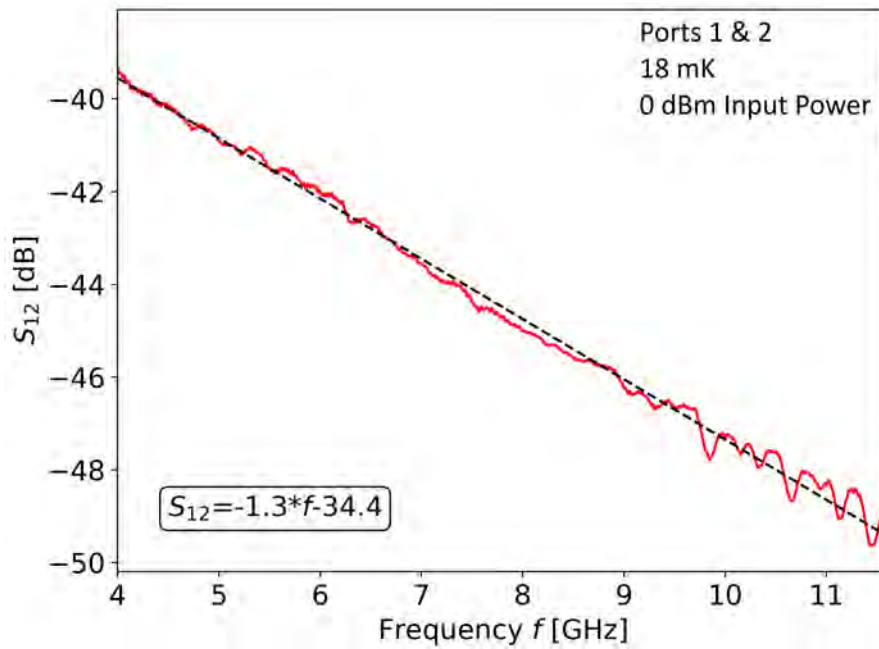


Figure 5.3.: Losses of the dilution refrigerators transmission lines in the frequency range of 4 GHz to 11.6 GHz at 18 mK and an input power of 0 dBm. The losses at these frequencies were also calculated with a linear fit (black dotted line), which allowed to correct the obtained cryogenic S_{12} spectra.

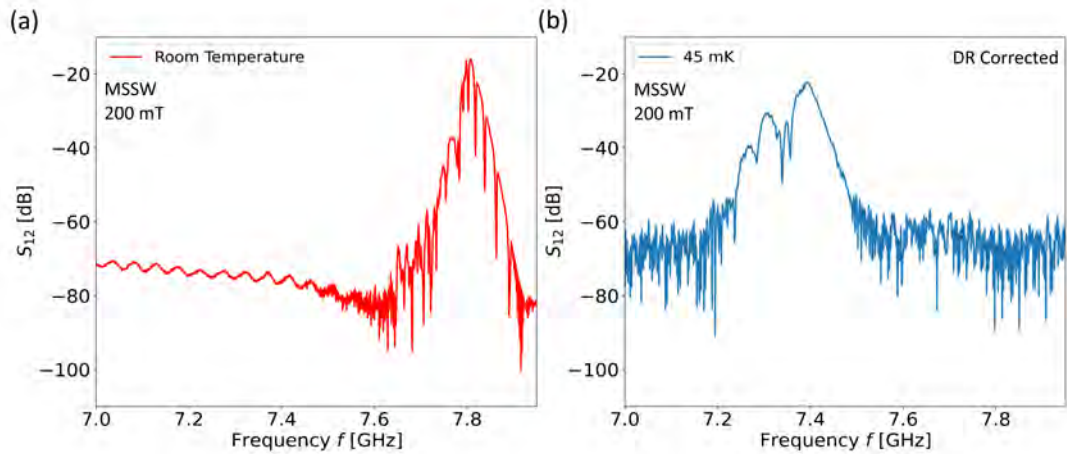


Figure 5.4.: S_{12} transmission spectra of (a) a room temperature and (b) a cryogenic PSWS measurement in the MSSW configuration. The data of the millikelvin PSWS study were corrected with respect to the dilution refrigerators transmission line and attenuation losses. Both spectra were obtained for an applied bias field of 200 mT. Spin waves were recorded for an input power of -15 dBm at room temperature and 0 dBm at the cryogenic measurements, with a base temperature of 45 mK.

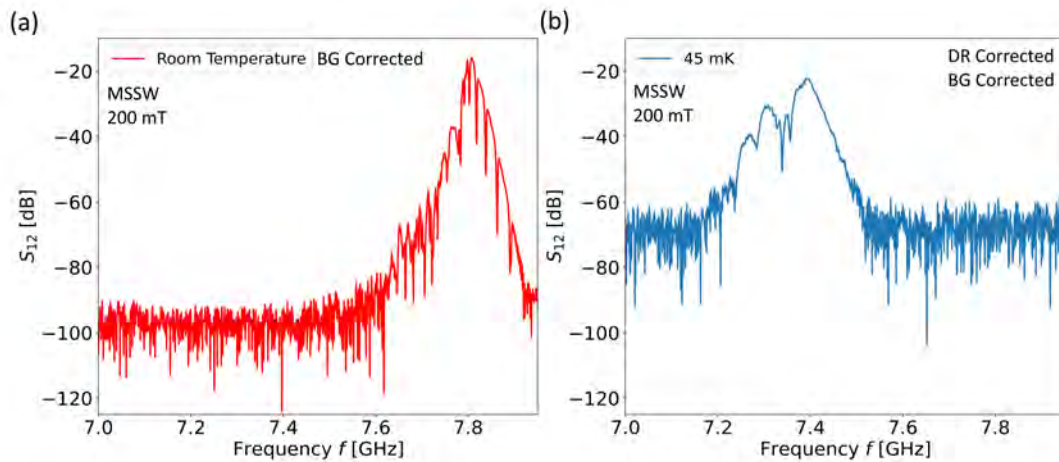


Figure 5.5.: S_{12} transmission spectra of (a) a room temperature and (b) a cryogenic PSWS measurement in the MSSW configuration. The data of the millikelvin PSWS study were corrected with respect to the dilution refrigerators transmission line and attenuation losses. Both spectra were corrected to the non-magnetic background and obtained for an applied bias field of 200 mT. Spin waves were recorded for an input power of -15 dBm at room temperature and 0 dBm at the cryogenic measurements, with a base temperature of 45 mK.

To minimise features in the transmission spectrum, which are not related to propagating spin waves, the S_{12} - and S_{21} -parameters were corrected to the non-magnetic signal background (see Fig. 5.5). Therefore, the spin-wave related peak in the spectrum was shifted out of the observed frequency range by an increase in the magnetic bias field. The remaining background signal level can be subtracted from the S_{12} and S_{21} spectra of the observed propagating spin wave. Fig. 5.6 (a) to (d) illustrates the transmission spectra S_{12} and S_{21} of PSWS experiments performed at room temperature and at a sample base temperature of 45 mK. The measurements were performed in the MSSW configuration at an external magnetic bias field of 200 mT (plots (a) to (b)) and -200 mT (plots (c) to (d)). The shown data include the correction of the dilution refrigerators transmission line losses, as explained for Fig. 5.4, are corrected with respect to the non-magnetic background, and were smoothed with the *scikit-rf*-package included in python (see [55]). The spin-wave linewidth in the observed spectra is designated by a black dotted line.

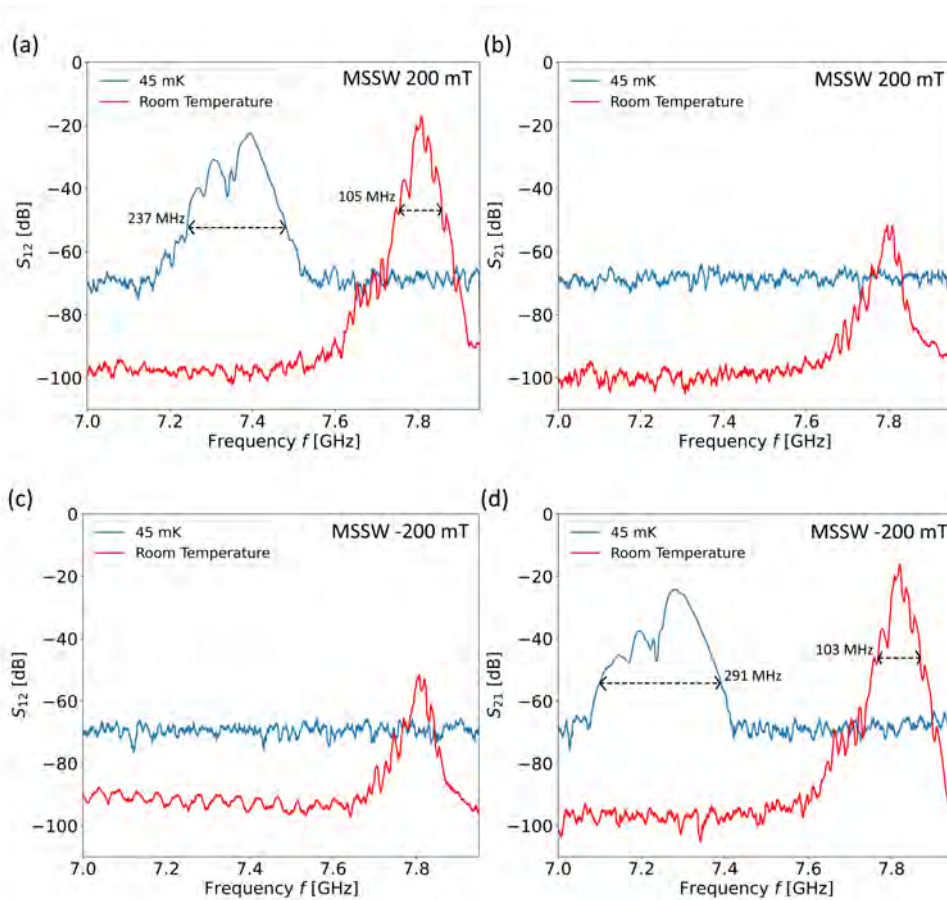


Figure 5.6.: S_{12} and S_{21} transmission spectra of a room temperature (red) and a millikelvin (blue) PSWS measurement in the MSSW configuration, with applied bias fields of 200 mT and -200 mT. The data were recorded for an input power of -15 dBm, background corrected, and the millikelvin results are corrected to the transmission losses of the dilution refrigerator, which allows direct comparison of the data.

Unlike FVMSWs and BVMSWs, which are volume modes and therefore have a cosinusoidal amplitude distribution of the magnetisation precession along the sample thickness, MSSWs are localised at the surface and the spin precession exponentially decreases with the sample thickness [1, 6]. MSSWs which are excited in a thin-film waveguide with microstrip antennas, exhibit a nonreciprocal character, as the spin wave only propagates in one direction of the sample. This non-reciprocity is related to the interference of components of the antennas induced Oersted field (see Sec.[1.3]). For MSSWs, the geometry of the excitation mechanism leads to two microwave magnetic field components (vertical and horizontal), that participate in the spin-wave excitation, which is constructive for one propagation direction and destructive in the other [1, 59].

Hence, for a bias field of 200 mT a spin wave should only be visible in the S_{12} spectrum and vice versa for the opposing field direction. Although they are smaller, Fig. 5.6 (b) and (c) also exhibit spin-wave peaks and the expected non-reciprocity of the MSSW is not completely acknowledged by the experimental results. The detection of spin waves in the opposing direction is owed to the finite thickness of the used YIG film on the GGG substrate. At an external field of 200 mT, the maximum of the spin precession is located at the upper sample surface and a MSSW peak is visible in the S_{12} propagation direction. However, the spin-wave excitation can be switched to the bottom surface of the sample if the propagation direction of the MSSW is reversed. Therefore, a lower signal of the MSSW, propagating on the bottom surface, can still be detected in the S_{21} direction, because the thickness of the YIG film is limited with 5.65 μm .

Fig. A.3 to A.8 in the appendix display the transmission spectra S_{12} and S_{21} at bias magnetic fields ranging from 300 mT to -300 mT and were observed at room temperature and at 45 mK. The comparison of the PSWS measurements at 45 mK and at room temperature reveals, that although no thermal magnons are present at millikelvin temperatures, the peak amplitude in the cryogenic measurements is decreasing compared to room temperature. This difference in the amplitude is the smallest (only considering the recorded data points) at a bias field of 200 mT and -200 mT with 5.47 dB and 8.07 dB difference. The divergence between the amplitudes increases for bigger absolute field magnitudes. Below the saturation magnetisation of YIG at 10 mK ($M_0 = 197 \text{ kA m}^{-1}$), the amplitude difference increases for smaller absolute field magnitudes.

Here, it is important to acknowledge that the used YIG strip is grown on a GGG substrate. As the lattice constant of GGG is well matched to YIG, GGG allows the fabrication of defect-free and unstressed YIG films [1]. GGG exhibits paramagnetic behaviour and therefore increases the damping in films that are grown on its surface at millikelvin temperatures. Due to the higher damping, the signal amplitude in the transmission spectrum at millikelvin temperatures decreases for YIG films grown on GGG [60]. The increasing change of the amplitude difference with absolute field magnitudes above M_0 can be explained with the dependency of the Gilbert-damping α on the applied input power. It was observed in [60], that the damping in YIG films grown on GGG increases with decreasing input power at millikelvin base temperatures. As the spin-wave frequency of MSSW increases with the absolute magnitude of the applied field (see Fig 1.3 or equation 1.7), the transmission losses of the dilution refrigerators transmission lines increase simultaneously, resulting in a lower effective input power at the microstrip antennas. Hence, the Gilbert-damping in the dilution refrigerator increases with frequency and amplifies the amplitude decrease related to GGG at millikelvin temperatures. Additionally, further experiments or simulations will have to investigate the used microstrip antennas and microantenna-PCB in cryogenic measurements, to exclude the possibility that the amplitude

decrease at increasing absolute field magnitudes is related to the excitation and detection efficiency of the antennas.

Fig. 5.6 (a) and (d) illustrate a shift to a smaller spin-wave frequency and an increase of the spin-wave linewidth at a base temperature of 45 mK, compared to the room temperature results. To further analyse these effects, the dispersion curve of the 70 mm×2 mm×5.65 μm YIG strip on the 500 μm thick GGG substrate was calculated for the external bias magnetic field of 200 mT with equation 1.7. The calculation of the dispersion curve needs to consider the higher value of the saturation magnetisation M_0 of YIG at millikelvin temperatures (see [14]):

$$M_0(300\text{ K}) = 140\text{ kA m}^{-1}, \quad M_0(45\text{ mK}) = 196\text{ kA m}^{-1}.$$

Fig. 5.7 displays (a) the S_{12} spectra of the PSWS measurements at a bias field of 200 mT and (b) the corresponding dispersion curves. The FMR-frequency f_{FMR} of the MSSWs was calculated with equation 1.9 and indicated in the S_{12} spectra of Fig. 5.7 (a) by black dotted lines.

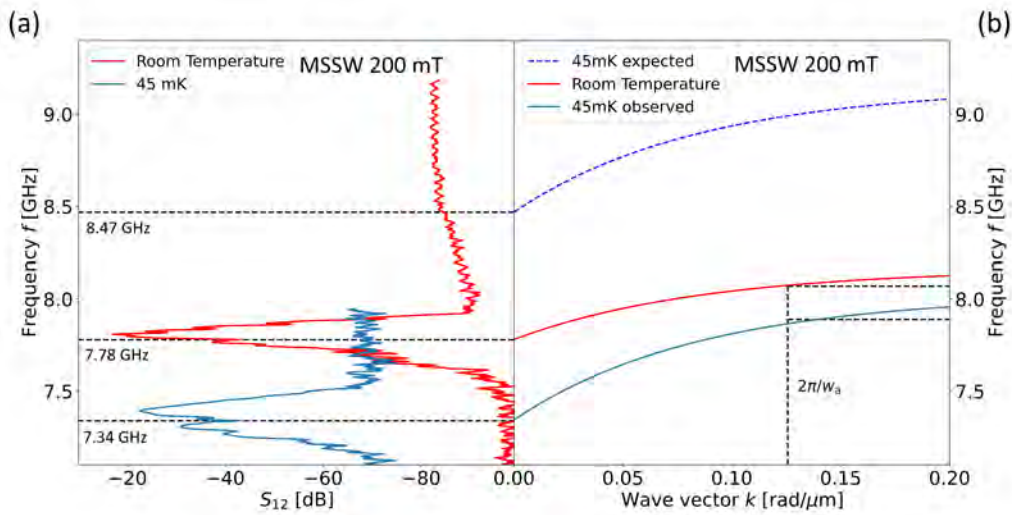


Figure 5.7.: (a) S_{12} spectrum of recorded MSSWs at room temperature and at 45 mK with an external bias magnetic field of 200 mT. The FMR-frequency f_{FMR} of the spin waves is designated with black dashed lines. (b) Dispersion relation of a MSSW at a bias field of 200 mT, calculated with equation 1.7. The blue dashed line shows the calculated dispersion relation at millikelvin, while the continuous blue line illustrates the dispersion curve of the experimentally recorded spin wave. The black dashed lines indicate the k -vectors that can be excited with the 50 μm wide microstrip antennas. The FMR-point was calculated with equation 1.9, including an introduced anisotropy field $\mu_0 H_a = 10\text{ mT}$ (see Sec.[1.3]).

The features in the spectra, visible before the FMR point (also see Fig. A.3 to A.8), are related to standing thickness or width spin-wave modes in the YIG strip [1, 20]. The first calculated FMR-point (room temperature measurement) was shifted for 100 MHz by the introduction of the anisotropy field $\mu_0 H_a = 10$ mT, to accord with the distinct point of the experimentally recorded fundamental propagating spin-wave mode, resulting in $f_{\text{FMR}}(300 \text{ K}) = 7.78$ GHz. This anisotropy field $\mu_0 H_a$ was retained for all following calculations. The calculated dispersion curve of the room temperature measurements is depicted in Fig. 5.7 (b) as the red line.

To determine the possible wave vectors, which the $50 \mu\text{m}$ thick microstrip antennas can excite and detect, the first minimum $2\pi/w_a$ of the *sinc*-shaped pulse signal (spectral representation, Fourier-transform of the rectangular pulse signal in the time domain) is illustrated by a black dotted line. The used antennas are able to excite wave vectors up to $k = 0.126 \text{ rad } \mu\text{m}^{-1}$ or spin waves with frequencies up to 8.07 GHz at a bias field of 200 mT. The comparison of the dispersion curve and the S_{12} spectrum at room temperature reveals, that we are not able to observe wave vectors up to the possible maximum of $k = 0.126 \text{ rad } \mu\text{m}^{-1}$. A possible explanation for this observed effect could be the non-linear drop in the excitation and detection efficiency of the antennas, due to the *sinc*-shaped pulse.

The dispersion curve of the cryogenic measurement was calculated with the corresponding saturation magnetisation $M_0(45 \text{ mK}) = 196 \text{ kA m}^{-1}$ and is displayed by the dark blue dashed line. The higher saturation magnetisation of YIG at millikelvin temperatures leads to an increased slope of the dispersion curve, compared to room temperature. The increased slope explains the broader linewidth of the spin waves at 45 mK. The spin-wave linewidth Δf between the room temperature and the cryogenic measurement increased for 132 MHz at a field of 200 mT and for 188 MHz at a field of -200 mT.

The corresponding FMR-point at 45 mK was calculated with equation 1.9, including the anisotropy field $\mu_0 H_a = 10$ mT which was introduced for the room temperature data. The calculations resulted in the theoretically expected FMR-frequency of $f_{\text{FMR}}(45 \text{ mK}) = 8.47$ GHz. The recorded millikelvin S_{12} spectrum, represented by the blue curve of Fig. 5.7 (a), reveals that the theoretically expected dispersion curve does not agree with the experimentally obtained results. The experimentally determined FMR-frequency at 45 mK resulted in $f_{\text{FMR}}(45 \text{ mK}) = 7.34$ GHz, leading to a difference of 1.13 GHz between the expected and observed spin-wave frequency at a bias field of 200 mT. The observed discrepancy states a shift of the experimentally obtained dispersion curve to lower frequencies and therefore disagrees with the theoretically expected increase of the spin-wave frequency due to the higher M_0 .

The occurring frequency shift would suggest a modification of the theoretically predicted FMR-frequency (see equation 1.9) at millikelvin temperatures. This modification could be related to a defective calibration of the superconducting vector magnet, which would result in an amplitude offset of the applied external bias field, which is linearly rising with H_0 . If so, the observed frequency shift of 1.13 GHz at $\mu_0 H_0 = 200$ mT would require a field modification to $\mu_0 H_0 - \mu_0 H_{\text{cal}} = 163.5$ mT. Here, H_{cal} describes the field deviation that would lead to the observed difference between the expected and experimentally determined FMR-frequencies. It is also possible, that the frequency shift is related to a change of the anisotropy field H_a at millikelvin temperatures (see [61]).

To further investigate the observed frequency shift, a field H_0 versus frequency f_{FMR} plot is displayed in Fig. 5.8. This plot allows to compare the theoretically expected curves, calculated with equation 1.9 for the corresponding saturation magnetisation, with the experimentally recorded data. The experimental room temperature measurements (red dots) comply with the theoretically calculated FMR-points (red solid line) and the cryogenic experimental results

(blue dots) indeed to not confirm the expected results of equation 1.9 (blue solid line). If the shift of the experimentally determined FMR-points to lower frequencies is induced by a temperature dependent anisotropy field, the field magnitude $\mu_0 H_a$ would need to change from 10 mT to -110 mT between room temperature and 45 mK (see black dotted line in Fig. 5.8). For absolute bias fields $\mu_0 H_0$ below 100 mT it is possible that the applied current of the superconducting vector magnets control unit is not steady enough to guarantee a reliable magnet operation. Additionally, remanence effects in the magnet coils can lead to an offset at small applied magnetic bias fields $\mu_0 H_0$. The extent of the offset depends on the sequence of applied fields. During the cryogenic PSWS measurements, spin waves were first recorded for positive bias fields from 80 mT to 350 mT. Afterwards, spin waves were detected for the bias fields -80 mT to -350 mT. Hence, the data of the negative bias fields exhibit an offset shift of the magnetic field magnitude, due to remanence in the magnet coils. This offset appears in Fig. 5.8 as a spin-wave frequency shift between the bias fields of -80 mT and 80 mT.

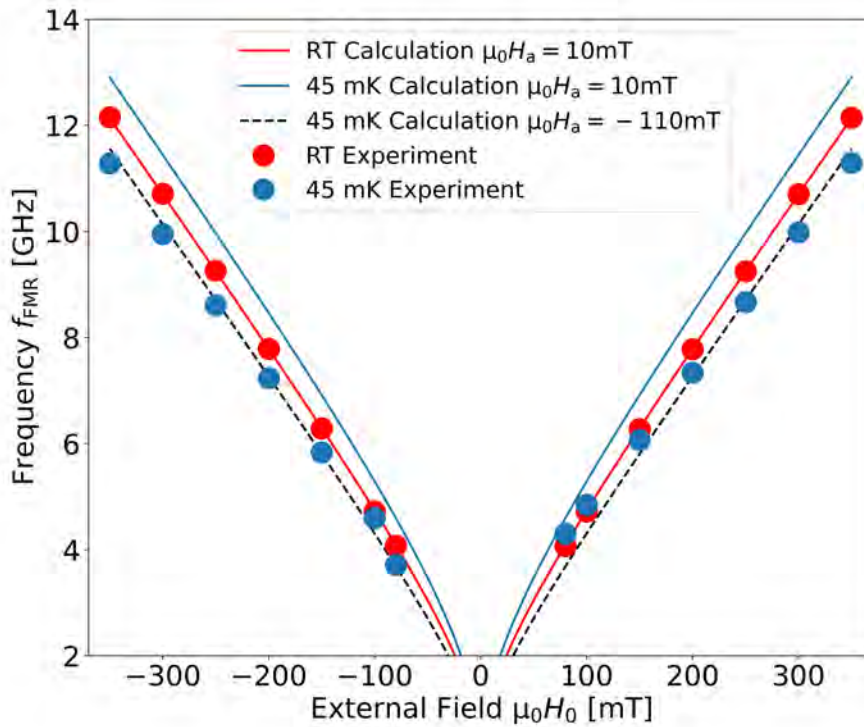


Figure 5.8.: Field $\mu_0 H_0$ versus frequency f_{FMR} plot for MSSWs with applied bias fields ranging from -350 mT to 350 mT. The continuous red and blue line display the theoretically expected FMR-points at room temperature and at 45 mK, calculated with equation 1.9. The results obtained with PSWS at room temperature and at 45 mK are illustrated by red and blue dots (error included in the dot-size).

The frequency difference leads to a remanence related offset field of $\mu_0 H_{\text{rem}} = 16 \pm 0.5 \text{ mT}$ between the bias magnetic fields of $\mu_0 H_0 = 80 \text{ mT}$ and $\mu_0 H_0 = -80 \text{ mT}$. This remanence

effect becomes less relevant with increasing absolute field magnitude, as Fig. 5.8 and Fig. A.3 to Fig. A.8 demonstrate.

Beside a temperature dependent anisotropy field H_a , the frequency shift at millikelvin temperatures could also be related to a defective calibration of the superconducting vector magnet, leading to an amplitude offset, which is dependent on the external bias field H_0 . The difference $\mu_0 H_{cal}$, between the applied external field and the field magnitude that would lead to the dispersion curves of the experimentally observed spin waves at 45 mK, is depicted in Fig. 5.9 (a) and (b).

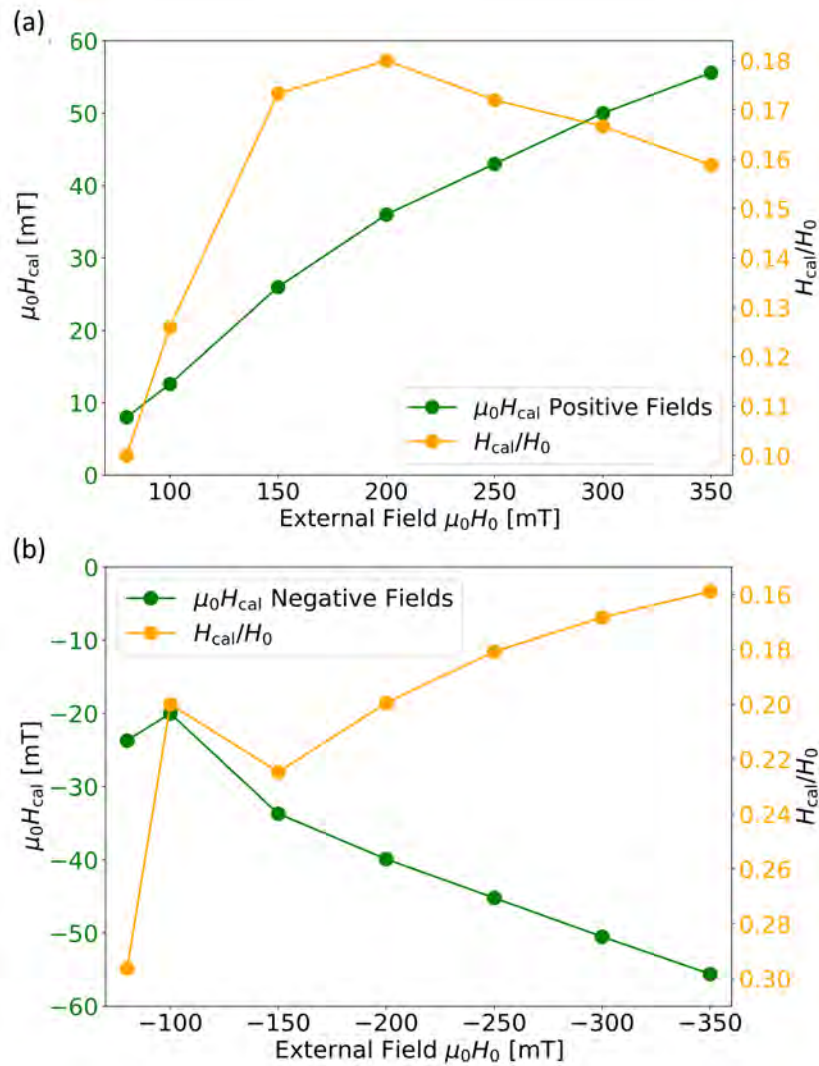


Figure 5.9.: Difference $\mu_0 H_{cal}$ between the applied external field and the field magnitude, which would lead to the dispersion curves of the experimentally observed spin waves at 45 mK. (a) $\mu_0 H_{cal}$ and H_{cal}/H_0 for positive bias magnetic fields. (b) H_{cal}/H_0 for negative bias magnetic fields (error included in the dot-size).

If the spin-wave frequency shift at millikelvin temperatures is introduced by a calibration related amplitude offset, H_{cal} would be expected to increase linearly with the absolute magnitude of the applied magnetic field H_0 . This linear increase of H_{cal} should be visible in Fig. 5.9 (a) and (b), especially at fields bigger than 200 mT. For absolute field magnitudes below 200 mT, deviations from the expected linear dependence of H_{cal} on H_0 are possible due to a non-saturated YIG sample. If H_{cal} increases linearly with H_0 , the ratio H_{cal}/H_0 (orange curve in Fig. 5.9) should not change with the applied external bias fields. The data reveal, that H_{cal}/H_0 is not constant over the range of applied bias fields, as the curve decreases at positive and negative fields H_0 . Therefore, Fig. 5.9 (a) and (b) would suggest, that the observed frequency shift visible in Fig. 5.8 is not related to the calibration of the vector magnet. However, as it was not possible to detect spin waves at frequencies above 12.16 GHz, due to the decrease in the spin-wave amplitude, the ratio H_{cal}/H_0 could still become constant at higher field magnitudes $\mu_0 H_0$. Thus, a modification of H_0 due to a defective calibration of the superconducting vector magnet can not be ruled out with the recorded results. Nevertheless, although a re-calibration of the superconducting magnet is not possible in the near future, due to the absence of a 3D Hall probe array, the magnetic field could be surveyed with another experiment.

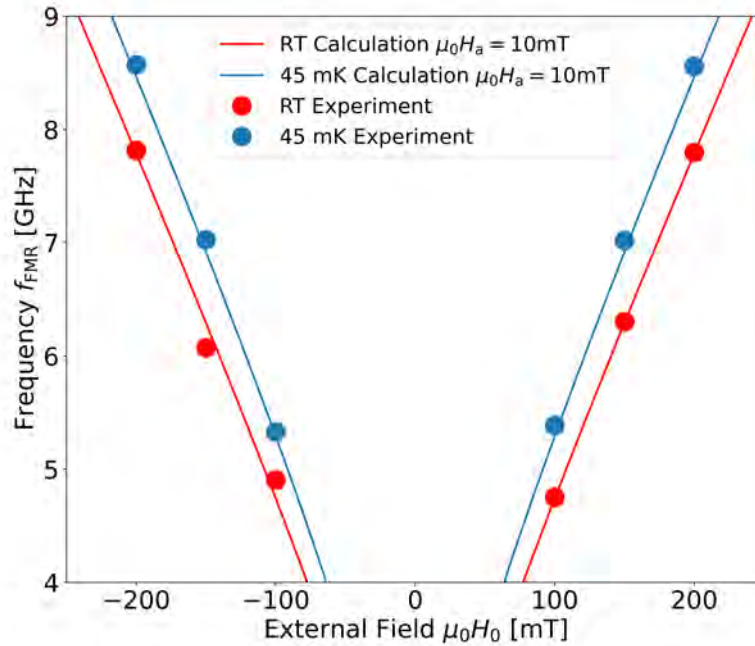


Figure 5.10.: Field $\mu_0 H_0$ versus frequency f plot for BVMSWs with applied bias fields ranging from -200 mT to 200 mT. The continuous red and blue line display the theoretically expected FMR-points at room temperature and at near zero temperatures, calculated with equation 1.9. The results obtained with PSWS at room temperature and at 137 mK are illustrated by red and blue dots (error included in the dot-size).

Additionally to the MSSW experiments, spin waves were also recorded in the BVMSW configuration at cryogenic temperatures. Here, the recorded S_{12} and S_{21} spectra are not displayed due to the inefficient excitation of BVMSW with the used microstrip antennas (see [1, 6]) and the limited input power, that can be applied at the VNA to still achieve millikelvin base temperatures. However, it was possible to excite and detect BVMSW in the built cryogenic PSWS setup, with the frequencies of the observed peak maxima in the S_{12} spectra depicted in Fig. 5.10. Because of the inefficient excitation of the BVMSW, the observed amplitudes in the S_{12} spectra were too small to define the distinct FMR-frequency in the experimentally obtained data. Therefore, Fig. 5.10 displays the frequency position of the recorded peak maxima of the S_{12} spectra, with bias magnetic fields ranging from -200 mT to 200 mT. The data were obtained for an input power at the VNA of 12 dBm and averaged over 200 loops. As the bias field is oriented in-plane and along the propagation direction of the spin waves, the z -axis of the superconducting vector magnet (solenoid coil) was used to apply the field $\mu_0 H_0$. Fig. 5.10 reveals, that the spin-wave frequency increases at millikelvin temperatures compared to room temperature, which would be expected due to the higher saturation magnetisation M_0 of YIG at such temperatures. The solid lines in Fig. 5.10 represent the theoretically expected FMR-frequencies calculated with equation 1.9. The agreement of the BVMSW measurements with the theoretically expected spin-wave frequencies would suggest, that the magnetic bias field of the superconducting vector magnet in the z -axis is calibrated correctly. The results of the cryogenic PSWS measurements in the MSSW configuration therefore could be tested by the rotation of the sample or microantenna-PCB, to allow the application of external magnetic fields in the z -axis. If the results of this experiment would lead to an increase of the spin-wave frequency compared to the room temperature studies, the split coils in the x - and y -direction indeed need to be re-calibrated. If the shift of the dispersion curve at millikelvin temperatures to lower frequencies is confirmed in these measurements, further investigations will be necessary to proof if other intrinsic physical phenomena, like for example a possible temperature dependence of the anisotropy field H_a (see [61]), emerge and contribute at such low temperatures.

In summary, the cryogenic PSWS measurement setup allowed to detect MSSWs at a base temperature of 45 mK in a $70 \text{ mm} \times 2 \text{ mm} \times 5.65 \text{ }\mu\text{m}$ YIG strip on a $500 \text{ }\mu\text{m}$ thick GGG substrate. Spin-wave spectra were recorded for bias magnetic fields in the range of -300 mT to 300 mT and compared to room temperature studies, which were performed in an electromagnet-based setup. The comparison of the obtained results revealed a decrease of the spin-wave frequency at millikelvin temperatures, despite the increased saturation magnetisation M_0 of YIG at near zero temperatures. Further investigations will have to be performed to clarify if this frequency shift is introduced by a defective calibration of the dilution refrigerators superconducting vector magnet or if other physical phenomena, such as a temperature dependent anisotropy field, emerge at millikelvin temperatures.

6. Conclusions and Outlook

In this thesis I have been able to build and characterise a state-of-the-art dilution refrigerator (BlueFors LD250), including its superconducting vector magnet, and a 40 GHz-rated VNA measurement system. This setup allowed me to demonstrate the first low temperature propagation of spin waves in yttrium iron garnet (YIG) on gadolinium gallium garnet (GGG) slabs in our laboratory. Further, I used computational methods to design and analyse a multilayer high-frequency PCB, to act as a connecting interface between the measurement setup and the investigated samples. Due to its functionalities, this PCB will enable the use of e-beam patterned antenna structures in a wide frequency range for different samples. The high-frequency PCB, together with the dilution refrigerator system, builds a measurement platform for cryogenic propagating spin-wave spectroscopy (PSWS).

However, the measurement platform can be optimised. For example, the attenuators in the cryostat are currently balanced to reach base temperature while filtering out noise (see Sec. [3.2]). Future research will determine, if this balance needs to be adjusted. Also, the PSWS experiments in the magnetostatic surface spin-wave configuration (see Fig. 5.6) and a field versus frequency plot (see Fig. 5.8) revealed a decrease of the spin-wave frequency at a base temperature of 45 mK compared to room temperature. Due to the higher saturation magnetisation of YIG at millikelvin temperatures, equation 1.9 would actually predict an increase of the spin-wave frequency in the cryogenic PSWS measurements. The disagreement between the theoretically expected and the experimentally recorded results may originate from an amplitude offset related to the calibration of the superconducting vector magnet. Cryogenic PSWS measurements in the BVMSW configuration (see Fig. 5.10) revealed an increase of the spin-wave frequency and acknowledged the expected theoretical results. As the BVMSW measurements were performed with a bias field of the superconducting vector magnet in the z -direction (solenoid coil), the modification of the external bias field could be related to a defective calibration of the split coils that create the magnetic field in the x - and y -direction. The results of the cryogenic PSWS measurements in the MSSW configuration therefore could be tested by the rotation of the sample or microantenna-PCB, to allow the application of external magnetic fields in the z -axis. If the results of this experiment would lead to an increase of the spin-wave frequency compared to the room temperature studies, the split coils in the x - and y -direction indeed need to be re-calibrated.

If the shift of the spin-wave dispersion curve at millikelvin temperatures to lower frequencies is confirmed in these measurements, further experiments will need to investigate the effect of the temperature dependence of the samples anisotropy field H_a (as suggested in [61]). Such experiments could for example compare the results of PSWS measurements with thin-film YIG on GGG samples to the recorded data of the $70\text{ mm} \times 2\text{ mm} \times 5.65\text{ }\mu\text{m}$ YIG strip on the $500\text{ }\mu\text{m}$ thick GGG substrate.

The full measurement setup, realised in this thesis, will enable future researchers to work beyond the limitations of room temperature experiments. Within a project of the Nanomagnetism and Magnonics group, first PSWS-based experiments with paramagnetic materials, such as GGG, have already been performed. Spin-wave propagation in paramagnetic materials has not

been recorded yet and is believed to be only observable at millikelvin base temperatures. Kosen S. *et al.* [60] have shown that the Gilbert damping constant α decreases at millikelvin temperatures for substrate-free YIG samples, but increases for YIG samples grown on GGG. The bigger damping is caused by the paramagnetic character of GGG. The experiments performed in [60] resulted in an increase of α by a factor of 3.4 between 300 K and 20 mK for a $2\text{ mm} \times 3\text{ mm} \times 10\text{ }\mu\text{m}$ YIG film on GGG. Due to the increased damping, the detection of spin waves in the built cryogenic setup was challenging, as the input powers are limited for the access to millikelvin base temperatures. Nevertheless, the recorded results of the millikelvin PSWS measurements proofed the detection of propagating spin waves and therefore verified that YIG samples grown on GGG are in general suitable for experiments in the cryogenic environment. Future experiments in the field of quantum magnonics are still expected to use YIG samples for the investigation and utilisation of single magnons. Tabuchi Y. *et al.* [3] achieved to demonstrate the first detection of a single magnon in a YIG sphere by coherent coupling to a superconducting qubit, situated in a microwave cavity.

As research is pushing towards solutions for on-chip magnonic systems, experiments within the Nanomagnetism and Magnonics group will focus on the investigation of single magnons in sub-100 nm wide YIG waveguides grown on GGG. Although the step towards the nanoscale proves to be very challenging with YIG, due to its complex crystallographic structure, the fabrication of YIG waveguides down to widths of 50 nm was already achieved by Heinz B. *et al.* [19]. The efficient excitation and detection of single magnons in such sub-100 nm wide structures will be one of the main challenges for experiments in the recent future. As the detection of single magnons with superconducting structures was already demonstrated by Tabuchi Y. *et al.*, this approach also is of interest for waveguide structures.

Progress in the development of efficient single magnon sources and detectors would also enable experiments in combination with other physical systems. Such experiments could follow the example of the various achievements in the coupling of single photons to mechanical oscillators on the single phonon level (see [62, 63]). Moreover, microwave excitations have proven to be capable to couple with optical photons [64, 65] and magnons generated interest to be used as quantum transducers between microwave quantum information and quantum optics [7]. The prospect of microwave and also optical magnon-photon hybrid systems offers great potential for future applications. The built and characterised dilution refrigerator system provides the possibility to perform such experiments in the cryogenic environment. Direct optical access to the cryostat is given by either small windows in the x -, y -, and z -direction or via optical fibres. Moreover, nano-positioning stages would allow the alignment of the magnonic waveguides or the microwave excitations to additional optical systems. The prospects of performing further experiments in the field of hybrid opto-magnonic quantum systems at a foundational level, together with the demonstration of spin-wave propagation at low temperatures, show the unique technological capabilities that have been created within the frame of this work.

Acknowledgements

First, I would like to express my gratitude to Dr. Sebastian Knauer. All the experiences and my integration into the daily laboratory work would not have been possible without his close support and supervision. The training I received from Dr. Knauer, not only on the dilution refrigerator and the laboratory equipment, but also in terms of presentations and scientific writing, prepared me for my future career with a broad skill set. I am especially thankful for the opportunity to get familiar with e-beam lithography and other nanofabrication techniques at the cleanroom facilities of the Central European Institute of Technology in the Czech Republic. Beside that, Dr. Knauer constantly supported me during my lecture courses and, together with Prof. Andrii Chumak, encouraged me to apply for the Magnonics 2022 conference in southern California. I also want to thank Prof. Chumak, who not only supervised my master thesis, but also granted me the opportunity to work as a student assistant researcher. Prof. Chumak supported me to join his research group directly after my undergraduate studies and therefore provided me insights to the scientific daily routine in a team of young and ambitious scientists. Due to the trust of Prof. Chumak, I had the chance to work in state-of-the-art laboratories and gain experience with high-technology equipment already before the start of my master thesis. I want to thank Dr. Knauer and Prof. Chumak for the opportunity to make but also learn from mistakes and the trust they gave me during my employment and my master thesis. Moreover, I want to thank my colleagues and friends Sabri Koraltan, Barbora Budinska, Noura Zenbaa, Khrystyna Levchenko, Qi Wang, Sebastian Lamb-Camarena, Pedro del Real Lavergne, Andrey Voronov, and Rostyslav Serha for fruitful discussions, helpful advice, and great company. I am especially grateful to my friend Sabri Koraltan, whose support and friendship accompanied me since my first days as a physics student at the University of Vienna.

Next, I want to emphasise my gratitude to Christian Tauber, Peter Wlasits, Paul Winkler and Paulus Bauer, whose encouragement and support during my undergraduate studies also immensely helped me in finishing this thesis.

Finally, I would like to thank my family and friends. My parents Dagmar and Roland and also my stepfather Walter supported me throughout my studies not only financially but also with their encouragement and open arms in tough times. Additionally, I want to thank my sister Katja, my brother Elias, my girlfriend Jasmin and my dear friends Fabian, Florian, Ludwig and Sascha for their patience, their curiosity, and the advice they shared with me. I would not have been able to graduate without their support. Last I also want to thank my grandfather Werner, who never got tired to answer my questions and always encouraged me to stay curious.

Bibliography

- [1] A. A. Serga, A. V. Chumak and B. Hillebrands. “YIG magnonics”. In: *Journal of Physics D: Applied Physics* 43.26 (2010). ISSN: 00223727. DOI: 10.1088/0022-3727/43/26/264002.
- [2] Dany Lachance-Quirion et al. “Hybrid quantum systems based on magnonics”. In: *Applied Physics Express* 12.7 (2019). ISSN: 18820786. DOI: 10.7567/1882-0786/ab248d. eprint: 1902.03024.
- [3] Yutaka Tabuchi et al. “Quantum magnonics: The magnon meets the superconducting qubit”. In: *Comptes Rendus Physique* 17.7 (2016). Quantum microwaves / Micro-ondes quantiques, pp. 729–739. ISSN: 1631-0705. DOI: <https://doi.org/10.1016/j.crhy.2016.07.009>.
- [4] Björn Heinz et al. “Parametric generation of spin waves in nano-scaled magnonic conduits”. In: June (2021). arXiv: 2106.10727.
- [5] F Bloch. “Zur Theorie des Ferromagnetismus”. In: *Zeitschrift für Physik* 61.3 (1930), pp. 206–219. ISSN: 0044-3328. DOI: 10.1007/BF01339661.
- [6] Philipp Pirro et al. “Advances in coherent magnonics”. In: *Nature Reviews Materials* 6.12 (2021), pp. 1114–1135. ISSN: 20588437. DOI: 10.1038/s41578-021-00332-w.
- [7] Yi Li et al. “Hybrid magnonics: Physics, circuits, and applications for coherent information processing”. In: *Journal of Applied Physics* 128.13 (2020). ISSN: 10897550. DOI: 10.1063/5.0020277. eprint: 2006.16158.
- [8] O. V. Dobrovolskiy et al. “Magnon–fluxon interaction in a ferromagnet/superconductor heterostructure”. In: *Nature Physics* 15.5 (2019), pp. 477–482. ISSN: 17452481. DOI: 10.1038/s41567-019-0428-5.
- [9] Soshin Chikazumi and C. D Graham. *Physics of Ferromagnetism*. eng. International series of monographs on physics. Oxford: Oxford University Press, 1997. ISBN: 9780199564811.
- [10] K.M. Krishnan. *Fundamentals and Applications of Magnetic Materials*. Oxford University Press, 2016. ISBN: 9780199570447.
- [11] Claas Abert. “Micromagnetics and spintronics: models and numerical methods”. In: *European Physical Journal B* 92.6 (2019). ISSN: 14346036. DOI: 10.1140/epjb/e2019-90599-6.
- [12] A.G. Gurevich and G.A. Melkov. *Magnetization Oscillations and Waves*. Taylor & Francis, 1996. ISBN: 9780849394607.
- [13] D.D. Stancil and A. Prabhakar. *Spin Waves: Theory and Applications*. Springer US, 2009. ISBN: 9780387778655.
- [14] D.D. Stancil. *Theory of Magnetostatic Waves*. Springer-Verlag, 1993. ISBN: 9780387979694.
- [15] Li Min Zheng et al. *Magnon Spintronics*. 2015, pp. 1505–1551. ISBN: 9789400768925. DOI: 10.1007/978-94-007-6892-5_26.

- [16] Anjan Barman et al. "The 2021 Magnonics Roadmap". In: *Journal of Physics Condensed Matter* 33.41 (2021). ISSN: 1361648X. DOI: 10.1088/1361-648X/abec1a.
- [17] Thomas L. Gilbert. "A phenomenological theory of damping in ferromagnetic materials". In: *IEEE Transactions on Magnetics* 40.6 (2004), pp. 3443–3449. ISSN: 00189464. DOI: 10.1109/TMAG.2004.836740.
- [18] T Böttcher et al. "Fast long-wavelength exchange spin waves in partially-compensated Ga: YIG". In: 102401.December 2021 (2021). DOI: 10.1063/5.0082724.
- [19] Björn Heinz et al. "Propagation of Spin-Wave Packets in Individual Nanosized Yttrium Iron Garnet Magnonic Conduits". In: *Nano Letters* 20.6 (2020), pp. 4220–4227. ISSN: 15306992. DOI: 10.1021/acs.nanolett.0c00657.
- [20] Marek Vaňatka et al. "Spin-wave dispersion measurement by variable-gap propagating spin-wave spectroscopy". In: 054033 (2021), pp. 1–10. DOI: 10.1103/physrevapplied.16.054033. arXiv: 2107.09363.
- [21] A. V. Chumak et al. "Roadmap on Spin-Wave Computing". In: *arXiv e-prints*, arXiv:2111.00365 (Oct. 2021), arXiv:2111.00365. arXiv: 2111.00365 [physics.app-ph].
- [22] Babak Zare Rameshti et al. *Cavity Magnonics*. 2021. arXiv: 2106.09312 [cond-mat.mes-hall].
- [23] IIR-IIF Paris. *New International Dictionary of Refrigeration*. Third edition. 1975.
- [24] Lebrun P. *An introduction to cryogenics*. Tech. rep. CERN, Accelerator Technology Department, 2007.
- [25] Oxford University Press. *Oxford English Dictionary*. Second edition. 1989.
- [26] Reynolds W.C. *Thermodynamic properties in SI. Graphs, tables and computational equations for 40 substances*. Stanford univ., 1979, p. 172.
- [27] A.R. Jha. *Cryogenic Technology and Applications*. First. Butterworth-Heinemann, 2005, p. 296. ISBN: 9780080457970.
- [28] Frank Arute et al. "Quantum supremacy using a programmable superconducting processor". In: *Nature* 574.7779 (2019), pp. 505–510. ISSN: 14764687. DOI: 10.1038/s41586-019-1666-5.
- [29] John Clarke and Frank K. Wilhelm. "Superconducting quantum bits". In: *Nature* 453.7198 (2008), pp. 1031–1042. ISSN: 14764687. DOI: 10.1038/nature07128.
- [30] P. Arpaia et al. *Cryogenic Systems: Advanced Monitoring, Fault Diagnostics, and Predictive Maintenance*. Emerging technologies in measurement, instrumentation, and sensors collection. Momentum Press, 2017. ISBN: 9781946646309.
- [31] Batey G. and Teleberg G. *Principles of dilution refrigeration*. Oxford Instruments NanoScience. 2015.
- [32] BlueFors Cryogenics Ltd. *BF-XLD-Series cryogen-free dilution refrigerator system*. User manual. 2016.
- [33] N. Almtireen, J. J. Brandner and J. G. Korvink. "Pulse Tube Cryocooler: Phasor Analysis and One-Dimensional Numerical Simulation". In: *Journal of Low Temperature Physics* 199.5-6 (2020), pp. 1179–1197. ISSN: 15737357. DOI: 10.1007/s10909-020-02378-6.
- [34] J. R. De Laeter et al. "Atomic weights of the elements: Review 2000 (IUPAC Technical Report)". In: *Pure and Applied Chemistry* 75.6 (2003), pp. 683–800. ISSN: 00334545. DOI: 10.1351/pac200375060683.

- [35] BlueFors Cryogenics Ltd. *Bottom-Loading Fast Sample Exchange System*. User manual, Version 1. 2020.
- [36] American Magnetics Inc. *Multi-Axis Magnet systems for Vector Fields (MAXes™)*. downloaded in 2021.
- [37] Iwasa Y. *Case Studies in Superconducting Magnets*. Second Edition. Springer, 2009.
- [38] Christopher Coleman. *An Introduction to Radio Frequency Engineering*. Cambridge University Press, 2004. DOI: 10.1017/CB09780511801327.
- [39] Naoki Shinohara. "Theory of WPT". In: *Wireless Power Transfer via Radiowaves*. John Wiley and Sons, Ltd, 2013. Chap. 2, pp. 21–52. DOI: 10.1002/9781118863008.ch2.
- [40] Marcos Antonio De Sousa et al. "Parallel ferromagnetic resonance and spin-wave excitation in exchange-biased NiFe/IrMn bilayers". In: *Physica B: Condensed Matter* 450 (2014), pp. 167–172. ISSN: 09214526. DOI: 10.1016/j.physb.2014.05.050.
- [41] Cheng P Wen and Cheng P Wen. "A Surface Nonreciprocal Applications". In: *IEEE Transactions on Microwave Theory and Techniques* 17.12 (1969), pp. 28–31. ISSN: 0018-9480.
- [42] A. Penirschke et al. "Grounded coplanar waveguide transmission lines as pickups for beam position monitoring in particle accelerators". In: *IBIC 2013: Proceedings of the 2nd International Beam Instrumentation Conference* (2013), pp. 438–441.
- [43] Pozar D.M. *Microwave Engineering 4th Edition*. John Wiley and Sons, Ltd, 2011, p. 752.
- [44] Dan McMahill. *Coplanar Waveguide Analysis/Synthesis Calculator*. Accessed: 08.11.2021. URL: <http://wcalc.sourceforge.net/cgi-bin/coplanar.cgi>.
- [45] Swarup Bhunia and Mark Tehranipoor. "Chapter 4 - Printed Circuit Board (PCB): Design and Test". In: *Hardware Security*. Ed. by Swarup Bhunia and Mark Tehranipoor. Morgan Kaufmann, 2019, pp. 81–105. ISBN: 978-0-12-812477-2. DOI: <https://doi.org/10.1016/B978-0-12-812477-2.00009-5>.
- [46] George Harman. *Wire Bonding in Microelectronics*. en. McGraw Hill, New York, NY, 2010-01-04 2010.
- [47] Ivy Wei Qin et al. "Automatic wedge bonding with ribbon wire for high frequency applications". In: *Proceedings of the IEEE/CPMT International Electronics Manufacturing Technology (IEMT) Symposium* (2002), pp. 97–104. ISSN: 10898190. DOI: 10.1109/IEMT.2002.1032732.
- [48] COMSOL Inc. *RF module user guide v5.3a*. 2017.
- [49] Tim Jarvis. "Best practice in circuit board design". In: *Power* (2004), pp. 1–6. URL: http://ocw.bib.upct.es/pluginfile.php/7989/mod_resource/content/1/Best_practice_in_circuit_board_design.pdf.
- [50] Rogers Corp. *RO3000 Series Circuit Materials*. 2018. URL: <https://www.rogerscorp.com/documents/722/acs/R03000-Laminate-Data-Sheet-R03003-R03006-R03010.pdf>.
- [51] Arghya Sain and Kathleen L. Melde. "Impact of Ground via Placement in Grounded Coplanar Waveguide Interconnects". In: *IEEE Transactions on Components, Packaging and Manufacturing Technology* 6.1 (2016), pp. 136–144. ISSN: 21563950. DOI: 10.1109/TCPMT.2015.2507121.

- [52] COMSOL. *SMA Connector on a Grounded Coplanar Waveguide*. 2016.
- [53] Behnam Banan et al. "Electrical performance analysis of a CPW capable of transmitting microwave and optical signals". In: *International Journal of Microwave and Wireless Technologies* 9.8 (2017), pp. 1679–1686. ISSN: 17590795. DOI: 10.1017/S1759078717000575.
- [54] Cadence PCB solutions. *How to Use a Transmission Line Reflection Coefficient Correctly*. Accessed: 04.12.2021. URL: <https://resources.orcad.com/design-reliability/2021-how-to-use-a-transmission-line-reflection-coefficient-correctly>.
- [55] scikit-*rf* team. *Scikit-*rf**. Accessed: 23.02.2022. URL: [https://scikit-*rf*.readthedocs.io/en/latest/](https://scikit-<i>rf</i>.readthedocs.io/en/latest/).
- [56] Sarawuth Chaimool and Prayoot Akkaraekthali. "CPW-Fed Antennas for WiFi and WiMAX". In: *Advanced Transmission Techniques in WiMAX* May 2014 (2012). DOI: 10.5772/28456.
- [57] Jay L. Nadeau. "Introduction to Experimental Biophysics: Biological Methods for Physical Scientists". In: *Introduction to Experimental Biophysics* December (2018).
- [58] Yong Chen. "Review Nanofabrication : Conventional and nonconventional methods Miniaturization". In: *Electrophoresis Wiley Analytical Science* (2001).
- [59] T. Schneider et al. "Phase reciprocity of spin-wave excitation by a microstrip antenna". In: *Physical Review B - Condensed Matter and Materials Physics* 77.21 (2008), pp. 1–5. ISSN: 10980121. DOI: 10.1103/PhysRevB.77.214411.
- [60] S. Kosen et al. "Microwave magnon damping in YIG films at millikelvin temperatures". In: *APL Materials* 7.10 (2019). ISSN: 2166532X. DOI: 10.1063/1.5115266.
- [61] H. Maier-Flaig et al. "Temperature-dependent magnetic damping of yttrium iron garnet spheres". In: *Physical Review B* 95.21 (2017), pp. 1–8. ISSN: 24699969. DOI: 10.1103/PhysRevB.95.214423. arXiv: 1703.09444.
- [62] Sungkun Hong et al. "Hanbury Brown and Twiss interferometry of single phonons from an optomechanical resonator". In: *Science* 358.6360 (2017), pp. 203–206. ISSN: 10959203. DOI: 10.1126/science.aan7939. arXiv: 1706.03777.
- [63] Ralf Riedinger et al. "Non-classical correlations between single photons and phonons from a mechanical oscillator". In: *Nature* 530.7590 (2016), pp. 313–316. ISSN: 14764687. DOI: 10.1038/nature16536. arXiv: 1512.05360.
- [64] J. A. Haigh et al. "Magneto-optical coupling in whispering-gallery-mode resonators". In: *Physical Review A - Atomic, Molecular, and Optical Physics* 92.6 (2015), pp. 1–7. ISSN: 10941622. DOI: 10.1103/PhysRevA.92.063845.
- [65] A. Osada et al. "Cavity Optomagnonics with Spin-Orbit Coupled Photons". In: *Physical Review Letters* 116.22 (2016), pp. 1–5. ISSN: 10797114. DOI: 10.1103/PhysRevLett.116.223601.
- [66] Radebaugh R. *Thermodynamic properties of HE3-HE4 solutions with applications to the HE3-HE4 Dilution Refrigerator*. Tech. rep. U.S. Department of Commerce, National Bureau of Standards, 1967.

A. Appendix

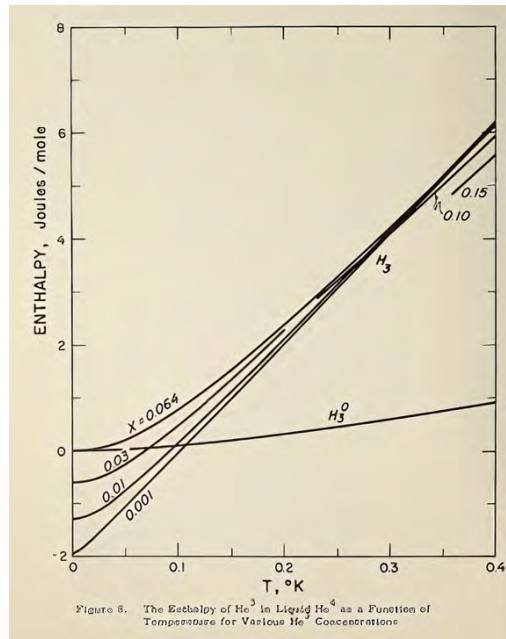
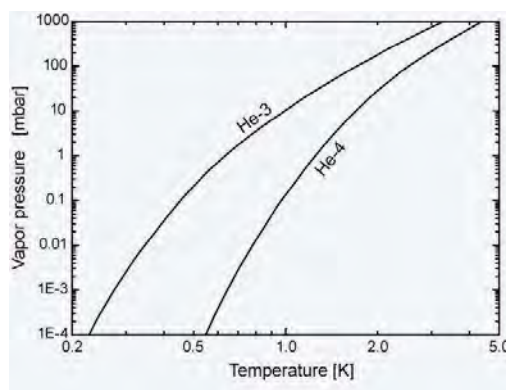


Figure A.1.: Enthalpy curve of ^3He in liquid ^4He as a function of temperature and for different concentrations. The enthalpy of ^3He atoms in ^4He is higher than in pure ^3He for the finite solubility of 6.4% (taken from [66]).



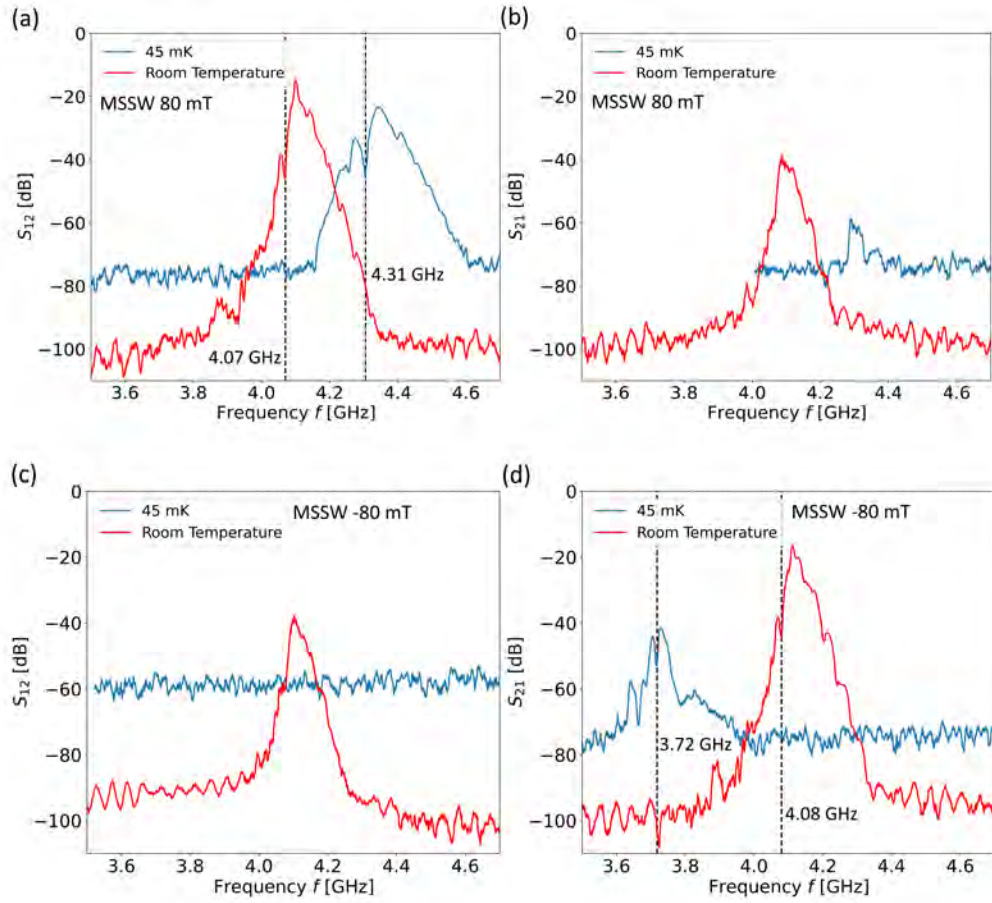


Figure A.3.: S_{12} transmission spectra of a room temperature (red) and a cryogenic (blue) PSWS measurement in the MSSW configuration. The data of the millikelvin PSWS study were corrected with respect to the dilution refrigerators transmission line losses and the nonmagnetic background. The spectra were obtained for an applied bias field of 80 mT (a)-(b) and -80 mT (c)-(d). Spin waves were recorded for an input power of -15 dBm at room temperature and 0 dBm at the cryogenic measurements, with a base temperature of 45 mK. The FMR-frequency f_{FMR} is illustrated with a black dotted line.

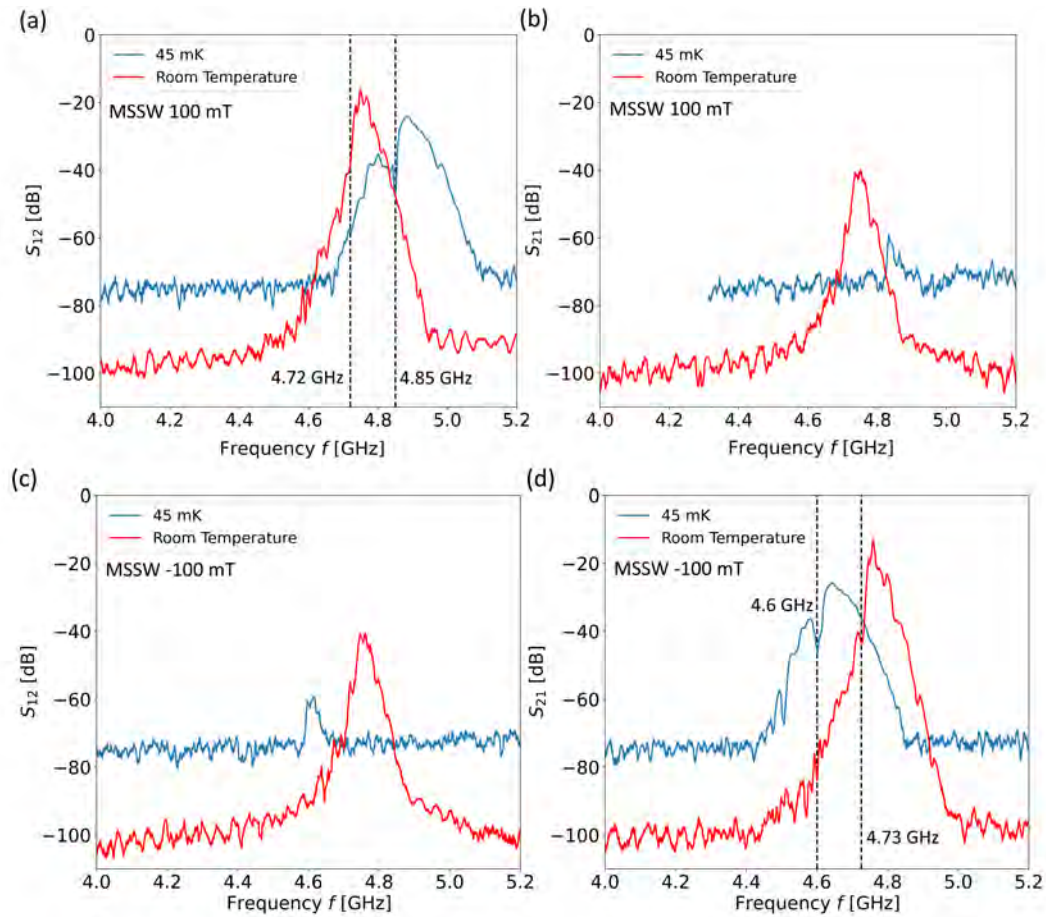


Figure A.4.: S_{12} transmission spectra of a room temperature (red) and a cryogenic (blue) PSWS measurement in the MSSW configuration. The data of the millikelvin PSWS study was corrected with respect to the dilution refrigerators transmission line losses and the nonmagnetic background. The spectra were obtained for an applied bias field of 100 mT (a)-(b) and -100 mT (c)-(d). Spin waves were recorded for an input power of -15 dBm at room temperature and 0 dBm at the cryogenic measurements, with a base temperature of 45 mK. The FMR-frequency f_{FMR} is illustrated with a black dotted line.

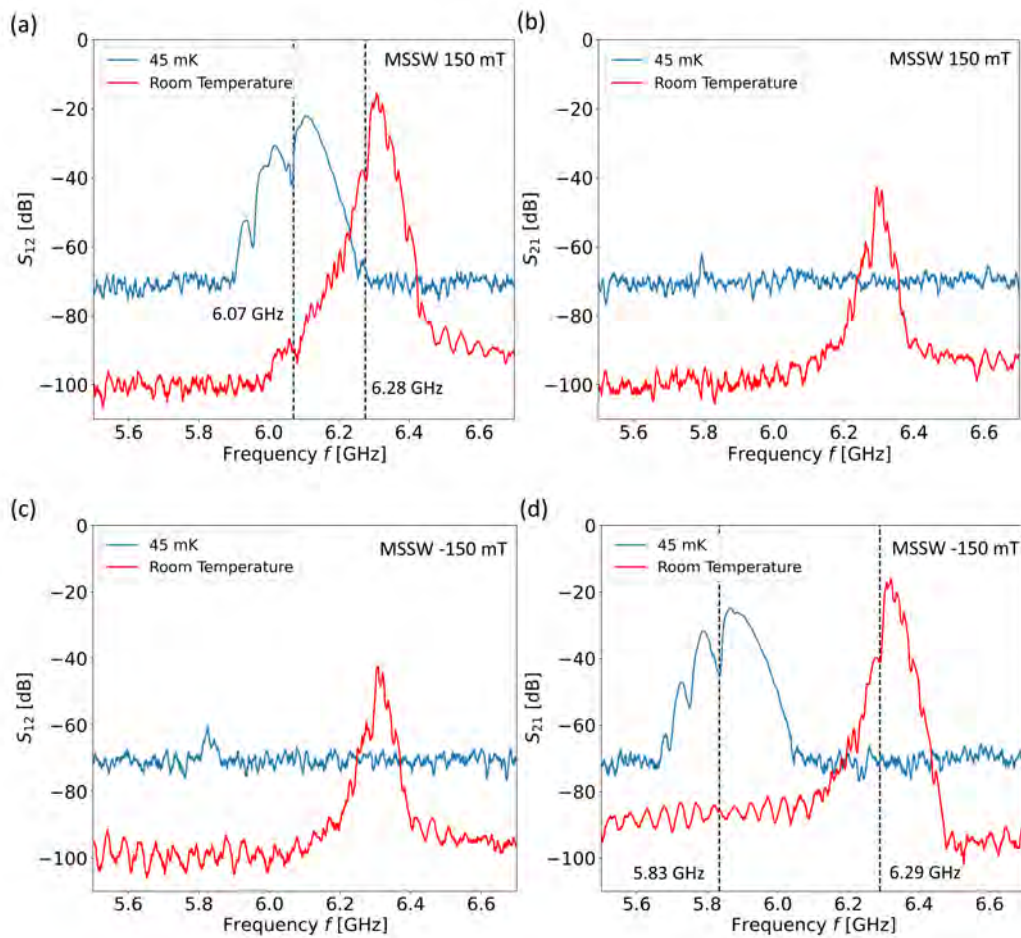


Figure A.5.: S_{12} transmission spectra of a room temperature (red) and a cryogenic (blue) PSWS measurement in the MSSW configuration. The data of the millikelvin PSWS study was corrected with respect to the dilution refrigerators transmission line losses and the nonmagnetic background. The spectra were obtained for an applied bias field of 150 mT (a)-(b) and -150 mT (c)-(d). Spin waves were recorded for an input power of -15 dBm at room temperature and 0 dBm at the cryogenic measurements, with a base temperature of 45 mK. The FMR-frequency f_{FMR} is illustrated with a black dotted line.

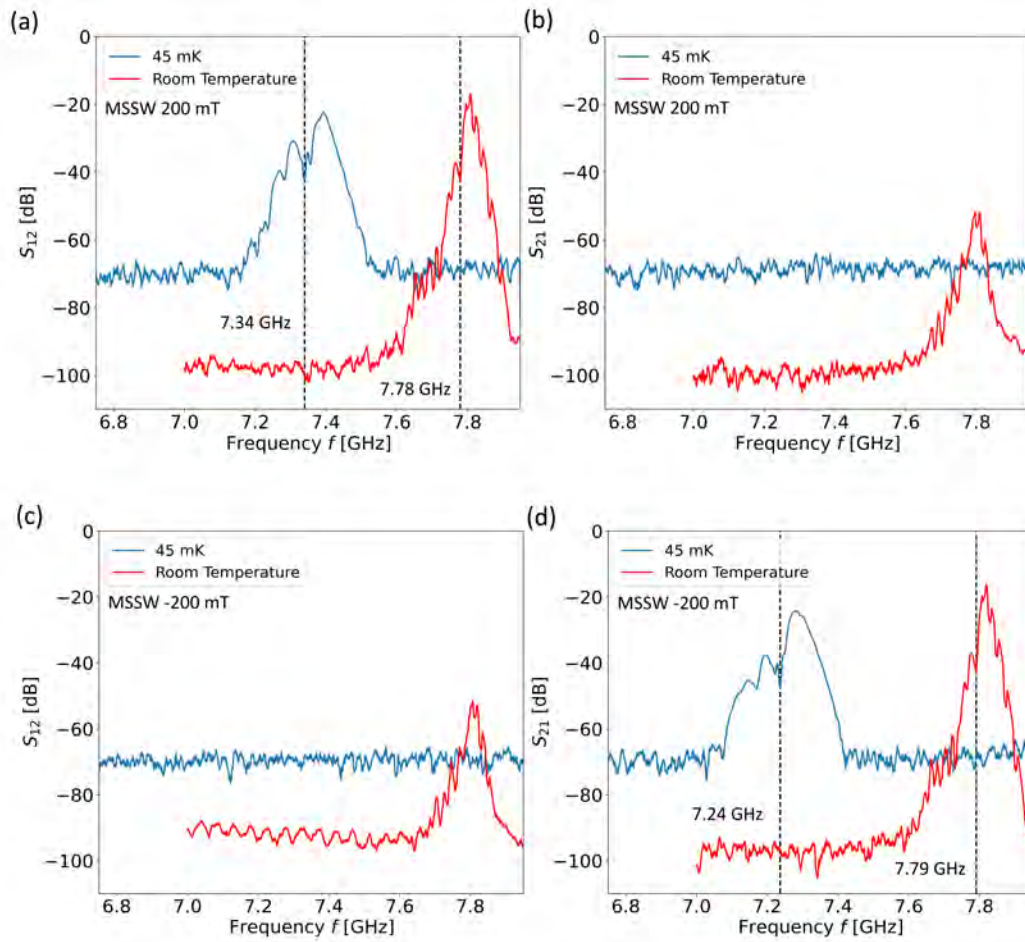


Figure A.6.: S_{12} transmission spectra of a room temperature (red) and a cryogenic (blue) PSWS measurement in the MSSW configuration. The data of the millikelvin PSWS study was corrected with respect to the dilution refrigerators transmission line losses and the nonmagnetic background. The spectra were obtained for an applied bias field of 200 mT (a)-(b) and -200 mT (c)-(d). Spin waves were recorded for an input power of -15 dBm at room temperature and 0 dBm at the cryogenic measurements, with a base temperature of 45 mK. The FMR-frequency f_{FMR} is illustrated with a black dotted line.

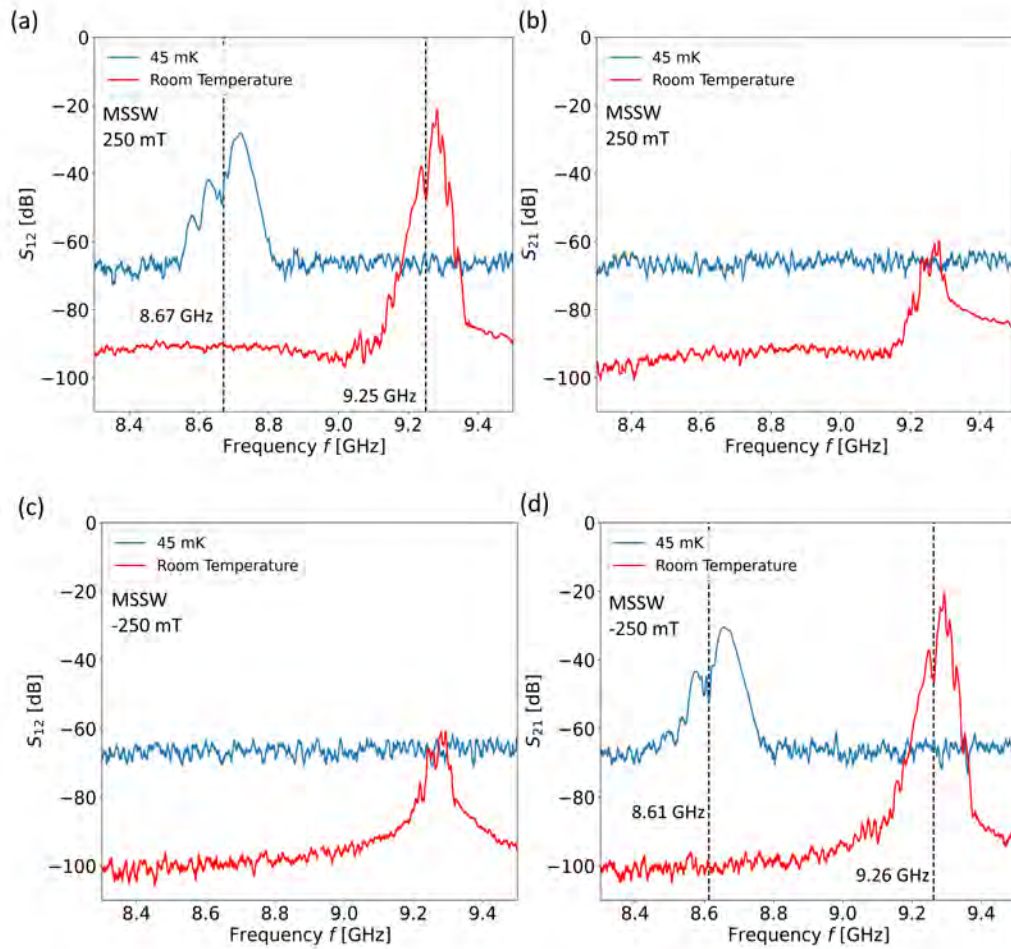


Figure A.7.: S_{12} transmission spectra of a room temperature (red) and a cryogenic (blue) PSWS measurement in the MSSW configuration. The data of the millikelvin PSWS study was corrected with respect to the dilution refrigerators transmission line losses and the nonmagnetic background. The spectra were obtained for an applied bias field of 250 mT (a)-(b) and -250 mT (c)-(d). Spin waves were recorded for an input power of -15 dBm at room temperature and 0 dBm at the cryogenic measurements, with a base temperature of 45 mK. The FMR-frequency f_{FMR} is illustrated with a black dotted line.

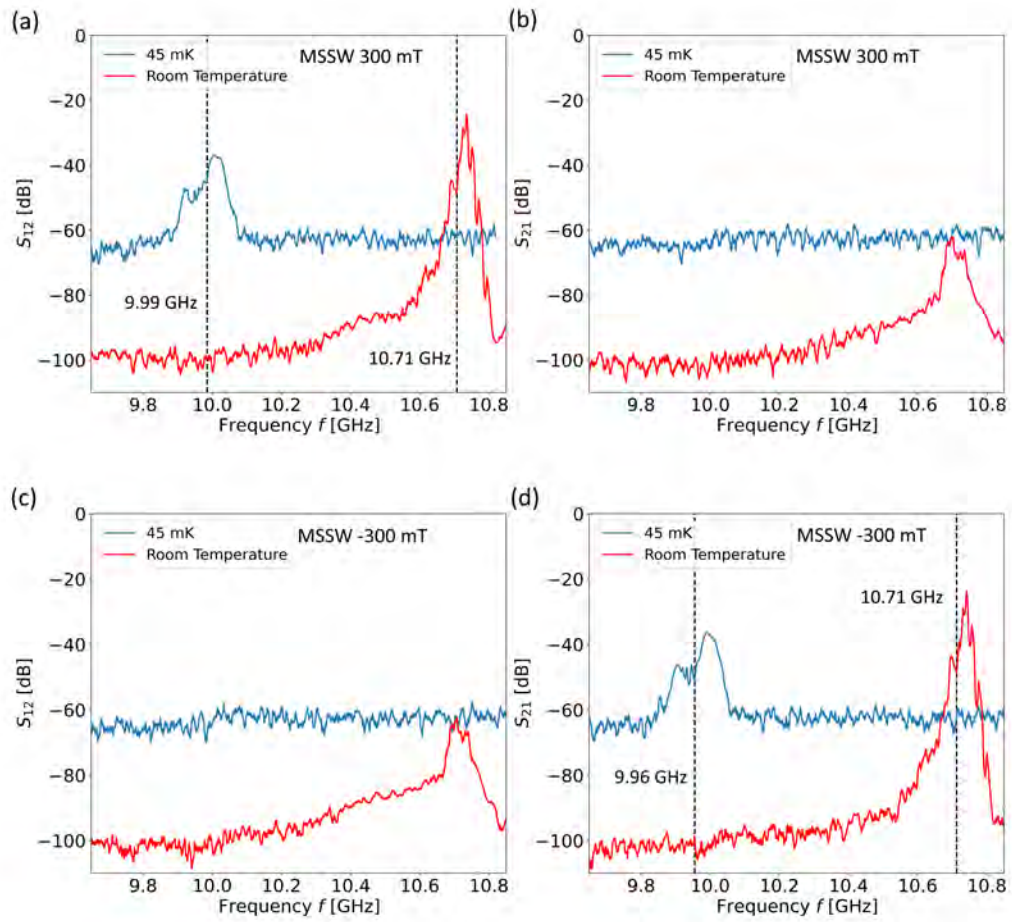


Figure A.8.: S_{12} transmission spectra of a room temperature (red) and a cryogenic (blue) PSWS measurement in the MSSW configuration. The data of the millikelvin PSWS study was corrected with respect to the dilution refrigerators transmission line losses and the nonmagnetic background. The spectra were obtained for an applied bias field of 300 mT (a)-(b) and -300 mT (c)-(d). Spin waves were recorded for an input power of -15 dBm at room temperature and 0 dBm at the cryogenic measurements, with a base temperature of 45 mK. The FMR-frequency f_{FMR} is illustrated with a black dotted line.

List of Tables

2.1. Characteristic temperatures of cryogenic fluids.	19
3.1. Attenuation configuration in the dilution refrigerators transmission lines. . . .	40
3.2. Parameters for the performance test of the superconducting vector magnet. . .	43
4.1. Pre-calculated dimensions and impedance values of fabricated CPW samples.	50

List of Figures

1.1.	Illustration of the motion of a magnetic moment in an external magnetic field.	13
1.2.	Comparison of spin-wave dispersion curves.	14
1.3.	Dispersion curve of a magnetostatic surface spin wave for different external fields.	15
2.1.	Schematic concept of a pulse tube cooler (PTC).	21
2.2.	Phase diagram of ^3He in ^4He for different concentrations x .	22
2.3.	Schematic of the main components of a dilution unit.	23
2.4.	Flow diagram of the gas handling system.	24
2.5.	Inner Layout of the cryostat with the different thermal stages.	25
2.6.	Layout of the bottom-loading sample exchange system.	26
2.7.	Simplified circuit diagram of a persistent mode superconducting magnet.	28
2.8.	Schematic diagram of the magnetic and electric field components in a grounded coplanar wave guide configuration.	29
2.9.	Schematic circuit diagram of a lumped element two-wire line.	30
2.10.	Design layout of a high-frequency PCB for experiments in the dilution refrigerator.	31
2.11.	Photo of the fabricated high-frequency PCB.	32
3.1.	Dilution refrigerator setup and samples for the experiments performed in this thesis.	36
3.2.	Cool down curve of the dilution refrigerator from room temperature to 4 K.	37
3.3.	Cool down curve of the mixing chamber from 4 K to base temperature.	38
3.4.	Temperature increase at the probe and the mixing chamber for different power inputs at the probe heater.	39
3.5.	Recorded losses of the dilution refrigerators transmission lines.	41
3.6.	Temperature development during the operation of the superconducting vector magnet.	42
4.1.	Geometry and dimensions of the GCPW that transmits high-frequency signals from the SMP connector to the bonding pad.	46
4.2.	Calculated electric field components of the high-frequency transmission lines of the PCB.	47
4.3.	S -parameters of the PCBs transmission lines, obtained with finite element frequency-domain studies.	48
4.4.	Simplified schematic for the experimental proof of principle of the designed high-frequency PCB.	49
4.5.	Calculated electric field components of fabricated CPW samples.	51
4.6.	Fabrication steps performed for the CPW samples.	52
5.1.	Photo of the used microantenna-PCB in the room temperature and the cryogenic PSWS setup.	56

5.2.	Uncorrected S_{12} transmission spectra of a room temperature and a cryogenic PSWS measurement in the MSSW configuration.	56
5.3.	Linear fit of the losses of the dilution refrigerators transmission lines.	57
5.4.	S_{12} transmission spectra of a room temperature and a corrected cryogenic PSWS measurement in the MSSW configuration.	58
5.5.	Background corrected S_{12} transmission spectra of a room temperature and a cryogenic PSWS measurement in the MSSW configuration.	58
5.6.	Comparison of the transmission spectra of room temperature and cryogenic PSWS measurements.	59
5.7.	Comparison of the S_{12} spectra and the dispersion relations of room temperature and cryogenic PSWS measurements.	61
5.8.	Field $\mu_0 H_0$ versus frequency f_{FMR} plot for MSSWs with applied bias fields ranging from -350 mT to 350 mT.	63
5.9.	Dependence of $\mu_0 H_{\text{cal}}$ on the external magnetic bias field $\mu_0 H_0$	64
5.10.	Field $\mu_0 H_0$ versus frequency f plot for BVMSWs with applied bias fields ranging from -200 mT to 200 mT.	65
A.1.	Enthalpy curve of ^3He in liquid ^4He	75
A.2.	Vapour pressure of ^3He and ^4He at near zero Kelvin temperatures.	75
A.3.	S_{12} spectra of a room temperature and a cryogenic PSWS measurement in the MSSW configuration at bias fields of 80 mT and -80 mT.	76
A.4.	S_{12} spectra of a room temperature and a cryogenic PSWS measurement in the MSSW configuration at bias fields of 100 mT and -100 mT.	77
A.5.	S_{12} spectra of a room temperature and a cryogenic PSWS measurement in the MSSW configuration at bias fields of 150 mT and -150 mT.	78
A.6.	S_{12} spectra of a room temperature and a cryogenic PSWS measurement in the MSSW configuration at bias fields of 200 mT and -200 mT.	79
A.7.	S_{12} spectra of a room temperature and a cryogenic PSWS measurement in the MSSW configuration at bias fields of 250 mT and -250 mT.	80
A.8.	S_{12} spectra of a room temperature and a cryogenic PSWS measurement in the MSSW configuration at bias fields of 300 mT and -300 mT.	81